



UNIVERSIDAD DE CHILE
FACULTAD DE CIENCIAS FÍSICAS Y MATEMÁTICAS
DEPARTAMENTO DE INGENIERÍA ELÉCTRICA

ULTRA-PURE DIGITAL DETECTION OF POLARIZATION FOR RADIO
ASTRONOMY APPLICATIONS

TESIS PARA OPTAR AL GRADO DE MAGÍSTER EN CIENCIAS DE LA
INGENIERÍA, MENCIÓN INGENIERIA ELÉCTRICA

ANDRÉS ARTURO ALVEAR CABEZÓN

PROFESOR GUÍA:
RICARDO ALBERTO FINGER CAMUS

MIEMBROS DE LA COMISIÓN:
NICOLÁS ANDRÉS REYES GUZMÁN
SHIN'ICHIRO ASAYAMA

Este trabajo ha sido parcialmente financiado por Centro de Astrofísica y Tecnologías Afines (CATA-BASAL-PBF 06), FONDECYT 11140428 y 1121051, y ALMA-CONICYT 31150012. Agradecemos a Xilinx Inc. por la donación de circuitos integrados y licencias de software y a la comunidad de CASPER por el apoyo brindado.

SANTIAGO DE CHILE
APRIL 2018

RESUMEN DE LA TESIS
PARA OPTAR AL GRADO DE
MAGÍSTER EN CIENCIAS DE LA INGENIERÍA,
MENCIÓN INGENIERIA ELÉCTRICA
POR: ANDRÉS ARTURO ALVEAR CABEZÓN
FECHA: ABRIL 2018
PROF. GUÍA: SR. RICARDO FINGER CAMUS

DETECCIÓN DIGITAL ULTRA-PURA DE POLARIZACIÓN PARA APLICACIONES RADIOASTRONÓMICAS

La polarización es una de las principales medidas dentro de la radioastronomía porque su estado entrega información de las condiciones físicas acerca del origen de la radiación observada y sobre el medio que la radiación ha traspasado.

En receptores radioastronómicos, el dispositivo utilizado para separar la polarización se conoce como transductor de modos ortogonales (Ortho-Mode Transducer u OMT, por sus siglas en inglés). Los OMT son componentes pasivos de microondas que dividen la radiación electromagnética de su puerto de entrada en dos componentes lineales y ortogonales entre sí.

Los receptores heterodinos de banda ancha generalmente obtienen razones de aislación de polarización de 15dB a 20dB, insuficientes para algunas aplicaciones radio astronómicas. Esta baja razón de aislación de polarización se debe a la presencia de fugas de una polarización a la otra, proceso que se conoce como polarización cruzada.

Con el fin de mejorar la aislación de polarización y reducir la polarización cruzada, se ha propuesto un nuevo enfoque denominado OMT digital, basado en pasar una funcionalidad dada del dominio análogo al dominio digital utilizando técnicas de procesamiento digital de señales.

Las técnicas digitales que fueron estudiadas para mejorar el rendimiento del OMT, condujeron al diseño de un *polarímetro* basado en la Transformada de Fourier Rápida (FFT) implementado en un FPGA, incluyendo la implementación de un Front-End análogo de banda Ku construido para caracterizar el OMT y medir la polarización sintetizada.

Esta tesis introduce un prototipo de un OMT digital calibrable con capacidad de procesamiento en tiempo real e integración continua que es adecuado para mediciones radioastronómicas. La configuración utilizada se basa en la arquitectura de un compacto OMT de cuatro puertos. Las salidas del OMT se convierten hacia abajo mediante el uso de mezcladores. Las señales convertidas hacia abajo se digitalizan directamente utilizando cuatro ADCs de 8 bits a 1.2 GSPS. El híbrido de 180° que permite recombinar y separar los vectores de polarización, está implementado en el FPGA junto con un conjunto de vectores de calibración, con el objetivo de corregir los desbalances de amplitud, fase y aislación típicos de un Front-End radioastronómico analógico.

El OMT digital calibrado exhibe una razón de aislación de polarización superior a 40 dB para todo el ancho de banda de recepción. Esto representa una mejora de un factor de 10 a 100 respecto a los actuales OMTs analógicos.

Abstract

Polarization is a key measurement within radio astronomy because its state can give insight as to the physical conditions of the source and the medium the radiation has traveled through. In radio astronomy receivers, the device used to separate the polarization is known as an Ortho-Mode Transducer (OMT). The OMT is a passive component that separates signals into two orthogonal components.

Using available millimeter-wave analog technology, wideband heterodyne receiver systems generally obtain polarization isolation ratios of 15dB to 20dB, insufficient for modern astronomical applications. That low polarization isolation ratio is due to the presence of leakage from one polarization contaminating the other, which is known as cross-polarization.

In order to improve polarization isolation and reduce cross-polarization, a new approach called Digital OMT has been proposed, based on passing one given functionality from the analog domain to the digital domain using digital signal processing techniques.

Digital techniques were studied to improve OMT performance, which led to the design of a *polarimeter* based on the Fast Fourier Transform (FFT). The polarimeter was implemented on a Field Programmable Gate Array (FPGA), including the implementation of a Ku-band analog front-end to characterize the design and measure the synthesized polarization.

This thesis introduces a prototype of a DOMT created for real-time processing and continuous integration, suitable for radio astronomy observations. The configuration used is based on the architecture of a compact four-port OMT. The outputs are downconverted using mixers and then directly digitalized using four 8bit ADC sampling at 1.2 GSPS. A 180° hybrid was implemented on the FPGA together with a set of calibration vectors, with the purpose of compensating the amplitude and phase imbalance typical of analog radio astronomy front-ends.

This calibrated Digital OMT exhibits a polarization isolation ratio of more than 40 dB for the entire RF bandwidth, representing an improvement factor of 100 over its analog counterpart.

*To my family and MWL's friends
for everything they taught me.*

Acknowledgments

First all, thanks to my family for being part of this process and all your love during my lifetime.

I would like to thank my guide Professor Ricardo Finger from the Astronomy Department (DAS) at the University of Chile, for his sharing of knowledge and experience has been a rewarding and inspiring resource.

I am gratefully indebted to Nicolas Reyes, Shin'ichiro Asayama, Ignacio Barrueto and Ricardo Finger. This thesis owes a lot to their detailed comments and constructive feedback. Special thanks to the outstanding team who made this project possible. It is impossible to list them all, but we list some of the many who contributed to this effort. Thanks to David Monasterio for design the analog devices and help provided. Thanks to José Pizarro for the mechanical design and manufacturing of waveguide components. My grateful thanks are also extended to Rafael Rodriguez for his help in doing the measurements and data analysis. Thanks to Edgardo Huaracán, Raúl Sapunar, Tom Geelen, Chenwei Cai, Franco Curotto and Roberto Fuentes. I have had the unique opportunity working with all of you and being part of the ROACH Team (2013-2017).

This thesis represents not only my work done, but it is also a milestone in more than three years of work at the University of Chile and precisely at the Astronomy Department, within the Millimeter-wave laboratory (MWL) where I met unforgettable colleagues. Thanks to Professor Leonardo Bronfman, Francisco Navarrete, Valeria Tapia, Pablo Vásquez, Claudio Jarufe, Pablo Astudillo, Professor Patricio Mena, Professor Ernest Michael, Matías Tejada, Camilo Avilés, Pablo Zorzi, Víctor Hugo Calle, Miguel Sánchez, Rocío Molina, Felipe Besser, Miguel Martínez, Daniel Montofré, Christopher Muñoz, Rodolfo Jara, and Alexander Ibarra for their support and friendship through all these years that we spent working together.

It is my pleasure to acknowledge the assistance of the English Teacher Carlos Orellana who offered their valuable time and energy to review drafts of this master's thesis.

I would like to thank the Product Validation Team of Synopsys R&D Center for your understanding while I was working on this thesis. I have learned a lot of great stuff from this clever team.

Finally, I would thank to the support of the Center of Excellence in Astrophysics and Associated Technologies (CATA-BASAL-PBF 06), FONDECYT 11140428 and ALMA-Conicyt 31150012. Thanks also to Xilinx Inc. for the donation of FPGA chips and software licenses, as well as the support of the CASPER community.

Sincerely,
Andrés Alvear
March 10, 2018

Contents

1. Background and Motivation	1
1.1. Introduction	1
1.2. Digital Polarization Detection	2
1.3. Objectives	5
1.3.1. General Objective	5
1.3.2. Specific Objectives	5
1.4. Hypothesis	5
1.5. Thesis Outline	6
2. Literature Review	7
2.1. Electromagnetic Waves	7
2.1.1. Electromagnetic Uniform Plane Waves	8
2.1.2. Polarization	9
2.1.3. The Polarization Ellipse	11
2.2. Polarization Isolation	13
2.3. Calibration and Polarization Synthesis Analysis	13
2.3.1. Third calibration measurement at $\alpha = \frac{\pi}{4}$	15
2.4. Digital Orthomode Transducer Architecture	17
2.4.1. Front-End	17
2.4.2. Back-End	19
2.5. Spectrometers and Polyphase filter Bank	20
2.5.1. Polyphase Filter-Bank: PFB	22
2.6. Digital Implementation	23
2.6.1. The ADC	23
2.6.2. The FPGA	24
2.7. The Casper Toolflow and Xilinx Build Flows	27
2.7.1. Digital design techniques	30
2.8. Conclusions	31
3. Digital Orthomode Transducer Design and Construction	32
3.1. Hardware	32
3.1.1. Analog OMT Design	33
3.1.2. Coaxial and waveguide transitions	35
3.1.3. Full waveguide setup simulations	36
3.2. Measurement procedure	38
3.3. Measurements results	39

3.4.	DSB Heterodyne Front End receiver	40
3.5.	Digital Back-End	43
3.5.1.	ROACH-II	45
3.5.2.	External Clock reference synthesizer	46
3.5.3.	The ADC Board ADC1x5000-8	46
3.6.	FPGA Gateware design	48
3.6.1.	Calibration:	49
3.6.2.	Polarization synthesis	50
3.7.	Digital Orthomode Transducer Gateware	51
3.7.1.	Calibration Gateware	52
3.7.2.	Synthesis Gateware	54
4.	Results and Measurements	59
4.1.	Test-Setup	59
4.2.	Digital OMT validation	60
4.3.	Polarization Synthesis using the ideal gain matrix	62
4.4.	Calibration	63
4.4.1.	Elements of the gain matrix G:	66
4.5.	Synthesis measurements	68
4.5.1.	Discussion and Conclusions	69
5.	Conclusion	72
	Bibliography	73
	Appendices	I
A.	Appendix-A	II
B.	Appendix-B	XVII
C.	Appendix-C	XIX

List of Tables

2.1. High-speed ADCs that are currently available at the MWL.	24
2.2. FPGAs comparison: Virtex-5 vs. Virtex-6	27
3.1. Instrument used in this test-setup:	38
3.2. Mixer ZX05-24-MH+:	41
3.3. Amplifier ZX-60-43+:	43
3.4. Low Pass Filter VHF-5050+:	43
4.1. Instruments used in this experiment:	59

List of Figures

1.1. Operating scheme of ALMA observatory.	2
1.2. ALMA Heterodyne Front-End receivers Band-1 (UChile prototype) and Band-3.	3
1.3. Cross-pol (XsP) behavior with respect to frequency for orthogonal linear polarizations P0 and P1 for five different ALMA band-4 cartridges.	4
2.1. Types of polarization of electromagnetic waves [1].	9
2.2. Elliptically Polarized Monochromatic Wave.	11
2.3. Polarization ellipse showing the orientation angle Ψ and ellipticity χ , which are a function of the semi-major and semi-minor axes, ξ and η	12
2.4. Typical configuration of a Dual Sideband mixer (DSB).	18
2.5. Frequency mixing process. After down-conversion the USB and LSB are overlapped in the IF band.	18
2.6. Overview of the FFT Spectrometers developed at the Millimeter Wave Laboratory, University of Chile	19
2.7. The two methods used to compute the PSD of a signal	20
2.8. Comparison of the channel response of an Auto-Correlation Spectrometer (ACS, dotted line), Fourier Transform Filterbank (FTF, dashed line) and an 8-tap, Hann-windowed Polyphase Filter Bank(PFB, solid line) [2].	23
2.9. Generic FPGA architecture	25
2.10. Disposition of Slices within the CLB	25
2.11. Xilinx Virtex-6 FPGA Slice structure	26
2.12. Casper Toolflow.	28
2.13. General Xilinx FPGA build flow.	29
2.14. FPGA Design flow using PlanAhead.	30
3.1. Digital Ortho-Mode Transducer block diagram	32
3.2. Circular waveguide to 4 coaxial probes OMT HFSS 3D model.	33
3.3. Circular waveguide to 4 coaxial probes OMT: Transmissions and reflections	34
3.4. Four probes OMT manufactured in two aluminum blocks.	34
3.5. Simulated cross polar leakage of the OMT from the input port to the orthogonal ports.	35
3.6. Coaxial to rectangular (left) and rectangular to circular (right) waveguide transitions design.	35
3.7. Simulation of all characteristics of the Coaxial to rectangular waveguide (left) and the rectangular to circular waveguide transition (right).	36

3.8. OMT + rectangular to circular waveguide transition + WR-62 to SMA transition.	36
3.9. Simulation of all characteristics when the OMT and the circular to rectangular transition are connected.	37
3.10. Manufactured OMT breakdown	38
3.11. Sketch of the VNA setup to measure the S-parameters from 12 to 18 GHz.	39
3.12. Circular waveguide to 4 coaxial probes OMT Transmission and reflection measurement using VNA.	39
3.13. Circular waveguide to 4 coaxial probes OMT and cross-polarization measurement using VNA.	40
3.14. Block diagram of the Digital ortho-mode transducer front-end setup.	41
3.15. DOMT Front-End.	42
3.16. Coaxial Frequency mixer, wide band from 7500 to 20000 MHz.	42
3.17. Wide band amplifier	42
3.18. Wide band Low pass filter	43
3.19. ROACH-II board	44
3.20. ROACH-II revision 2 block diagram.	45
3.21. EV8AQ160 chip ADC 5 GSps block diagram.	47
3.22. Snapshot obtained with a python script during phase difference compensation. This result was obtained after ADC calibration and FIFO delay compensation.	48
3.23. Digital OMT calibration schematic.	50
3.24. Top level Simulink block diagram of the Digital Orthomode Transducer (available in Appendix B).	51
3.25. Snapshot circuit to record blocks of data obtained by the ADCs	52
3.26. Left side of the calibration gateway, left to right: ADC, FIFO.	53
3.27. The real PFB spectrometer is composed of a 4-tap Fir filter and a 4096-point FFT	54
3.28. The Calibration model records the quantized complex spectra (FFT's outputs) in the yellow blocks.	55
3.29. The middle side of the polarization synthesis model	56
3.30. The adder trees of the polarization synthesis model	57
3.31. The vector accumulators of the polarization synthesis model	58
4.1. Sketch of the calibration setup to obtain calibration coefficients	60
4.2. Measuring test setup implemented for the DOMT characterization	61
4.3. Co-pol and Cross-pol spectra of the uncalibrated Digital OMT	62
4.4. Measured Cross-Polarization Isolation for X-Pol and Y-pol using the ideal gain matrix.	63
4.5. Schematic of the DOMT calibrating spectrometer	64
4.6. The initial calibration measurement was taken with the input transition set at $\alpha = 0^\circ$	65
4.7. The second calibration measurement was taken with the input transition rotated 90° clockwise. $\alpha = 90^\circ$	65
4.8. The third calibration measurement was taken with the input transition rotated 45° anticlockwise. $\alpha = 45^\circ$	66
4.9. Measured gain matrix amplitudes, a_x , for the X probes of the digital ortho-mode transducer	67

4.10. Measured gain matrix amplitudes, a_y , for the Y probes of the digital orthomode transducer	67
4.11. Measured gain matrix phases, p_x , for the X probes of the digital orthomode transducer	68
4.12. Measured gain matrix phases, p_y , for the Y probes of the digital orthomode transducer	68
4.13. Full Ku-Band measurement of the cross-polarization isolation for the four-probe DOMT	69
C.1. HFSS 3D model of the degraded circular waveguide to 4 coaxial probes OMT (left) and lateral view of the Circular waveguide to 4 coaxial probes OMT (right).	XIX
C.2. Circular waveguide to 4 coaxial probes degraded OMT transmission and reflection simulation results using HFSS.	XX
C.3. Circular waveguide to 4 coaxial probes degraded OMT and cross-polarization simulation results using HFSS.	XX
C.4. Photograph of the prototype digital orthomode transducer. Four probes OMT manufactured in two aluminum blocks with two probes with two bent antennas.XX	
C.5. Circular waveguide to 4 coaxial probes degraded OMT transmission and reflection measurement using VNA.	XXI
C.6. Circular waveguide to 4 coaxial probes degraded OMT and cross-polarization measurement using VNA.	XXI

Chapter 1

Background and Motivation

1.1. Introduction

The Millimeter Wave Laboratory (MWL) at the University of Chile is involved in the development of Front End receivers for millimeter-waves like Band 1, presented in Figure 1.2.b, of the Atacama Large Millimeter/submillimeter Array (ALMA) Observatory.

The ALMA Front End system is the first element in a complex chain of signal reception, conversion, processing and recording. As shown in Figure 1.2, the first element in the chain is a horn antenna receiving radio signals.

The second element in the cartridge is the Ortho-Modal Transducer (OMT), which separates polarization of a signal. The OMT is a waveguide passive component that separates the received astronomical signal into two orthogonal linearly-polarized components. It has two rectangular waveguide outputs that guide these modes independently through a rectangular wave guide. Using these two polarization channels that are amplified by independent amplification chains, one can estimate the 4 Stokes parameters of the incoming signal [3].

Subsequently, the signals are amplified by a Low Noise Amplifier (LNA). The LNA is composed by HEMT (High Electron Mobility Transistor) transistors. Finally, the signal is led to the mixers, or heterodyne stage, based on Schottky diodes for millimeter wavelengths in which it is down-converted to base-band to facilitate digitization in the Back End (see, e.g., Fig. 1.1). For sub-millimeter wavelengths the receiver change its configuration by means of a SIS mixer (Superconductor - Insulators - Superconductor) and then a LNA.

According to the experience of the MWL in the projects of ALMA Band 1 and Band 2+3, one of the most difficult elements to integrate inside a radio astronomy receiver is the OMT [4]. So resulting OMTs are bulky and do not fit geometrically with the receiver architecture, which makes it difficult to integrate into radio telescope Front End receivers. In order to place this device into compact receivers, we have to physically constrain its geometry, sometimes degrading its performance and increasing the complexity of the manufacturing process. To ensure its compatibility in an efficient manner with other components, such as the LNAs [5], a novel approach using digitally calibrated analog receivers was applied [6].

In particular, we want to demonstrate that a simple analog OMT made of four coaxial probes inserted in a circular waveguide can reach similar or better performance than Dual-Ridge [7],

Boifot [8], or Turnstile [9] OMTs commonly used in Radio Astronomy receivers. This could allow the construction of high-performance dual polarization receiver arrays, which are normally single polarization due to the difficulty of miniaturizing and integrating a large number of OMTs.

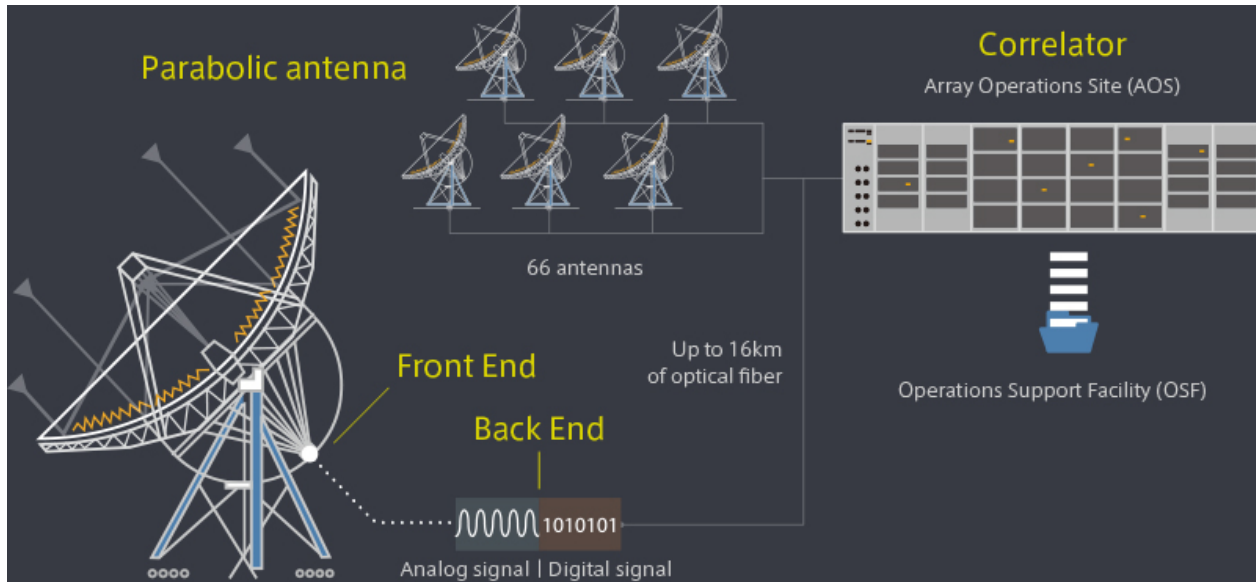


Figure 1.1. Operating scheme of ALMA observatory. Source: <http://www.almaobservatory.org/en/about-alma-at-first-glance/how-alma-works/>

1.2. Digital Polarization Detection

The observations of polarization are of great importance for the scientific community because there is a square root of 2 improvement in the signal-to-noise ratio (S/N), or a reduction factor of 2 in observing time on a telescope (e.g., Chattopadhyay et al. 2000) when both polarizations are received simultaneously [10].

In order to provide astronomy with detailed views of structures within areas of star formation which emit millimeter waves, a new generation of radio astronomy instruments require Front End receivers to function on a double-polarization configuration, including coherent detectors with unprecedented levels of sensibility, and dynamic range [11]. These will offer the field enhanced resolution, more chemical component features, greater velocities, and improved detection of astronomical object turbulence; all geared towards inspiring further exploration of astronomy.

Polarization sensitive detectors are strongly preferable over single polarization receivers for use in radio astronomy. Unfortunately they are difficult to build as they require doubling the number of components in the receiver chain and including a polarization splitter, also called Ortho-Mode Transducer (OMT), in the Front End. High frequency OMTs are passive waveguide devices that work well on small bandwidths. The leaking of one polarization into the other, cross-polarization, increases considerably when OMTs and other optical components operate away from the design central frequency (Figure 1.2-a). Typical cross-polarization performance of ALMA mm-wave receivers are around -23dB, with parts of the band as high as -19dB. The cross-polarization degradation comes both from OMT and optics/filters cross-pol signatures, sometimes not meeting ALMA specifications [12].

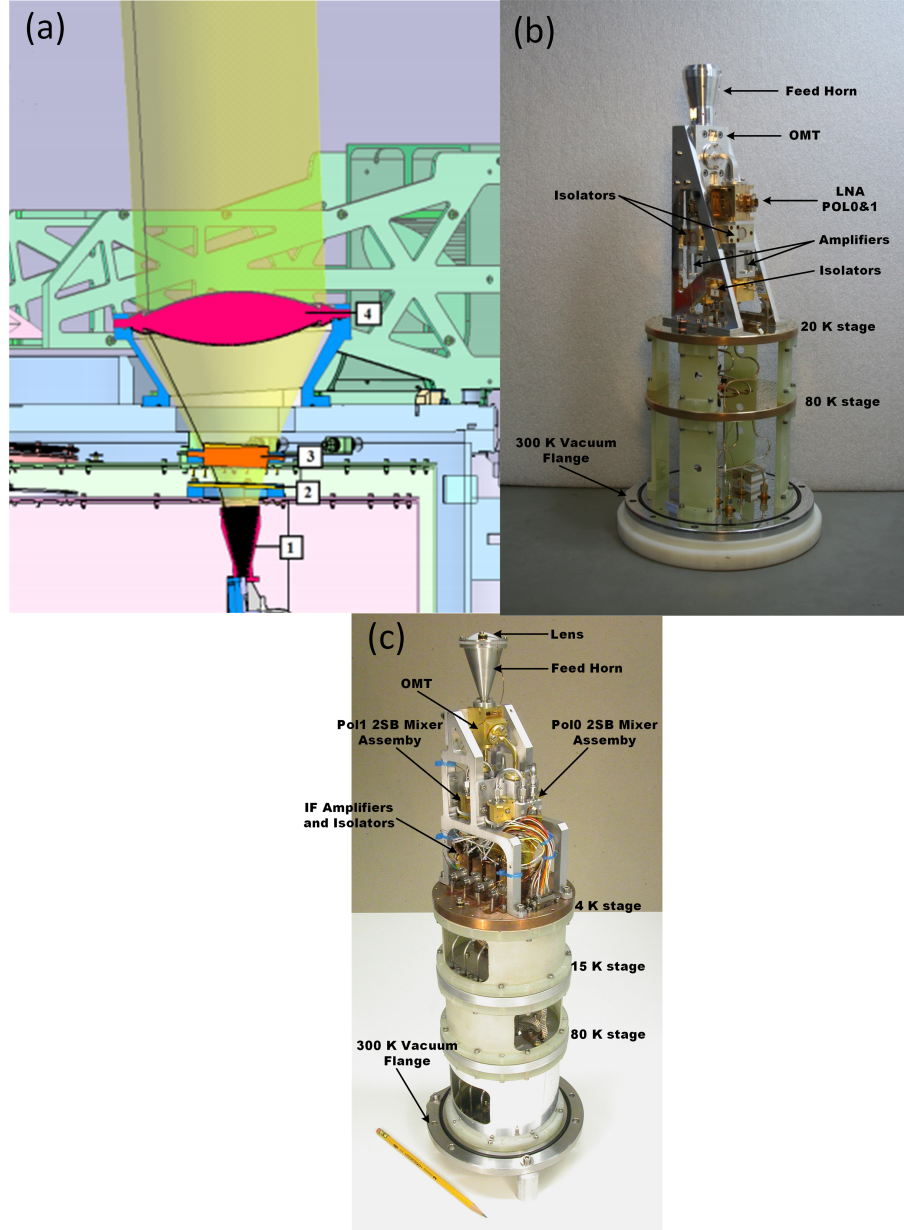


Figure 1.2. ALMA Heterodyne Front-End receivers Band-1 (UChile prototype) and Band-3. There are cryogenic stages present in the Front-End receivers to reduce the noise in the device, guaranteeing more precise measurements. (a) 1: Spline-profile corrugated. 2: 15K IR Filter. 3: 110K IR Filter. 4: Zoned Fresnel Lenses. (b) University of Chile Front-End Prototype for Band 1 (33-50GHz). The incoming RF signal is coupled with the horn via a lens (Fig. 1.a). The signal is then divided in its polarization components in an OMT. Then, each polarization signal is amplified. Finally, the amplified signals are filtered to suppress the lower sideband and mixed in separate Schottky diodes. (c) Front-End cartridge for ALMA Band 3 (84-116GHz). The incoming RF signal is coupled with the horn via a lens. The signal is then divided into its polarization components in an OMT. Then, the signal components are down-converted using a 2SB mixer giving separated USB and LSB. Finally, the IF signals are amplified.

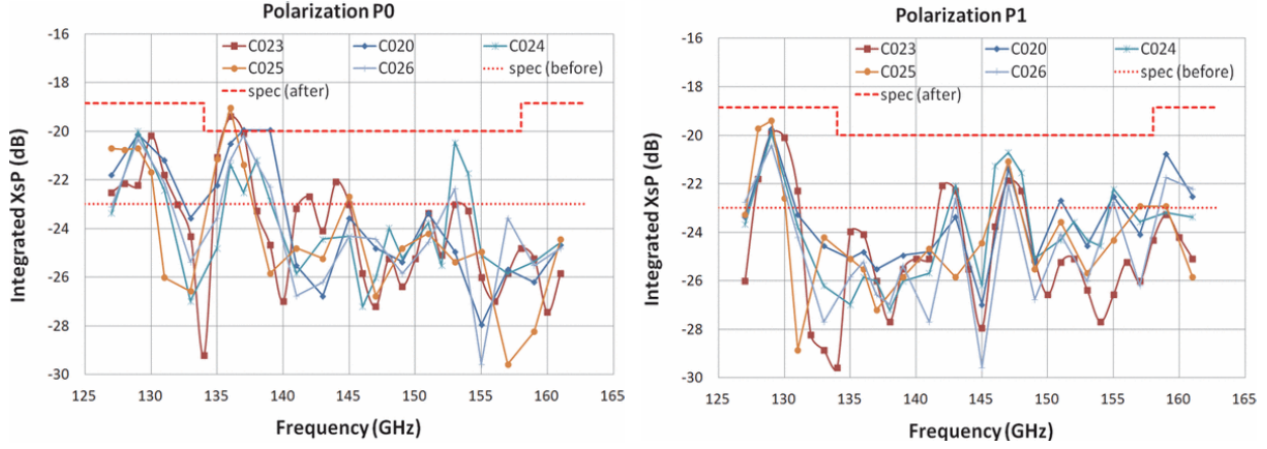


Figure 1.3. Cross-pol (XsP) behavior with respect to frequency for orthogonal linear polarizations P0 and P1 for five different ALMA band-4 cartridges. The dotted line at -23dB is the original ALMA specification for all bands. The dash line is the relaxed specification needed for band 4 [12].

These levels of cross-pol together with the antenna’s own polarization signature will produce errors of polarimetric measurements well above 1%. Considering that the degree of polarization of radio astronomy sources is typically only a few percent, the instrumental error becomes quite significant [12].

The advent of high speed digital technology has opened the possibility of building the same functionality of a wave-guide OMT in digital hardware, with the further prospect of calibrating the additional cross-pol contribution of the receiver optics; horns, lenses and possibly even the main antenna reflector.

Inspired by the pioneering work of Matthew Morgan and Rick Fisher [13], the Millimeter Wave Laboratory decided to focus its efforts on implementing the proof of concept developed by NRAO [5]. A prototype of a calibratable digital OMT created for real-time processing and continuous integration, suitable for radio astronomy. The configuration used is based on the architecture of a compact four-port OMT [14]-[15]. The OMT outputs are down-converted using mixers. The down-converted signals are directly digitized using a ROACH-II board [16], with four 8 bit ADC sampling at 1.2 GSPS, developed by CASPER [17]. Before the signal recombination a set of complex constants allow calibrating gain and phase imbalances introduced by the waveguide devices, and eventually the receiver optics, to reconstruct the original polarization state with unprecedented purity.

Finally a prototype Calibratable Digital Orthomode Transducer (DOMT) on a real-time FPGA-based processor capable of continuous integration and the results of its application reducing polarization isolation in the Ku-band with calibrated and uncalibrated spectra is discussed.

1.3. Objectives

1.3.1. General Objective

Design and build a prototype of a digital OMT by using the compact four-port OMT, and the analog front-end using commercial devices.

1.3.2. Specific Objectives

- Investigate EDA tools (CASPER and Xilinx Tool-Flow) and existing papers about the subject in order to design and implement a Calibratable Digital Orthomode Transducer (DOMT) using the ADC 5GSPS and the Virtex-6 FPGA available in the ROACH-II.
- Implement a Python or Matlab script to perform off-line numerical calibration to determine elements of the gain matrix G , obtaining data in a Plain text output file.
- Develop a Python script to operate as “Synthesizer mode” to load the gain matrix elements into the FPGA and then measure X-pol, Y-pol and Cross-polarization in Real-Time.
- Develop a Python script capable of measuring Polarization Isolation in the Ku-Band sweeping from 12 to 18 GHz, using 10 IF sub-bands of 600 [MHz] and 2048 channels, each.
- Validate the results of a polarization isolation graph in the Ku-band with calibrated and uncalibrated spectra to demonstrate and verify the proper working of the Digital OMT.
- Assure the quality of results of the DOMT with a polarization isolation graph, publication-quality figure, in the whole Ku-band with calibrated and uncalibrated spectra to demonstrate and verify the proper working of the Digital OMT.

1.4. Hypothesis

The use of Digital Signal Processing (DSP) algorithms by leveraging modern digital reconfigurable computing will be a significant technological step for the new generation of radio telescopes. In particular, Coherent Radio astronomy receiver performance can be improved by adding calibrated polarization isolation and replacing portions of the signal processing currently done by an analog Orthomode Transducer (OMT) with a calibratable digital OMT implemented in a reconfigurable hardware for real-time applications such as Field Programmable Gate Array (FPGA).

1.5. Thesis Outline

This thesis begins with a brief introduction to Digital Signal Processing for polarization detection in radio astronomy. Followed by:

- **Literature Review:** Chapter 2 proceeds to outline key concepts applied during OMT development. The central point of this Chapter consists in calibration, and synthesis method described in mathematical terms.
- **Digital Orthomode Transducer Design and Construction:** In chapter 3 the Digital OMT development and build are presented. This Chapter begins with a brief description of the whole system. From there it proceeds to outline the OMT HFSS simulations, the commercial components that were acquired to build the Front-End. Finally, the calibratable digital Back-End based on ROACH-2 using Fast Fourier Transform spectrometers is described.
- **Results and Measurements:** In chapter 4 the calibration measurements performed on the DOMT Analog Front-End are presented. To fully illustrate the results and relevant conclusions this is followed by a discussion regarding calibration and synthesis formulation, and measurement results.
- **Conclusions:** The final chapter of this work seeks to provide closure to the different concepts discussed here and summarizes the performances and strengths of the calibrated Digital OMT.

Chapter 2

Literature Review

This chapter describes the main concepts and theoretical support to understand the design, construction and characterization of a novel Digital Ortho-Mode Transducer for radio astronomy. For this purpose the fundamental concepts of electromagnetic theory will be reviewed. Wave phenomena are of essential importance in the present study, introducing uniform plane waves because they are the simplest form of electromagnetic waves and so serve to illustrate basic properties associated with polarization.

In the following sections, the DOMT's principles of operation will be presented. In doing so they will be presented mathematically in order to demonstrate an easy way to implement a calibration and polarization synthesis on a Xilinx FPGA Virtex-6.

2.1. Electromagnetic Waves

The phasorial Maxwell's equations are presented in the equations [2.1 - 2.4]. In this case phasor notation is very convenient because they consider that the whole system is oscillating at unique frequency in a lineal medium, allowing for phasorial analysis in function of the space. The objective of this formulation consists in using Maxwell's equations in order to disengage the Electromagnetic and Magnetic Fields and come up with the equations that characterize a wave in terms of the fields. This will be possible considering that a wave travels through in a source-free, linear, isotropic, homogeneous region, Maxwell's equations in phasor form are:

$$\nabla \times \vec{E}(\vec{r}) = -j\omega\vec{B}(\vec{r}) \quad (2.1)$$

$$\nabla \times \vec{H}(\vec{r}) = \vec{J}(\vec{r}) + j\omega\vec{D}(\vec{r}) \quad (2.2)$$

$$\nabla \cdot \vec{D}(\vec{r}) = \rho(\vec{r}) \quad (2.3)$$

$$\nabla \cdot \vec{B}(\vec{r}) = 0 \quad (2.4)$$

The equations 2.1 and 2.2 constitute two equations for the two unknowns, \vec{E} and \vec{H} . We rewrite these equations assuming the source-free medium $\rho(\vec{r}) = 0$ and lossless medium $\sigma = 0$ so, $\vec{J}(\vec{r}) = 0$. Then,

$$\nabla \times \vec{E} = -j\omega\mu\vec{H} \quad (2.5)$$

$$\nabla \times \vec{H} = j\omega\epsilon\vec{E} \quad (2.6)$$

Taking the curl of both sides of 2.5 gives:

$$\nabla \times \nabla \times \vec{E} = -j\omega\mu\nabla \times \vec{H} \quad (2.7)$$

Then, using 2.6 to replace $\nabla \times \vec{H}$ in equation 2.7 and to simplify the equation for \vec{E} , we use the vector identity $\nabla \times \nabla \times \vec{F} = \nabla(\nabla \cdot \vec{F}) - \nabla^2 \vec{F}$.

$$\nabla(\nabla \cdot \vec{E}) - \nabla^2 \vec{E} = \omega^2 \mu \epsilon \vec{E} \quad (2.8)$$

Then, $\nabla \cdot \vec{E} = 0$ in a source-free region. Equation 2.9 is the *wave equation* or *Helmholtz equation*, for \vec{E} .

$$\nabla^2 \vec{E} + \omega^2 \mu \epsilon \vec{E} = 0 \quad (2.9)$$

An analogue equation for \vec{H} can be derived in the same manner,

$$\nabla^2 \vec{H} + \omega^2 \mu \epsilon \vec{H} = 0 \quad (2.10)$$

A constant $k = \omega\sqrt{\mu\epsilon}$ is defined and called the *propagation constant* also known as the *phase constant* or *wave number*, of the medium.

2.1.1. Electromagnetic Uniform Plane Waves

In free-space, the Helmholtz equation for \vec{E} can be written as the equation 2.11:

$$\nabla^2 \vec{E} + k_0^2 \vec{E} = \frac{\partial^2 \vec{E}}{\partial x^2} + \frac{\partial^2 \vec{E}}{\partial y^2} + \frac{\partial^2 \vec{E}}{\partial z^2} + k_0^2 \vec{E} = 0 \quad (2.11)$$

and this vector wave equation holds for each rectangular component of \vec{E} , where the index $i = x, y, \text{ or } z$:

$$\frac{\partial^2 \vec{E}_i}{\partial x^2} + \frac{\partial^2 \vec{E}_i}{\partial y^2} + \frac{\partial^2 \vec{E}_i}{\partial z^2} + k_0^2 \vec{E}_i = 0 \quad (2.12)$$

The equation 2.12 is known as the *Helmholtz equation* and its solutions describe the Electromagnetic Uniform Plane Waves propagated through the medium [18]. Note that the \vec{E} and \vec{H} vectors are orthogonal to each other and orthogonal to the direction of propagation ($\pm z$); this is a characteristic of transverse electromagnetic (TEM) waves, which are characterized by not having field components in the direction of propagation. Without loss of generality it can be assumed that the wave travels in the \hat{z} direction reducing 2.12 to the equation 2.13:

$$\frac{\partial^2 E_x}{\partial z^2} + k^2 E_x = 0 \quad (2.13)$$

The equation 2.13 is an homogeneous differential equation within which two independent solutions to this equation are easily seen, by substitution, to be of the form

$$E_x(z) = E^+ e^{-jkz} + E^- e^{jkz} \quad (2.14)$$

where E^- and E^+ are arbitrary amplitude constants and the equation 2.14 presents the expression for the **Electric Field Vector of a Uniform Plane Wave** propagating in the

$+z$ direction. Consider the first term in 2.15. This term represents a wave traveling in the $+z$ direction because, to maintain a fixed point on the wave ($\omega t - kz = \text{constant}$), one must move in the $+z$ direction as time increases. Similarly, the second term in equation 2.15 represents a wave traveling in the negative $-z$ direction hence the notation $E+$ and $E-$ for these wave amplitudes.

The above solution is for the harmonic case at frequency ω . In the time domain, this result is written as the equation 2.15:

$$\mathcal{E}_x(z, t) = E^+ \cos(\omega t - kz) + E^- \cos(\omega t + kz) \quad (2.15)$$

2.1.2. Polarization

One of the properties of Electromagnetic field is that they have an aspect called 'polarization.' The polarization of a uniform plane wave is defined as the shape performed by the tip of the electric field vector in time at a given point in space [19]. From Maxwell's equations, we know a propagating EM wave (in the far field) has no component in the direction of propagation – it is a transverse wave.

$$\hat{k} \cdot \vec{E} = 0$$

The characteristics of the transverse component of the electric field, E , are referred to as the polarization properties in general. The E -vector follows a (elliptical) helical path as it propagates.

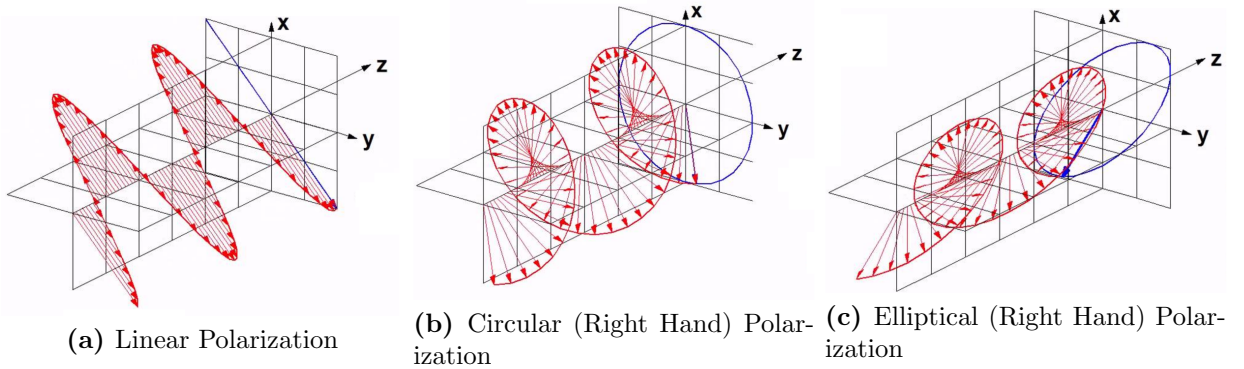


Figure 2.1. Types of polarization of electromagnetic waves [1].

If this locus is a straight line the wave is said to be linearly polarized. If this locus is a circle we have circular polarization and if it is an ellipse we have elliptical polarization. Actually, linear and circular polarizations are special cases of elliptical polarization [20].

There are several ways to define the polarization of electromagnetic Waves, (H,V) stands for horizontal and vertical, which can be easily pictured as x and y components; while (L,R) stands for left and right circular. It may be difficult to imagine that a vector in space can have a circular component in it, the secret lies in the fact that each component can be a complex number, which greatly increases the complexity of the trace of such a vector.

The time domain form of this electromagnetic wave can be written as Eq. 2.16:

$$\vec{\mathcal{E}}(z, t) = \hat{x}|E_x| \cos(\omega t - k_0 z + \theta_x) + \hat{y}|E_y| \cos(\omega t - k_0 z + \theta_y) \quad (2.16)$$

The equation 2.16 shows that the electromagnetic wave traveling in a forward-backward direction changes simultaneously with time and space along the z-axis.

$$E_x = |E_x|e^{j\theta_x}, E_y = |E_y|e^{j\theta_y} \quad (2.17)$$

Therein are the two components of phasor representation. The equation 2.17 is the most general equation to define polarization, \hat{x} and \hat{y} are the unit vector of x and y axes, respectively. The simplest case is a linear polarization, which happens when the two components are always in phase.

$$|E_x| = |E_y| = 1, \theta_x = \theta_y = 0$$

Assuming the field can be represented by a vector of [1;1]. The polarization for such a field looks like the linear polarization presented in Figure 2.1a. It is the projection of the combined field trace on the x-y plane shown in blue in the figure. The polarization ellipse is often characterized by two angles, the tilt angle (also known as polarization angle) α and the ellipticity angle ε . In this case, the tilt angle is 45 degrees and the ellipticity angle is 0. Hence, \vec{E}_0 is a vector over the x-y plane which can be written as follows in equation 2.18:

$$\vec{E} = [E_1 \hat{x} + E_2 \hat{y}] e^{-jk_0 z} \quad (2.18)$$

Where E_1 and E_2 are constants. If $E_1 \neq 0$ and $E_2 = 0$, we have a plane wave linearly polarized in the \hat{x} direction. Likewise, if $E_1 = 0$ and $E_2 \neq 0$, we have a plane wave linearly polarized in the \hat{y} direction. if E_1 and E_2 are both nonzero and real, we have a plane wave linearly polarized at the angle, α :

$$\alpha = \tan^{-1} \left(\frac{E_2}{E_1} \right) \quad (2.19)$$

The electric field vector lies along the straight line of slope $\tan^{-1}(\alpha)$. This is true for all z. For instance, if $E_0 = E_1 = E_2$, then we have:

$$\vec{E} = E_0 [\hat{x} + \hat{y}] e^{-jk_0 z} \quad (2.20)$$

which represents an electric field vector at a 45° angle from the x-axis. Next consider the superposition of two linearly polarized uniform plane waves; one polarized in the -x direction and the other in the -y direction lagging 90° in time. Consider $E_1 = jE_2 = E_0$, with $E_0 \in \text{Re}$:

$$\vec{E} = E_0 [\hat{x} - j\hat{y}] e^{-jk_0 z} \quad (2.21)$$

The time domain form of this electromagnetic wave is:

$$\vec{\mathcal{E}}(z, t) = E_0 [\hat{x} \cos(\omega t - k_0 z) + \hat{y} \cos(\omega t - k_0 z - \pi/2)] \quad (2.22)$$

The equation 2.22 shows that the electromagnetic wave traveling in a forward-backward direction changes simultaneously with time and space along the z-axis. To examine this set $z = 0$, Equation 2.23 then reduces to:

$$\vec{\mathcal{E}}(0, t) = E_0 [\hat{x} \cos(\omega t) + \hat{y} \sin(\omega t)] \quad (2.23)$$

so as ωt increases from zero, the electric field vector rotates counterclockwise from the x-axis. The resulting angle from the x-axis of the electric field vector at time t, at $z = 0$, is then:

$$\alpha = \tan^{-1} \left(\frac{\sin(\omega t)}{\cos(\omega t)} \right) = \omega t \quad (2.24)$$

which shows that the polarization rotates at the uniform angular velocity ω . Since the fingers of the right hand point in the direction of rotation of the electric field vector when the thumb points in the direction of propagation, this type of wave is referred to as a *right-hand circularly polarized* (RHCP) wave. Similarly, a field of the form

$$\vec{E} = E_0 [\hat{x} + j\hat{y}] e^{-jk_0 z} \quad (2.25)$$

constitutes a *left-hand circularly polarized* (LHCP) wave, where the electric field vector rotates in the opposite direction [18].

2.1.3. The Polarization Ellipse

From Maxwell's equations $\vec{E} \cdot \vec{B} = 0$ (\vec{E} and \vec{B} perpendicular). By convention, we consider the time behaviour of the E-field in a fixed perpendicular plane, from the point of view of the receiver. Then, For a monochromatic wave of frequency ω , we rewrite the electromagnetic field in phasor representation, (as equation 2.17):

$$E_x = |A_x|e^{j\theta_x}, E_y = |A_y|e^{j\theta_y} \quad (2.26)$$

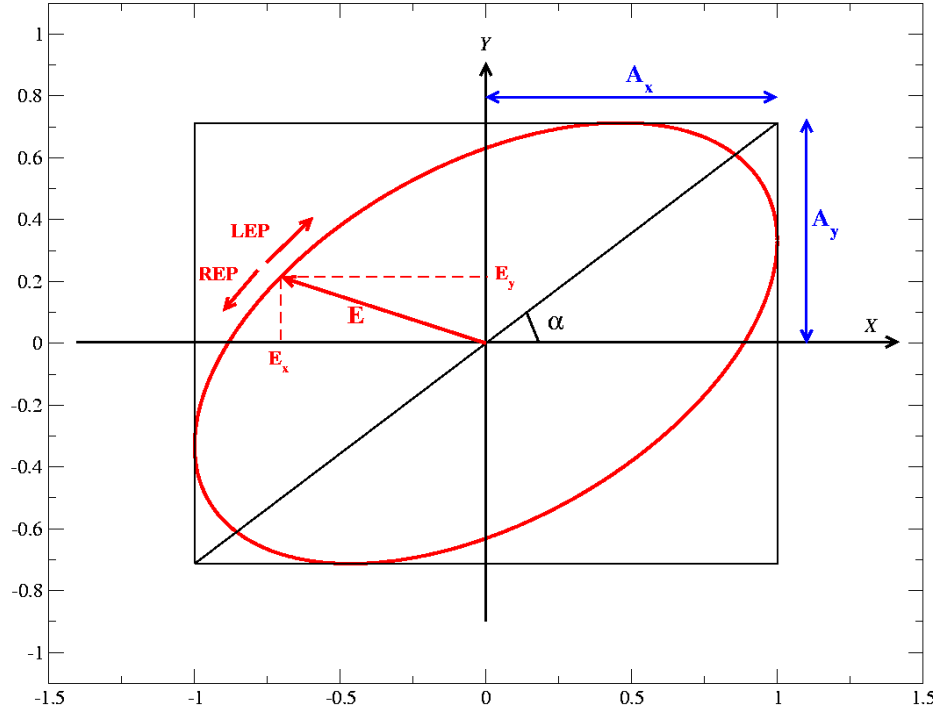


Figure 2.2. Elliptically Polarized Monochromatic Wave.

These two equations describe an ellipse in the (x-y) plane. Finally, the ellipse is described fully by three parameters: A_x , A_y , and the phase difference, $\delta = \theta_x - \theta_y$. The wave is elliptically polarized when $A_x \neq A_y$, and the phase difference, $\delta = \theta_x - \theta_y = \frac{\pi}{4}, \frac{3\pi}{4}, \frac{5\pi}{4}, \frac{7\pi}{4}, \dots, \frac{(2n+1)\pi}{4}$. In contrast, if $A_x = A_y = E_0$, and $\delta = \pm\frac{\pi}{2}$, is circularly polarized:

- Rotating clockwise, the wave is "Left Elliptically Polarized", $\delta = \frac{\pi}{2}$.
- Rotating counter-clockwise, it is "Right Elliptically Polarized", $\delta = -\frac{\pi}{2}$.

In Figure 2.2 an elliptically polarized monochromatic wave with a polarization angle $\alpha = \text{atan}(A_Y/A_X)$ is presented.

Figure 2.3 presents a more natural description of polarization ellipse in a frame (ξ, η) , rotated so the ξ -axis lies along the major axis of the ellipse. The polarization ellipse is often characterized by two angles, the tilt angle (also known as polarization angle) Ψ and the ellipticity angle χ .

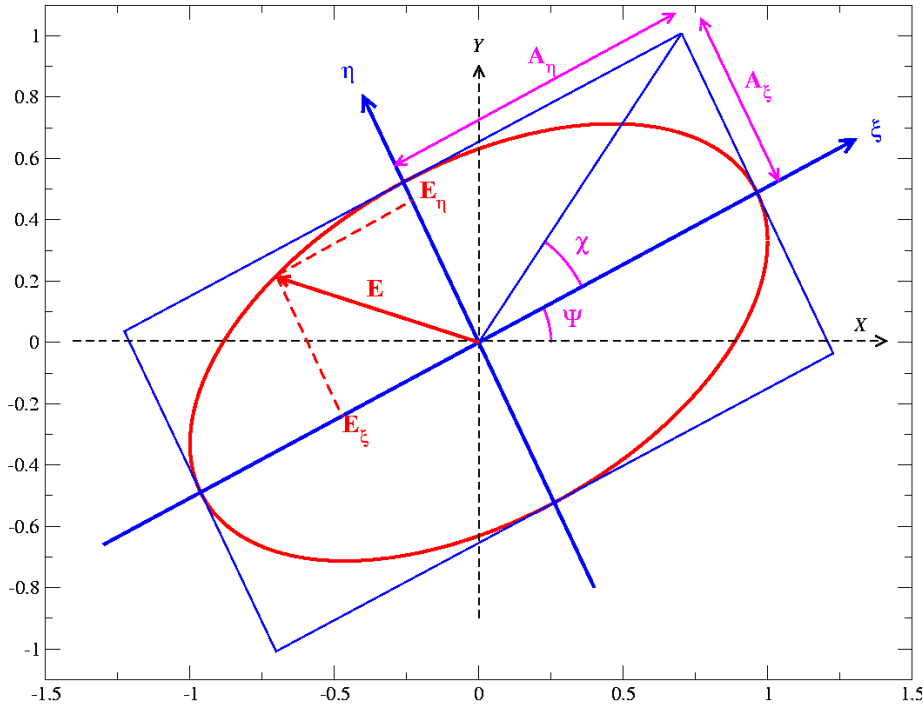


Figure 2.3. Polarization ellipse showing the orientation angle Ψ and ellipticity χ , which are a function of the semi-major and semi-minor axes, ξ and η .

However, three parameters are necessary to describe the ellipse:

1. A_η : the major axis length
2. $\tan \chi = A_\eta/A_\xi$: the axial ratio
3. Ψ : orientation angle regarding the major axis

This leads to purely trigonometric equations:

- $\tan(2\Psi) = \tan(2\alpha) \cos(\delta)$
- $\sin(2\chi) = \sin(2\alpha) \sin(\delta)$

The ellipticity angle, χ , is determined:

- $\chi > 0$, right-hand elliptical polarization (REP).
- $\chi < 0$, left-hand elliptical polarization (LEP)
- $\chi = 0, 90^\circ$ Linear polarization ($\delta=0^\circ, 180^\circ$)
- $\chi = \pm 45^\circ$ Circular polarization ($\delta=\pm 90^\circ$)

For instance, in the case that the polarization angle is 45 degrees and the ellipticity angle is 0.

2.2. Polarization Isolation

Polarization isolation is the ratio of the cross-polarized signal component from one transmitted polarization to the co-polarized signal component for the orthogonal transmitted polarization. It is the quantity that describe the performance of a dual-polarized system. Therefore, simultaneous measurements of co-polarized and cross-polarized signal components for two orthogonal linear polarizations should be made to compare the DOMT performance with their analog counterparts.

2.3. Calibration and Polarization Synthesis Analysis

As described in Morgan et al. [5], repeated here briefly, the behavior for a four probes orthomode transducer is represented by the following set of linear equations 2.27:

$$\begin{bmatrix} v_1 \\ v_2 \\ v_3 \\ v_4 \end{bmatrix} = \begin{bmatrix} a_{1x}e^{j\theta_{1x}} & a_{1y}e^{j\theta_{1y}} \\ a_{2x}e^{j\theta_{2x}} & a_{2y}e^{j\theta_{2y}} \\ a_{3x}e^{j\theta_{3x}} & a_{3y}e^{j\theta_{3y}} \\ a_{4x}e^{j\theta_{4x}} & a_{4y}e^{j\theta_{4y}} \end{bmatrix} \begin{bmatrix} s_0 \cos(\alpha)e^{j\beta} \\ s_0 \sin(\alpha)e^{j\beta} \end{bmatrix} \quad (2.27)$$

Or in matrix notation as shown in equation 2.28:

$$\vec{V} = \vec{G}\vec{S} \quad (2.28)$$

V is the output voltage vector from all four receiver channels connected to the DOMT, G is the complex gain matrix and S is the input signal vector in x and y polarization. The a_{ix} is the gain coefficient of probe i to x-polarized input signals. The term θ_{ix} is the phase difference between probe i and the probe chosen as the phase reference. The only assumption in this formulation is that the digital orthomode transducer is linear.

For instance, if a perfect x-pol input signal is injected to the circular 4-probe OMT, it will

be coupled to probes aligned to the x-axis, as shown in Eq. 4.10. S is frequency-dependent, so to simplify the example their terms are constant.

$$S = \begin{bmatrix} 1 \\ 0 \end{bmatrix} \quad (2.29)$$

By applying the Moore-Penrose Pseudo-Inverse [21] to G matrix in equation 2.28, the input sky signal, S , given the voltage outputs, V , is recovered as S' . Therefore the H matrix is then derived from the *measured* gain matrix. Equation 2.31 states what the pseudo-inverse should result in.

$$H = (G^\dagger G)^{-1} G^\dagger \quad (2.30)$$

$$S' = HV \quad (2.31)$$

S is a 2x1 matrix, H is a 2x4 matrix and V is a 4x1 matrix.

H is frequency dependent, and estimation of the input signal vector, S , from phasor voltages, V , takes place in the spectrometer after an FFT [5].

For each FFT channel a set of four complex-valued output vector, V , are computed. Then using V , the measurement matrix, M , is computed by cross-product spectra means, as shown in equation 2.32:

$$M = VV^* \quad (2.32)$$

To find the X-pol and Y-pol the elements of the gain matrix, G , should be computed by calibration measurements. Two measurements should be taken, first with an input test signal aligned with the x-axis ($\alpha = 0^\circ$) and the second with the input test aligned with the y-axis ($\alpha = 90^\circ$), then the terms of the measurement matrix must be obtained, by equation 2.33:

$$\begin{aligned} m_{ij} = & s_0^2 (a_{ix} a_{jx} e^{j(\theta_{ix} - \theta_{jx})} \cos^2(\alpha) \\ & + a_{ix} a_{jy} e^{j(\theta_{ix} - \theta_{jy})} \cos(\alpha) \sin(\alpha) \\ & + a_{iy} a_{jx} e^{j(\theta_{iy} - \theta_{jx})} \cos(\alpha) \sin(\alpha) \\ & + a_{iy} a_{jy} e^{j(\theta_{iy} - \theta_{jy})} \sin^2(\alpha)) \end{aligned} \quad (2.33)$$

Equation 2.32 ensures that the unknown phase constant β of the signal source is canceled and the only phase information remaining is caused by the system itself [5]. Note that equation 2.33 is dependent on the angle α and therefore for each measurement direction we end up with a simpler formula given by:

$$m_{i,j} = s_0^2 (a_{ix} a_{jx} e^{j(\theta_{ix} - \theta_{jx})}) \quad \alpha = 0 \quad (2.34)$$

$$m_{i,j} = s_0^2 (a_{iy} a_{jy} e^{j(\theta_{iy} - \theta_{jy})}) \quad \alpha = \frac{\pi}{2} \quad (2.35)$$

From the measurements the calibration coefficients are obtained using the following equations [2.36-2.39]:

$$a_{ix} = s_0^{-1} \sqrt{m_{ii}(0)} \quad (2.36)$$

$$a_{iy} = s_0^{-1} \sqrt{m_{ii}(\frac{\pi}{2})} \quad (2.37)$$

$$\theta_{ix} - \theta_{jx} = \arctan \left(\frac{\text{Im}(m_{ij}(0))}{\text{Re}(m_{ij}(0))} \right) \quad (2.38)$$

$$\theta_{iy} - \theta_{jy} = \arctan \left(\frac{\text{Im}(m_{ij}(\frac{\pi}{2}))}{\text{Re}(m_{ij}(\frac{\pi}{2}))} \right) \quad (2.39)$$

Note that at this point we only have relative phases available so we will select the probe with the biggest magnitude to be $\theta = 0^\circ$ since this will have the larger correlation with the input signal. The other phase values are then known and set relative to this reference. In total this gives us all the gain matrix entries for the matrix G .

Note that it is also possible for a given set of cross-products to be internally inconsistent. This is because there is more information available in the cross-products than is needed to fill in all the unknowns of the linear gain matrix. If there is some systematic error in the determination of the cross-products (such as an offset in the samplers), then the same gain terms derived from different cross-products may not always agree. A last check that has to be done is to see whether the resulting phase and gain matrix are indeed valid and consistent. Therefore we have implemented the two tests proposed in [5]. These checks are presented in equations 2.40 and 2.41:

$$|m_{ij}(\alpha)|^2 = |m_{ii}(\alpha)||m_{jj}(\alpha)| \quad (2.40)$$

$$\angle m_{ik}(\alpha) = \angle m_{ij}(\alpha) \angle m_{jk}(\alpha) \quad (2.41)$$

So far the rough calibration is sufficient to obtain precise reconstruction of the polarization vector S . Up to now, we have taken two measurements, first with the input aligned with the x axis ($\alpha = 0$), and the second with the input aligned with the y axis ($\alpha = 90$). This is sufficient to characterize the analog Front-End and constitute the first approach to meet the Calibrated DOMT. However two issues remain. First, the relative phase between the x and y columns has not been determined. The second issue has to do with the orthogonality of the x and y calibrators. In fact, a fraction of a degree of axial misalignment introduces cross-polar leakage on the order of -40dB . Therefore the solution lies in recognizing that if the axes x and y are orthogonal or not, then any attempt to synthesize circular polarization will result in measurable ellipticity[5].

2.3.1. Third calibration measurement at $\alpha = \frac{\pi}{4}$

This calibration consists in measuring the OMT output voltages with the input transition rotated 45° . For this test, a frequency sweep is done at each spectral channel in the desired RF band. For each frequency channel, the complex frequency vector V is computed via Fast Fourier Transform (FFT) algorithm, and stored in memory. Then, the elements of G can be computed in an offline manner, where the exact mathematical equations can be presented [5]. Then, G is used to compute the correction matrix H' by equation (2.30) to $\alpha = 45^\circ$. Once we obtained the estimated values of given the partially calibrated matrix, we compute S' , using the equation 2.42:

$$S' = H'V \quad (2.42)$$

Therefore, the output voltage vector must be the same whether we pair the real input signal vector, S , with the correct gain matrix, G , or the estimated signal vector, S' , with the partially calibrated gain matrix, G' . Allowing for an x versus y phase differential of ϕ and a misalignment of the axis y of ε , we can write

$$G'S' = G'\Phi ES$$

$$G'\Phi ES = G' \begin{bmatrix} 1 & 0 \\ 0 & e^{j\phi} \end{bmatrix} \begin{bmatrix} 1 & \sin \varepsilon \\ 0 & \cos \varepsilon \end{bmatrix} \begin{bmatrix} \cos \alpha \\ \sin \alpha \end{bmatrix} s_0 e^{j\beta} \quad (2.43a)$$

$$S' = \Phi ES = \begin{bmatrix} \cos \alpha + \sin \varepsilon \sin \alpha \\ e^{j\phi} \cos \varepsilon \sin \alpha \end{bmatrix} s_0 e^{j\beta} \quad (2.43b)$$

Linear polarizations may be converted to circular polarizations by observing that

$$\begin{bmatrix} s_l \\ s_r \end{bmatrix} = \begin{bmatrix} 1 & -j \\ 1 & j \end{bmatrix} \begin{bmatrix} s_x \\ s_y \end{bmatrix} \quad (2.44a)$$

$$\begin{bmatrix} s_x \\ s_y \end{bmatrix} = \frac{1}{2} \begin{bmatrix} 1 & 1 \\ j & -j \end{bmatrix} \begin{bmatrix} s_l \\ s_r \end{bmatrix} \quad (2.44b)$$

and solving for a new pseudo-inverse matrix

$$H_{circular} = \begin{bmatrix} 1 & -j \\ 1 & j \end{bmatrix} H_{linear} \quad (2.45)$$

Using (x-y to L-R) we determine the estimated circular components, converting from linear polarization to circular. We may also rotate the linear polarization to any orientation angle, Ψ , regarding the major axis:

$$H_{\Psi} = \begin{bmatrix} \cos \Psi & \sin \Psi \\ -\sin \Psi & \cos \Psi \end{bmatrix} H_{linear} \quad (2.46)$$

Using the equation 2.44a, we determine the estimated circular components s'_l and s'_r from the equation 2.43b. In order to solve the orthogonality and phase terms ε and ϕ , using the equation 2.43a, we can derive the value of ε , given equation 2.47 [5]:

$$\sin \varepsilon = \frac{1}{2} s_0^{-2} \left(\left| s'_l \left(\frac{\pi}{4} \right) \right|^2 + \left| s'_r \left(\frac{\pi}{4} \right) \right|^2 \right) - 1 \quad (2.47)$$

In the case of the orthogonality term ε , the value tends to zero because expected value of ε is equal or at least tends to $\frac{\pi}{2}$, so the $\cos(\varepsilon) \approx 1$, and the principle value of the arcsin is the correct one. In fact those results means the polarization is linear because the polarization angle is 45 degrees, therefore the ellipticity angle is 0. To calculate $e^{j\phi}$ in equation 2.43a, we compute first the $\sin \phi$ given equation 2.48:

$$\sin \phi = s_0^{-2} \frac{\left(\left| s'_l \left(\frac{\pi}{4} \right) \right|^2 - \left| s'_r \left(\frac{\pi}{4} \right) \right|^2 \right)}{\sin 2\varepsilon + 2 \cos \varepsilon} \quad (2.48)$$

And finally, to calculate $\cos \phi$ given equation 2.49:

$$\cos \phi = \frac{2s_0^{-2} \text{Im} \left[s'_r \left(\frac{\pi}{4} \right) s'_l * \left(\frac{\pi}{4} \right) \right]}{\sin 2\varepsilon + 2 \cos \varepsilon} \quad (2.49)$$

The x versus y phase differential, ϕ , can have different values depending on the choice of reference probes. So to resolve the ambiguity, the orthogonal terms ($\sin \phi$ and $\cos \phi$) should be computed. Once the rotations matrices' terms are computed, we may apply them to gain matrix by multiplication to obtain G final as presented in equation 2.50.

$$G = G'\Phi E = G' \begin{bmatrix} 1 & 0 \\ 0 & e^{j\phi} \end{bmatrix} \begin{bmatrix} 1 & \sin \varepsilon \\ 0 & \cos \varepsilon \end{bmatrix} \quad (2.50)$$

Finally, in order to validate the correct working of the digital polarization synthesis we synthesize the polarization vectors in two ways: calibrated with an ideal Gain matrix and calibrated with the Gain matrices resulting from the three measurement calibration procedures described above. To synthesize the polarization vectors the complex frequency vector V is multiplied with the pseudo-inverse of the gain matrices from the three measurements, H , obtaining S_x and S_y , that constitute the final polarization in either the x or y direction according to the equation 3.1.

$$\begin{bmatrix} s_x[n] \\ s_y[n] \end{bmatrix} = \begin{bmatrix} H_{11}[n] & H_{12}[n] & H_{13}[n] & H_{14}[n] \\ H_{21}[n] & H_{22}[n] & H_{23}[n] & H_{24}[n] \end{bmatrix} \begin{bmatrix} V_{11}[n] \\ V_{21}[n] \\ V_{31}[n] \\ V_{41}[n] \end{bmatrix} \quad (2.51)$$

For instance, an ideal (uncalibrated) digital OMT may be implemented, loading the ideal H matrix (eq. 4.1) into the DOMT.

$$[H_4] = \begin{bmatrix} \frac{1}{2} & 0 & \frac{-1}{2} & 0 \\ 0 & \frac{1}{2} & 0 & \frac{-1}{2} \end{bmatrix} \quad (2.52)$$

2.4. Digital Orthomode Transducer Architecture

The Digital Orthomode Transducer Architecture is based on a new trend called digitally calibrated receivers for radioastronomy using a combination of careful analog design and digital signal processing to achieve wideband downconversion. Passing some functionality from the analog Front-End to the digital Back-End to improve the performance of purely analog receivers[22]. These receivers allow digital sampling of the radio frequency (RF) signal as close to the antenna connection or focal point as possible[13].

In the following subsections the operation principle of the analog Front-End and the digital Back-End used in this project will be discussed.

2.4.1. Front-End

In Figure 2.4 a Dual Side Band (DSB) receiver is presented. This receiver is responsible for capturing, amplifying and down-converting the signal under study.

The first element is a Horn antenna that collect radiation coming from distant astronomical objects. The radiation collected by the Horn is conducted through a wave-guide to a Low Noise Amplifier (LNA) where the signal is amplified adding some noise. The noise temperature of the radio astronomical receiver is highly dominated by the noise figure of its first amplifying stage. Then the RF signal is mixed using a non-linear device (diode, transistor) called a mixer with a reference signal fine tuned to a specific frequency, called Local Oscillator (LO). They convert the incoming RF signal into a lower frequency, called Intermediate Frequency (IF) signal, maintaining the phase and amplitude of the original signal.

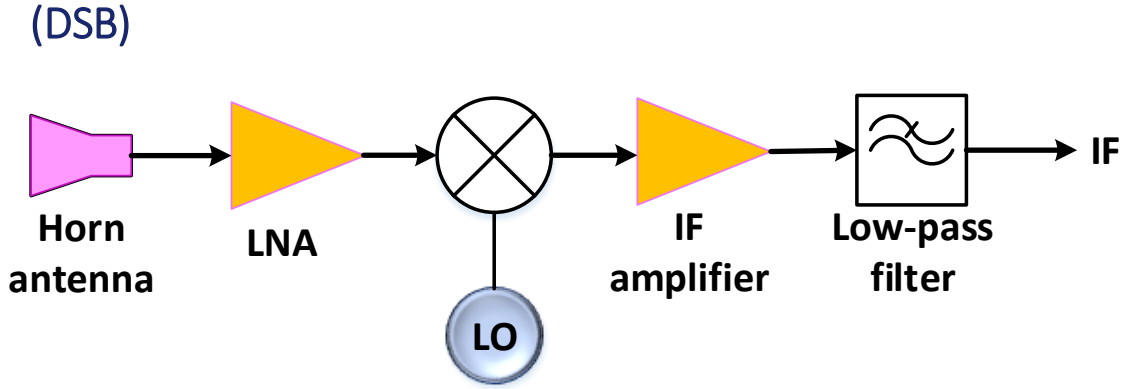


Figure 2.4. Typical configuration of a Dual Sideband mixer (DSB). The input is an RF signal which is first amplified and mixed. The resulting signal is filtered and amplified again, in order to obtain the IF signal which is easier to post-process than the original RF signal.

Afterwards, the IF signal is amplified and filtered using an anti-aliasing filter (Low pass filter) in order to make the digital signal processing as easy as possible, hereafter the IF signal is ready to be digitized using Analog to Digital converters (ADC).

The frequency mixing process of a DSB heterodyne radio receiver is shown in Figure 2.5, where a frequency domain representation is presented to understand its performance. The Radio Frequency (RF), composed by the Lower Side Band (LSB) and the Upper Side Band (USB) signals, is down-converted to base band. After down-conversion the USB and LSB are overlapped in the IF band. To overcome the overlapped spectra problem a 2SB receiver is always preferable but much more complex [22].

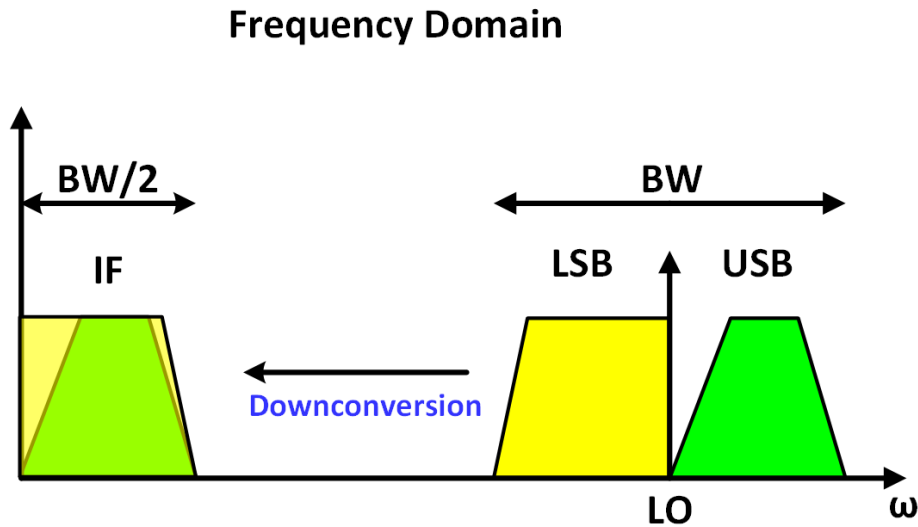


Figure 2.5. Frequency mixing process. After down-conversion the USB and LSB are overlapped in the IF band.

2.4.2. Back-End

The back ends are devices that analyze the polarization, time structure or spectral properties of the broadband radiation. The trend has been toward digital components for all types of back ends. Frequently these components are developed for use in telecommunication systems, however have been successfully adapted for higher frequency bands suitable for radio astronomical applications. Because signal information (phase and amplitude) should be preserved coherent spectrometers were implemented in the DOMT [23].

The hardware used in this project to implement the digital back-end is a ROACH-2 Revision 2 (Reconfigurable Open Architecture Computing Hardware), this is a standalone FPGA processing board [17].

In 2010 we identified the fast growing trend of digitalization and joined the 'Colaboration for Astronomy Signal Processing and Electronic Research - CASPER', led by UC Berkeley and acquired ROACH boards, an FPGA based platform for ADC interfacing, to research the next generation of radio astronomy instruments by passing some functionality from the analog domain to the digital domain [24].

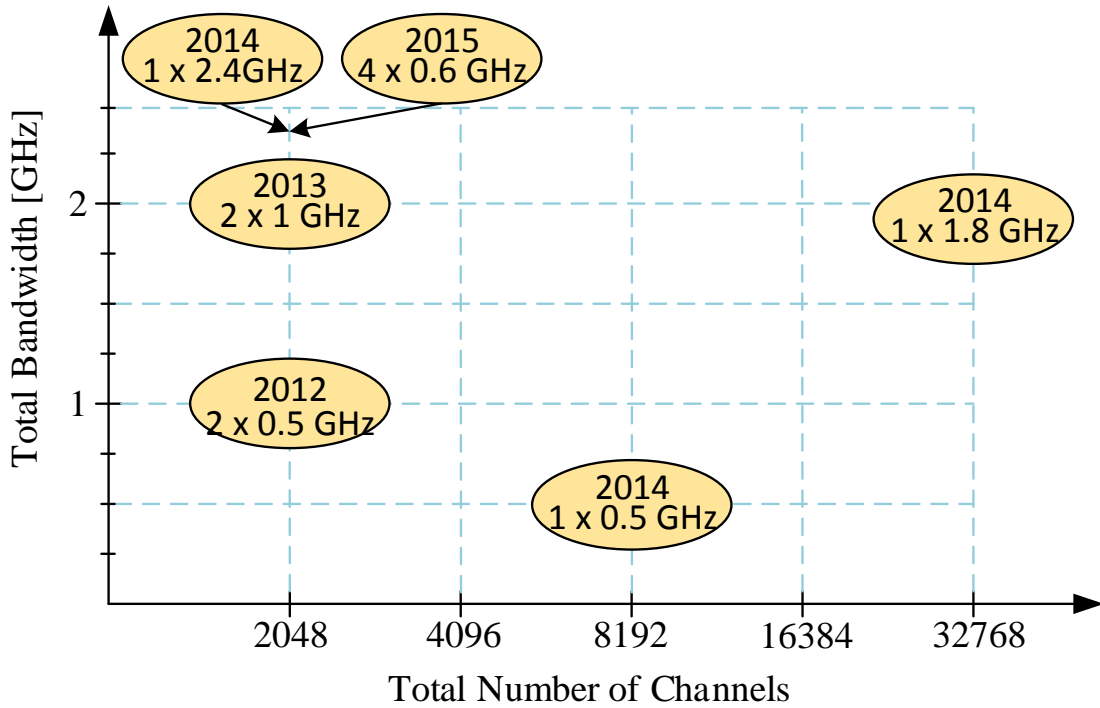


Figure 2.6. Overview of the Fast Fourier Transform Spectrometers developed at the Millimeter Wave Laboratory, University of Chile. From 2012 to 2013 the Spectrometers were developed using ROACH-I. In following years it was possible to improve the bandwidths, the number of channels and the number of IF bandwidth processed in parallel by means of a ROACH-II.

Custom PFB spectrometer back-ends optimized for a wide range of radio astronomical applications were developed [24]. Figure 2.6 presents the development history of digital wide-band

Polyphase Filter Banks in the MWL, University of Chile. So far, the largest spectrometer implemented in ROACH-II was achieved in 2014 with a spectrometer with a total bandwidth of 2,5 GHz and 65536 spectral channels [25].

2.5. Spectrometers and Polyphase filter Bank

Spectrometers are the Back-End systems most used in the radio astronomy [23].

The spectrometers allow the realization of spectral analysis for data in frequency domain, allowing to know the phase, magnitude and frequency of a signal in the band under study. Spectrometers are designed to measure the spectral density of a signal, which corresponds to the power distribution of the signal on the different frequencies which are formed, that is, its spectrum. This is known as the power spectral density or PSD.

There are two ways in which the PSD of a signal may be computed. The power spectrum, S_{xx} , of a waveform and its autocorrelation function, r_{xx} . They are related by the Wiener-Khinchin theorem [2] as presented in Figure 2.7.

When the spectrum of a periodic signal is calculated the result is a discrete frequency, i.e. a spectral line of zero bandwidth. Instead, when the spectrum of a random signal is analyzed, it is found to be distributed continuously in a frequency band. In this case it makes no sense to question the magnitude of the spectrum at a certain frequency (since the answer is always zero), but by the RMS value or the signal strength in a frequency band.

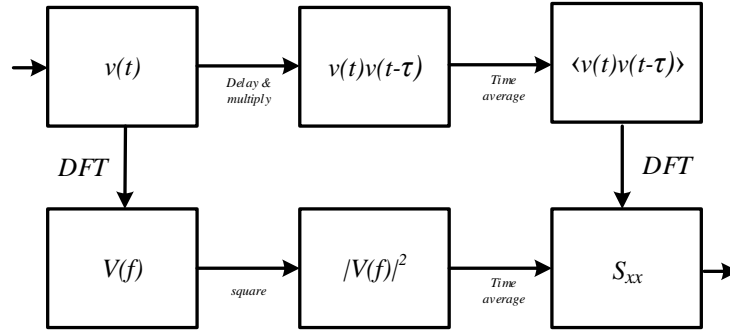


Figure 2.7. The two methods used to compute the PSD of a signal. The top path corresponds to an Auto-Correlation Spectrometers (ACS) system while the bottom corresponds to an Fourier Transform Filterbanks (FTF) system. The two approaches are related by the Wiener-Khinchin theorem.

Furthermore, the phase information is irrelevant in the case of a random signal. Unless the noise signal is correlated [2].

Usually in signal analysis we normalize the power by the value of the resistance to $1[\Omega]$. In this case, $p(t) = (x(t))^2$ where $x(t)$ can be a voltage or a current.

Thus, for a time sequence $x(n)$, the instantaneous power is: $p(t) = (x(t))^2$. Since energy is the accumulation over time of instantaneous power, the total energy of a sequence $x(n)$ is

presented in equation 2.53.

$$E = \sum_{n=-\infty}^{\infty} |x(n)|^2 \quad (2.53)$$

The average power of the sequence is the average of the instantaneous power:

$$P = \lim_{n \rightarrow \infty} \frac{1}{2N} \sum_{n=-N}^N |x(n)|^2 \quad (2.54)$$

The RMS value of a sequence is the magnitude of current or a voltage which produces the same average power dissipation of a load that produces the sequence. The average power produced by the RMS value of the sequence is:

$$P = x_{RMS}^2 \quad (2.55)$$

Equating the average power produced by the sequence and the RMS value of it, the formula is obtained to calculate the RMS value of a sequence:

$$x_{RMS} = \sqrt{\lim_{n \rightarrow \infty} \frac{1}{2N} \sum_{n=-N}^N |x(n)|^2} \quad (2.56)$$

In general, periodic and random sequences length sequences (noise) are power, while non-periodic sequences of short duration (transient) are energy sequences. For example, the effect of background noise on the reception of a radio signal is directly related to noise power. While the higher the noise power, the more difficult the signal reception.

We can prove that the above results are generating a noise sequence (normal distribution and flat spectrum) and compare the calculation result of the power in the time and frequency domain. We should note that the results are equals in both time and frequency domain.

The primary subsystem used in this work is a spectrometer based on the Fast Fourier Transform (FFT) algorithm [2]. The FFT is an algorithm mathematically optimized (i.e. fewest possible number of butterflies) to compute the Discrete Fourier Transform (DFT). The FFT used in this work is suitable for continuous integration and real-time computation of spectra. We implemented our spectrometers using the radix-2 FFT generator developed by CASPER at UC Berkeley.

The DFT coefficient $X[k]$ is defined according the equation 2.57. Where $W_N = \exp(-j\frac{2\pi}{N})$ is the first of the N-th roots of unity and $x[n]$ is the digitized signal [26].

$$X[k] = \sum_{n=0}^{N-1} W_N^{nk} x[n] \quad 0 \leq k \leq N-1 \quad (2.57)$$

The DFT is an algorithm that play a crucial role in many digital signal processing applications, such as spectrum analysis of signals, power spectrum estimation, and linear filtering [2]. One of the most important features of the DFT operation is as a tuned filter bank with evenly spaced frequencies in the band analysis. If the sequence is random, each of these filters gives an output whose power is proportional to bandwidth of the filters, which allows to estimate the power density through the following relationship:

$$P(k) = \frac{1}{N} |X(k)|^2 \quad 0 \leq k \leq N-1 \quad (2.58)$$

Spectrometer Parameters:

- Bandwidth: The frequency spectrum width in Hz. This is in function of the sampling rate. For complex sampled data this is equivalent to equation 2.59:

$$BW = F_{Sampling} \quad (2.59)$$

In contrast, in equation 2.60 with Nyquist sampled data the rate is half this, for real sampled data.

$$BW = \frac{F_{Sampling}}{2} \quad (2.60)$$

- Frequency resolution: The frequency resolution of a spectrometer, is given by the equation 2.61 and is the width of each frequency bin.

$$\Delta f = \frac{BW}{N^{\circ} Channels} \quad (2.61)$$

- Time resolution: Time resolution is the spectrometer spectral dump rate. In general we accumulate multiple spectra to average out noise. The radiometer equation 2.62, describes how the uncertainty in measuring a noise temperature decreases as the square-root of the number of samples averaged together:

$$\sigma = \frac{T_{sys}}{\sqrt{BWt}} \quad (2.62)$$

where σ is the residual (root-mean-square) uncertainty in a noise temperature measurement, T_{sys} is the noise temperature of a system, Bw is the bandwidth over which a single measurement is made, i.e. the integrated bandwidth and t is the time over which a measurement is averaged.

A handy equation to determine the integration time of the Spectrometers, which it is in function of the FFT window, for parallel FFT, i.e. presented in equation 2.63:

$$FFT \text{ window} = \frac{N^{\circ} \text{ of } FFT \text{ Channels}}{N^{\circ} \text{ of } FFT \text{ Outputs}} \quad (2.63)$$

Finally, the integration time for parallel spectrometers implemented using FPGA technology can be computed according the equation 2.64:

$$Integration \text{ Time} = (FFT \text{ window}) \times (N^{\circ} \text{ Acc}) \times (clock \text{ period}) \quad (2.64)$$

2.5.1. Polyphase Filter-Bank: PFB

A polyphase filterbank (PFB) is simply an efficient computational structure used to form a bank of filters. All that is required to form a PFB is to place a “prototype polyphase filter structure” in front of an FFT. The frontend enhances the filter response of the FFT, making it better by using time samples and filter coefficients.

The addition of the FIR before the FFT improves the frequency response of each channel making them flatter within each frequency bin, sharper on the edges, and strongly reducing the inter-channel leaking. Figure 2.8 shows a comparison of the single-bin frequency response of a PFB with a direct FFT.

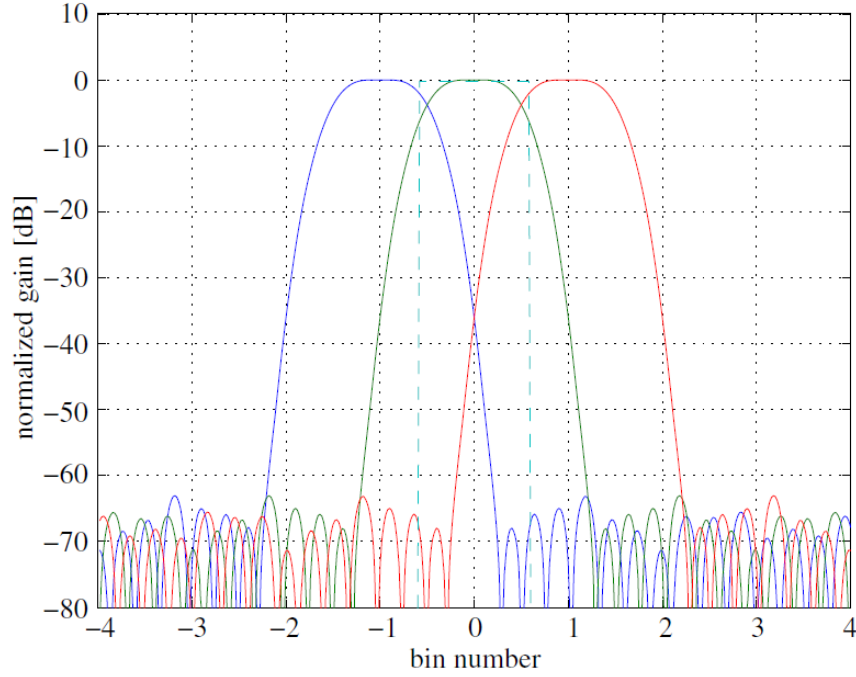


Figure 2.8. Comparison of the channel response of an Auto-Correlation Spectrometer (ACS, dotted line), Fourier Transform Filterbank (FTF, dashed line) and an 8-tap, Hann-windowed Polyphase Filter Bank(PFB, solid line) [2].

2.6. Digital Implementation

The spectrometers used in radio-astronomy are based on mixed technologies, first with an A/D converter and then with a processor capable of applying DSP algorithms on it. The spectrometers that were implemented on the DOMT utilize ADC interfacing with the Xilinx FPGA Virtex-6 [27] due to the computing power its architecture provides and to interface over Ethernet network to extract data easily.

During the recent past, embedded hard blocks (HBs) in FPGAs (i.e., heterogeneous FPGAs. For example the Virtex-6 is equipped with embedded blocks of Multipliers [28] and RAMs) have become increasingly popular for DSP due to their ability to implement complex applications more efficiently as compared to homogeneous FPGAs technologies (i.e., pure combinational logic, Flip-Flops, Latches, to name a few) [29].

This section describes the ADCs, and FPGAs available in the MWL. Finishing with the description of the FPGA Design Flow used to synthesize and implement a design on the ROACH-II.

2.6.1. The ADC

Most modern implementations of spectrometers in radio astronomy are PFB based and use commercially available high-speed ADCs. Over the years, ADC input bandwidth has grown from kilohertz to the gigahertz we see today. Specifications of some example high-speed ADCs that are currently available in the laboratory are given in Table 2.1: To characterize ADCs

Table 2.1: High-speed ADCs that are currently available at the MWL.

Sample rate [Samples/second]	number of bits	number of inputs	Chip Brand	Chip Part Number
3 GSPS	8	2	National Semiconductor	ADC083000
5 GSPS	8	2	e2v	EV8AQ160
250 MSPS	8	16	Analog Devices	HMCAD1511

performance the following metrics are being used: Frequency response, SFDR (Spurious Free Dynamic Range), SINAD (Signal-to-noise and distortion ratio) and ENOB (Effective number of bits) [25] (see Sec. 9.4 of the IEEE Standard (2010) [30]). The theoretical maximum Dynamic Range (DR) of an ADC in decibels is given by equation 2.65:

$$DR = 20 \log(2^{n_{bits}}) \approx 6.02 n_{bits} \quad (2.65)$$

In practice, as ADCs are imperfect analog devices, their effective number of bits (ENOB) is below this. For example, the 8-bit ADC5GSPS available in ROACH-II have an ENOB of 7.5, thus resulting in a dynamic range of 45 dB.

2.6.2. The FPGA

The *Field Programmable Gate Array (FPGA)* is an attractive platform for digital design due its flexibility. Initially, FPGAs were used to verify designs that would later be manufactured. Several innovations drive to FPGA vendors to integrate IP cores, ASIC-like circuitry into FPGAs. In the mid-1990s allowed FPGAs to compete with ASICs in digital signal and image processing.

FPGAs are used for low volume circuits that could not be profitable synthesized as an *Application Specific Integrated Circuit (ASIC)* [31]. The principal markets for FPGAs consist of the replacement of old ASICs available in wired communication systems and storage area networks. Integrated systems such as wired communications, storage control, wireless communications, defense, and digital signal and image processing. The FPGAs vendors constantly increase the number of logic elements in the FPGAs to address those markets. Nowadays (2016) we can find over of two million or more logic elements as well as large number of IP cores available on a single FPGA chip [24].

In Figure 2.9 is shown the generic logic elements available in an FPGA, such as Configurable Logic Blocks (CLB), Connection blocks, wire segments, Switch Blocks, IO blocks, clocking resources, embedded memories and routing channels [32].

Configurable Logic Blocks (CLBs)

The Configurable Logic Blocks (CLBs) are the main logic resources for implementing sequential as well as combinatorial circuits. Each CLB element is connected to a switch matrix for access to the general routing matrix (shown in Figure 2.10). A CLB element contains a pair of slices. A Slice in Virtex-6 FPGA contains four look-up tables (LUTs), eight registers, a carry chain, and multiplexers [33].

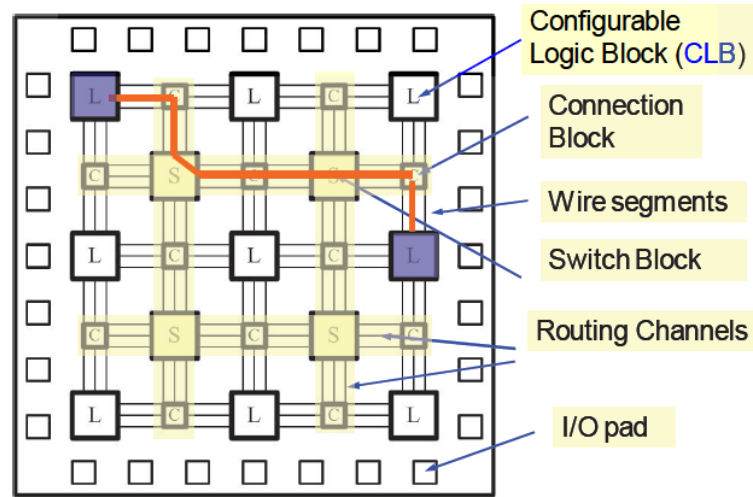


Figure 2.9. Generic FPGA architecture.

In Figure 2.11 the Virtex-6 FPGA CLB which is composed of two different Slice types: SLICEM and SLICEL. A SLICEM has a multi-purpose LUT, which can also be configured as a Shift Register LUT (SRL), or a 64- or 32-bit read-only or random access memory. Each Slice register can be configured as a latch. The connectivity between LUTs, registers, multiplexers, and a carry chain can be configured to form different logic circuits.

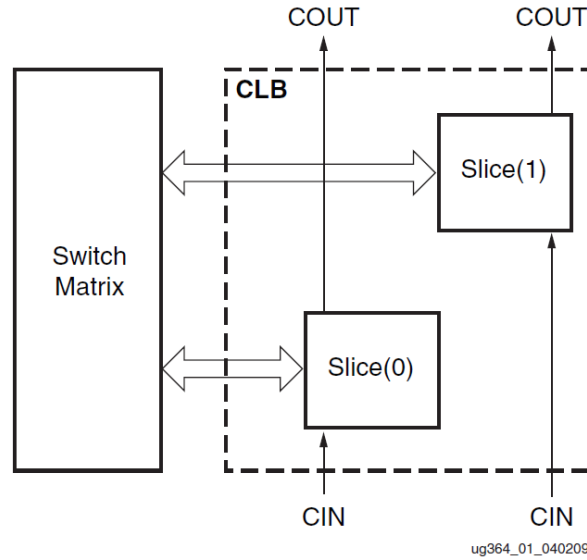


Figure 2.10. Disposition of Slices within the CLB [33].

Clocking resources

Each Virtex-6 FPGA provides a set of configurable mixed-mode clock managers (MM-CMs) [34], which are used for frequency synthesis and phase shifting. Clocks to different synchronous elements across FPGA are distributed using dedicated low-skew and low-delay clock routing resources. Clock lines can be driven by global clock buffers, which allow glitch-less clock multiplexing and the clock enable [35].

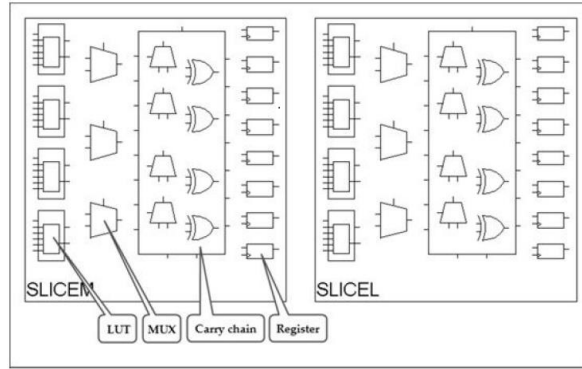


Figure 2.11. Xilinx Virtex-6 FPGA Slice structure. A Slice in Virtex-6 FPGA contains four look-up tables (LUTs), eight registers, a carry chain, and multiplexers. The above snapshot is taken from PlanAhead tool which is part of ISE Design Suite System Edition.

Block RAM (BRAM)

Xilinx FPGAs have two types of embedded memories: a dedicated Block RAM (BRAM) primitive, and a LUT configured as Distributed RAM. Virtex-6 BRAM can store 36K bits, and can be configured as a single- or dual-ported RAM. Other configuration options include data width of up to 36-bit, memory depth up to 32K entries, and error detection and correction [27].

Block DSP - DSP48E1 Slice

Virtex-6 FPGAs provide dedicated Digital Signal Processing (DSP) primitives to implement various functions used in DSP applications, such as multipliers, accumulators, and signed arithmetic operations. The main advantage of using DSP primitives instead of general-purpose LUTs and registers is high performance [28]. Each DSP48E1 slice fundamentally consists of a dedicated 25 x 18 bit two's complement multiplier and a 48-bit accumulator, both capable of operating at 600 MHz [27].

Input/Output

Input/Output (IO) block enables different IO pin configurations: IO standards, single-ended or differential, slew rate and the output strength, pull-up or pull-down resistor, digitally controlled impedance (DCI). An IO in Virtex-6 can be delayed by up to 32 increments of 78 ps each by using an IODELAY primitive [27].

Routing resources

FPGA routing resources provide programmable connectivity between logic blocks, BRAM, DSP, IOs and other modules. Routing resources are arranged in a grid. A special interconnect module serves as a configurable switch box to connect logic blocks, BRAM, DSP, IOs and other modules to horizontal and vertical routing. Unfortunately, Xilinx doesn't provide much documentation on performance characteristics, implementation details, and quantity of the routing resources. Some routing performance characteristics can be obtained by analyzing timing reports.

FPGA configuration

The majority of modern FPGAs are Static Random Access Memory (SRAM) based, including Xilinx Virtex families. On each FPGA power-up, or during a subsequent FPGA reconfiguration, a bitstream is read from the external non-volatile memory (NVM), processed by the configuration controller, and loaded to the internal configuration SRAM [35].

In Table 2.2 a comparison of the Virtex-5 and Virtex-6 Xilinx FPGAs is presented. The Virtex-6 has more resources than Virtex-5. For instance, there are 488 BRAMs 18Kb or 244 BRAMs 36Kb Virtex-5 and in contrast, in Virtex-6 there are 2128 BRAMs with 18Kb or 1064 BRAMs with 36Kbits, i.e. x4 times larger.

Table 2.2: FPGAs comparison: Virtex-5 [36] vs. Virtex-6 [27].

	Virtex-5	Virtex-6
	XC5VSX95T-1FF1136	XC6VSX475T-1FFG1759C
Logic Cells	14,720	476,160
Embedded memory (Kbits)	1,520	7,640
DSP modules	640	2,016
Block RAM Blocks		
Max (Kbits)	8,784	38,304
Max User Input/Output	640	840
	ROACH-I	ROACH-II

2.7. The Casper Toolflow and Xilinx Build Flows

The CASPER flow is a process which refers to a sequence of steps to build an FPGA design from a Simulink model to a BORPH¹ executable. Figure 2.12 presents the compilation stages of CASPER Toolflow which is based in the Standard Xilinx FPGA build Flow. The output file in each step during the CASPER flow is used as input in the next compilation stage, they are accompanied by reports to help to the designers to analyze the quality of results (QoR) in their designs to completion and to achieve their timing constraints [37].

¹BORPH: Berkeley Operating system for ReProgrammable Hardware. Source: <https://www.eee.hku.hk/~hso/borph.html>

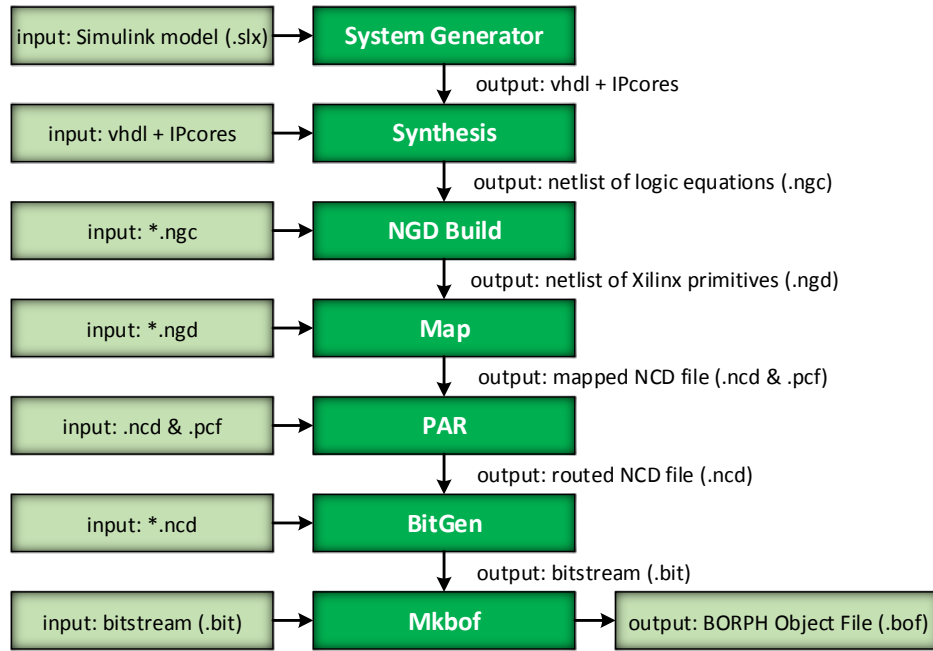


Figure 2.12. Casper Toolflow.

The Xilinx FPGA flow contains six fundamental steps as shown in Figure 2.13: synthesis, ngdbuild, map, place-and-route, static timing analysis, bitgen [38].

Synthesis is the process by which we map a generic Register-Transfer Level (RTL)² to a target FPGA architecture. The ISE[®] Design Suite includes Xilinx Synthesis Technology (XST) allowing synthesis of HDL designs to create netlist files.

NGDBuild reads in a netlist file of logic equations in EDIF or NGC format and creates a Xilinx Native Generic Database (NGD) file that contains a logical description of the design in terms of logic elements, such as AND gates, OR gates, LUTs, flip-flops, and RAMs.

Map stage maps a logical design to a target Xilinx FPGA architecture. The input to MAP is an NGD file, which is generated using the NGDBuild program.

Place-and-Route (PAR or PnR) takes output file of the MAP program the Native Circuit Description (NCD) file to place and route that design file using Xilinx PAR algorithm into a target FPGA architecture.

Static Timing Analysis (STA) is a method of validating the timing performance in a digital logic by checking all timing violations under worst-case conditions. It considers worst possible delays along a timing path (both gate and interconnect) and comparing it with constraints (clock period) to check whether the path meets the constraint [39].

Bitgen is a Xilinx command line tool that generates a bitstream for Xilinx device configuration. BitGen takes a fully routed Native Circuit Description (NCD) file as input and produces a configuration Bitstream (BIT) file as output. A BIT file is a binary file with a .bit extension [38]. After synthesis the entire implementation process is performed by FPGA vendor tools. The FPGA physical implementation is composed of Ngdbuild, Map, PAR, and bitgen steps and they depend on the specific FPGA architecture [38].

²In digital design, the RTL is a model in which we focus in the transfer data from one register to another.

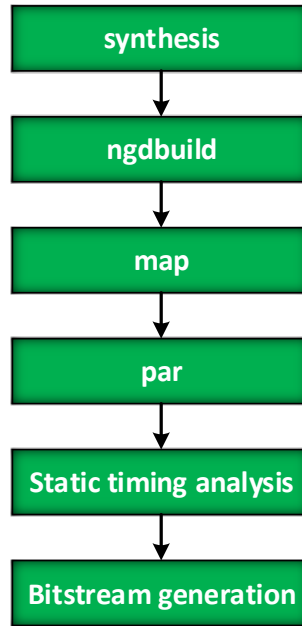


Figure 2.13. General Xilinx FPGA build flow.

Only Synthesis can be performed using third party software, for example, Synopsys' Synplify product. During the synthesis, designers may use the Xilinx XST tool or a third-party offering. The major third-party synthesis tools for general-purpose FPGA design are Synopsys' Synplify Pro and Mentor Graphics' Precision.

Intellectual Property (IP) cores developed by other companies which offers the latest IP solutions could be included to the netlist during synthesis [37].

Modern synthesis Tools improving the *Quality-of-Results* (QoR) and compilation runtime, by means of multi-core processing, of digital designs using custom flows developed with different compilation strategies.

Then, the NGDBuild phase involves netlist translation using the NGDBuild tool, while the next step, map, involves mapping the netlist into FPGA-specific resources, such as slices, RAMs and I/Os, using the Xilinx MAP tool.

The PAR tool handles placement and routing, and the TRACE tool performs static timing analysis. Finally, the BitGen stage is the point in the design cycle at which FPGA bitstreams are generated.

Figure 2.14 presents the second standard Xilinx FPGA build flow using PlanAhead. The PlanAhead tool supports multiple flows and methodologies to help designers overcome a variety of challenges during design implementation. The types of challenges encountered depend primarily on the target application, project goals and priorities. For instance, in 2013 using the CASPER toolflow a timing optimization was performed with PlanAhead [40]. In that work the FPGA Virtex-5 (see Table [2.2]) was constrained using the floor-planning methodology via PlanAhead Tool to reduce the path delay post PAR. The result of this work reduced the period of the system clock from 8ns to 4ns and the Worst Negative Slack (WNS) to zero, that result impacted in a factor x2 in the ADC sampling rate obtaining a x2 Bw processed in real-time. The FPGA projects involve the optimization of the Area, Timing, and Power [38].

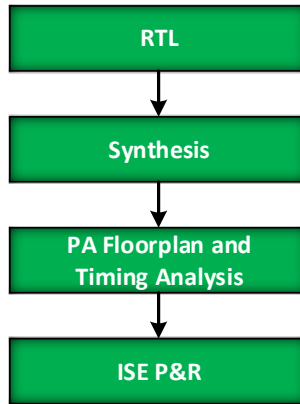


Figure 2.14. FPGA Design flow using PlanAhead.

The optimizations can be done following the methodologies such as Timing closure and Power management [38][39]. Timing closure methodology helps in meeting timing constraints. The power management methodology helps to obtain area goals defined for the user [37]. Nowadays (2015) to build a large FPGA design can take several hours, a day or even more. In order to overcome that problem, the FPGA designers use different methodologies applying digital design techniques customizing the build flows to meet the project requirements.

2.7.1. Digital design techniques

A recommended Timing Closure methodology³ consists in improving the QoR metrics Worst Negative Slack (WNS), and Timing Score⁴, as much as possible, by running different optimizations during Synthesis and Implementation stages to meet all timing constraints.

SmartXplorer command line tool delivering Timing Closure in the shortest amount of time with improved synthesis and implementation algorithms [37].

Depending on the size of the Simulink model we can estimate in function of the compilation runtime of a design how many days (or any unit of time) of effort it can take for a designer introduce a change and validate the result.

Electronic design automation (EDA) tools can run jobs in a GUI, and command-line mode (shell mode). The GUI approach enables a designer to use a pushbutton flow, which is convenient for small projects because GUI tools are expensive in memory and CPU resource utilization. However, when the Xilinx Tools In Command-line Mode [37] [35] are used the tools reduce their runtime [35], this approach permits easy implementation of whatever design flow using scripting languages. Through the EDA industry-standard TCL scripting language [37] it is possible to implement different build flows, following different methodologies, for instance timing closure, power optimization, congestion and custom optimizations.

³Timing closure is undoubtedly one of the most challenging aspects in modern FPGA design

⁴Timing score is the total time in picoseconds of all the paths that fail timing constraints.

2.8. Conclusions

In this chapter we have reviewed the most important concepts for this thesis. The calibration method was described mathematically which can accurately determine the amplitude and phase response of an OMT of four probes and automatically corrects for potential angular misalignments introduced by the manufacturing process of analog OMT.

The FPGA Virtex-6 architecture (see table [2.2]) and the ADC board ADC5GSPS (see table [2.1]) were introduced.

The compilation process of an RTL design to obtain a binary file to implement the model into a target FPGA, was defined as a flow. Mainly the CASPER tool flow was used to produce the binary file (boffile) needed to reconfigure the FPGA. The standard Xilinx FPGA Build and the PlanAhead flows were proposed, to optimize complex designs using Timing closure and Floorplanning methodologies [37].

Chapter 3

Digital Orthomode Transducer Design and Construction

This chapter presents the components that were designed and developed in the laboratory besides the components and devices that were bought to construct the Digital Ortho-Mode Transducer.

3.1. Hardware

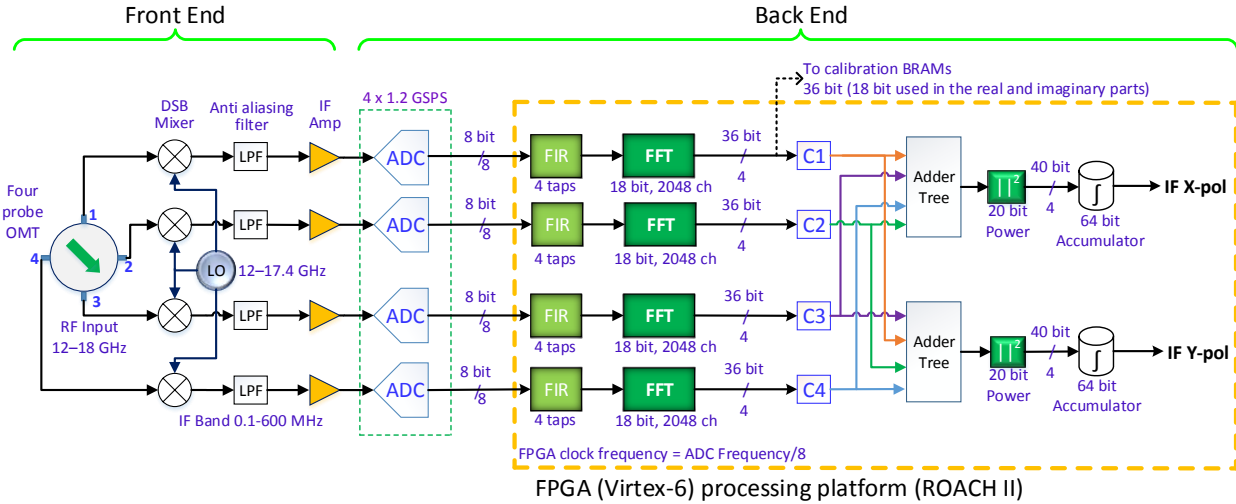


Figure 3.1. Digital Ortho-Mode Transducer block diagram. The front end was built out of commercial parts to provide the functionality of typical analog receivers.

Figure 3.1 shows the block diagram of the DOMT that is the subject of this thesis. The analog part of the DOMT consists of a circular waveguide with four probes of coaxial transition. Each output is connected to an independent receiver chain constituting its front end. The OMT's outputs are down-converted using mixers. The down-converted signals are filtered and amplified, then it is processed in the Back-End. The back end is a ROACH-II [16]

(Fig. 3.19) platform equipped with two 5 Gs/s (max) analog-to-digital converters (ADC) and a high performance FPGA (Virtex-6 XC6VSX475T-1FFG1759C) [27]. Four PFBs were implemented in parallel in the FPGA, in order to process the four IF outputs (600 MHz each) that comes from the front end.

In order to characterize the Front-end, the PFB outputs values are stored in calibration BRAMs. The calibration method described in section 2.3 is applied off-line using a python script that implements the equations presented to compute a set of calibration coefficients for each PFB channel.

The calibration coefficients are loaded into the FPGA. The calibrated DOMT is capable of compensating the imbalances of amplitude and phase of the analog front end. It was designed to synthesize the desired polarization vectors in real-time, with spectrometers capable of non-stop integration while maintaining high polarization isolation.

3.1.1. Analog OMT Design

The analog OMT design specifications are the following: Operation in Ku-band, have SMA coaxial probes, easy to build and miniaturize, reflections $S_{11} < -20\text{dB}$, cross-polarization $< -30\text{dB}$. The proposed specifications were satisfied by designing a circular waveguide with four probes of coaxial transitions. As shown in Figure 3.2, this design is very symmetrical and easily machined. The circular waveguide is a standard Ku band Hi circular waveguide with a diameter of 12.7mm. The probes are Pasternak PE4128 SMA connectors, where the length of the central pin and position of the connectors are optimized to meet the specifications.

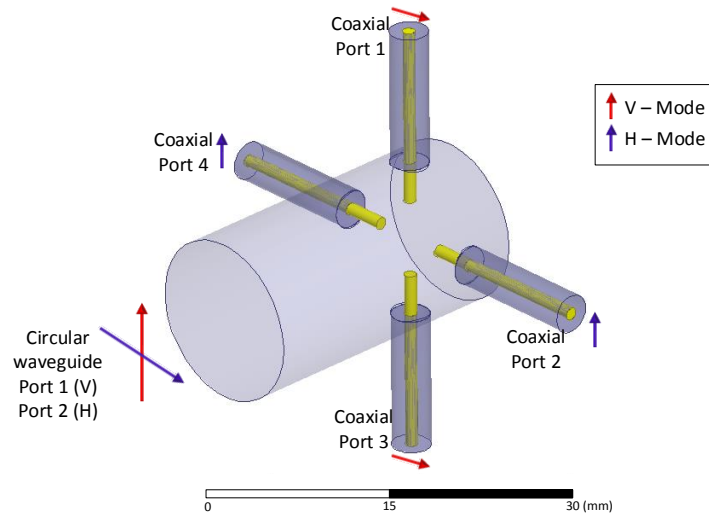


Figure 3.2. Circular waveguide to 4 coaxial probes OMT HFSS 3D model.

The model was simulated using ANSYS HFSS software (High Frequency Structural Simulator¹). The simulation of the OMT considers a discrete sweep of 6001 points with 1 MHz of resolution and the material properties of the aluminium ($\sigma = 38\text{MSiemmens} \times m$, $\mu_r = 1.000021$ and $\varepsilon_r = 1$). In Figure 3.3 the simulation results done for both polarizations are shown.

¹HFSS is a commercial finite element method solver for electromagnetic structures in the frequency domain [41].

The OMT has reflections (S_{11}) below -20dB from 12.8 GHz to 17.8 GHz, which covers 89% of the Ku band. The OMT presents two resonant peaks, one at 13.3 GHz and 17.3 GHz. These peaks are not wide, and have low amplitude, so they should not generate mayor problems in the measurements.

The cross polarization of the OMT is shown in Figure 3.5. We can see that cross polarization is around -50dB on average, but degrades around 14 and 17 GHz. The two resonant peaks that were present in the transmission and reflections are also present in the cross polarization.

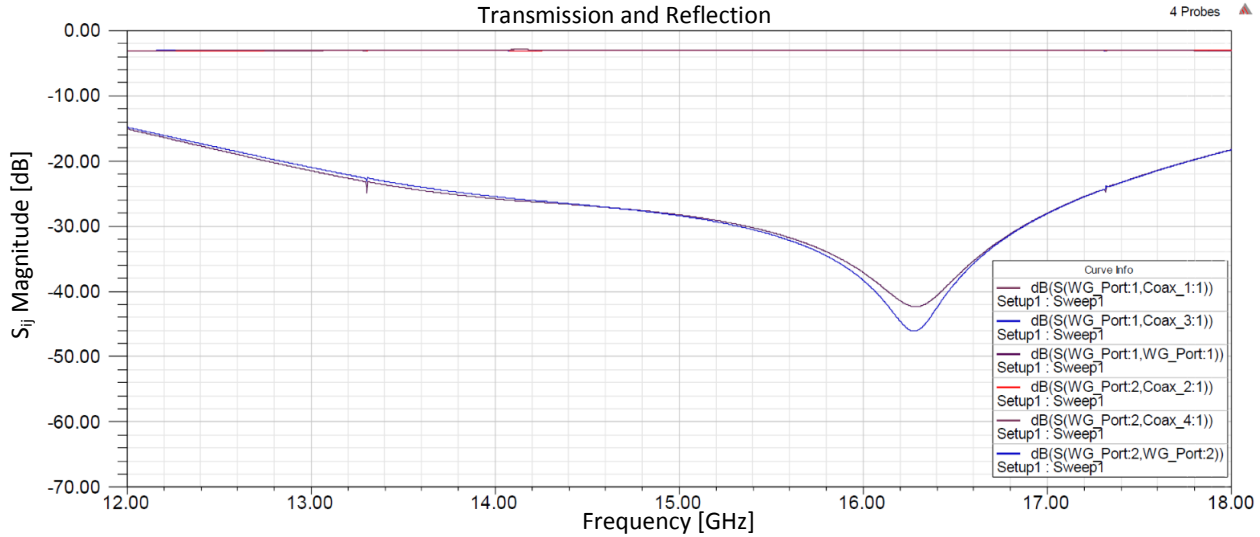


Figure 3.3. Circular waveguide to 4 coaxial probes OMT: Transmission and reflections. Simulated transmissions from the input port to all coaxial probes of the OMT. Simulated reflections at the input port of the OMT. $S(WG_Port:1, WG_Port:1)$ correspond to the reflection at the input port in V-mode (purple plot) and $S(WG_Port:2, WG_Port:2)$ is the reflection in H-mode (blue plot).

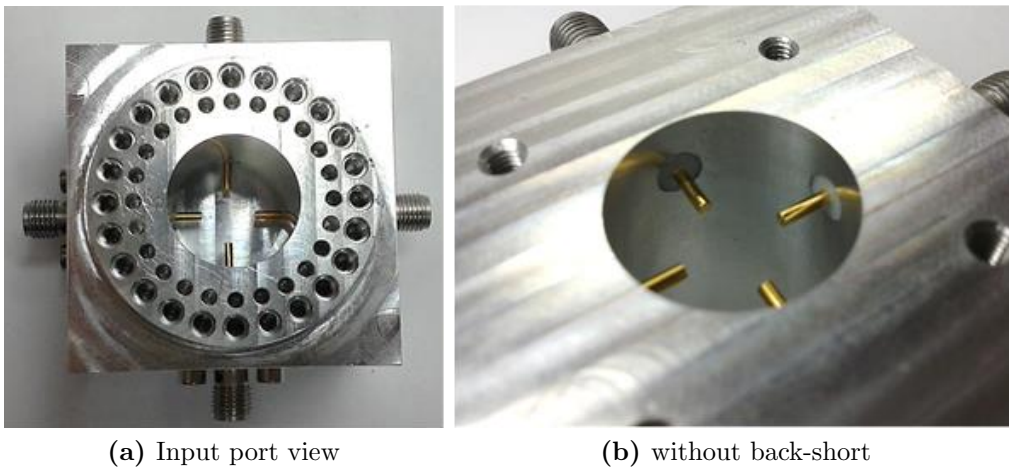


Figure 3.4. Four probes OMT manufactured in two aluminum blocks.

Once we meet the design requirements by HFSS simulation, the prototype was manufactured by José Pizarro using a CNC Milling Machine in two aluminum AL2017 blocks as shown in Figure 3.4.

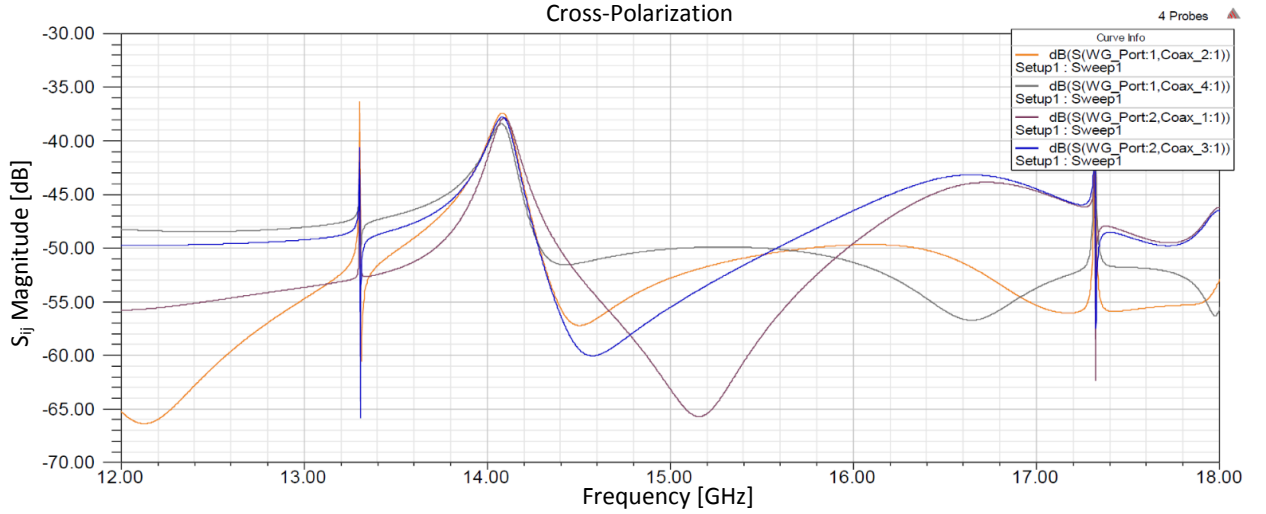


Figure 3.5. Simulated cross polar leakage of the OMT from the input port to the orthogonal ports. $S(\text{WG_Port:1,Coax_2:1})$ (orange plot), $S(\text{WG_Port:1,Coax_4:1})$ (gray plot), $S(\text{WG_Port:2,Coax_1:1})$ (purple plot), $S(\text{WG_Port:2,Coax_3:1})$ (blue plot).

3.1.2. Coaxial and waveguide transitions

In order to calibrate the OMT we need to design a coaxial-to-rectangular and a rectangular-to-circular waveguide transition. This hardware is required to inject a linearly polarized tone at different polarization angles, to then measure the amplitude and phase of each probe. The devices' general geometry is shown in Figure 3.6.

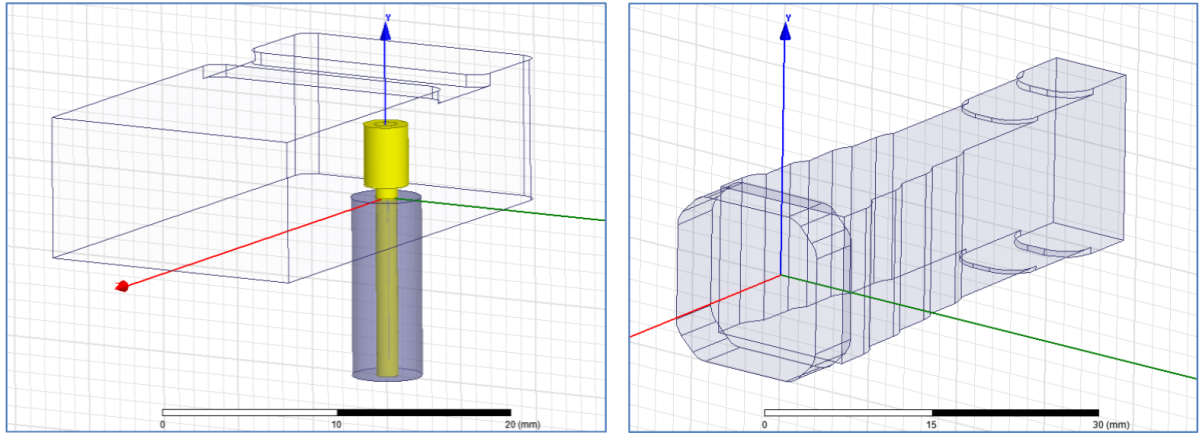


Figure 3.6. Coaxial to rectangular (left) and rectangular to circular (right) waveguide transitions design.

The performance reached after optimization is very good, with reflection below -20 dB for both transitions. The cross pol of the circular transition is below -60 dB, except for a few very narrow resonances. Results are shown in Figure 3.7.

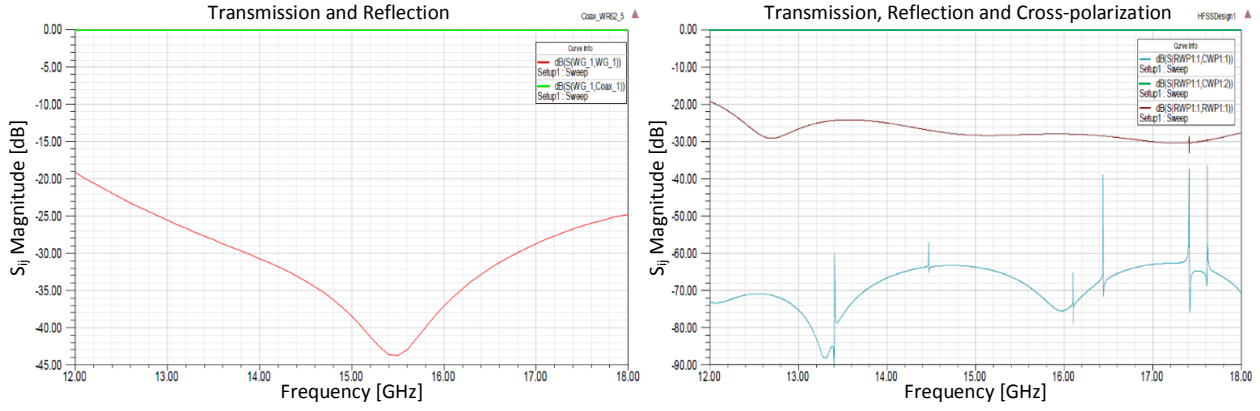


Figure 3.7. On the left, the simulation of the transmission and reflection of the coaxial to rectangular waveguide. On the right, the simulation of all characteristics of the rectangular to circular waveguide transition.

3.1.3. Full waveguide setup simulations

In order to inject an RF signal into the OMT a transition from coax to WR-62 waveguide was designed and constructed. Following that, a stepped taper from rectangular to circular waveguide provided a linear polarization, while an aluminum circular waveguide adapter allowed the interface at the flange to be rotated full-circle in 15° increments. The OMT with rectangular to circular waveguide transition and WR-62 to SMA waveguide transitions were simulated together in order to analyze its combined behavior using HFSS as shown in Figure 3.8.

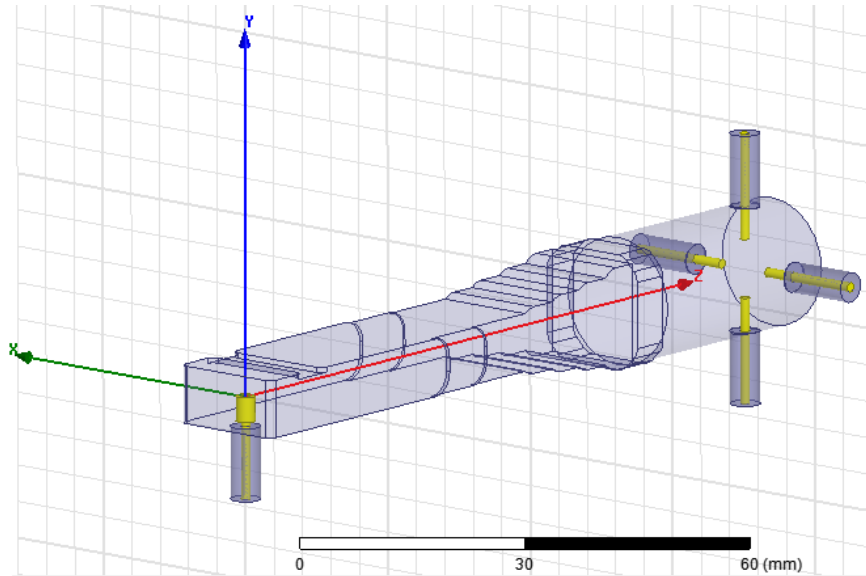


Figure 3.8. OMT + rectangular to circular waveguide transition + WR-62 to SMA transition.

In Figure 3.9 the whole system simulation results are presented. The transmission, reflection and cross polarization were simulated with a 1 MHz discrete sweep. Some minor parameters were optimized for better performance; these parameters include the dielectric position of the probes of the OMT, and some minor corrections (10 microns) in some of the transition dimensions. There is a good performance in almost all the Ku-band that meets the specified requirements and only two narrow resonant peaks are present.

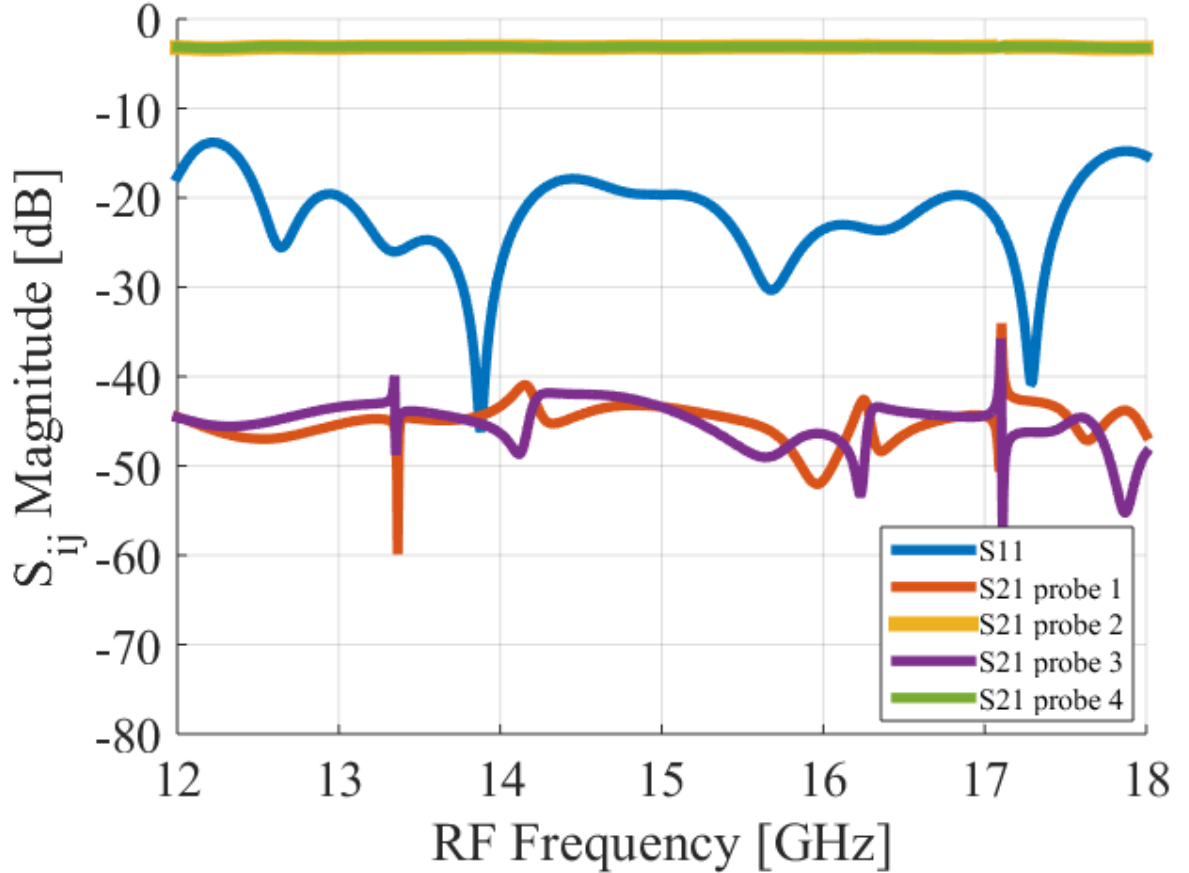


Figure 3.9. Simulation of all characteristics when the OMT with the rectangular to circular transition and the WR-62 to SMA transition are connected.

Once all the design requirements had been met, they were manufactured by José Pizarro in the laboratory using a CNC Milling Machine using the split block technique. Three prototypes were manufactured using two aluminum AL2017 blocks each.

The prototypes after construction are shown in Figure 3.10. The dimensions of the whole prototype system is in function of the WR-62 waveguide dimensions (0.622 Inches [15.7988 mm] x 0.311 Inches [7.8994 mm]).

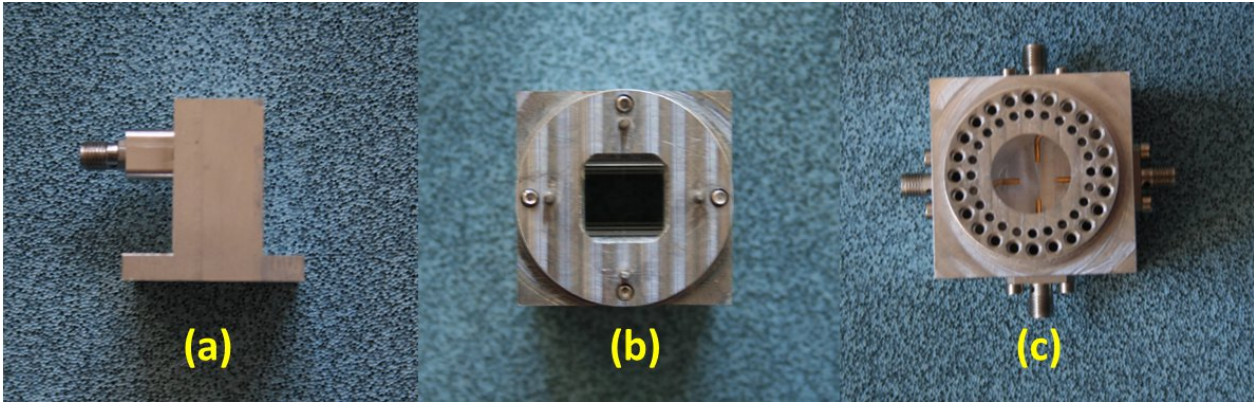


Figure 3.10. (a) SMA to WR-62 transition constructed to inject a test tone into the OMT. (b) Top view of the rectangular to circular waveguide transition. (c) Top view of the manufactured OMT.

3.2. Measurement procedure

The analog OMT was designed by R&D engineer David Monasterio and manufactured by mechanical technician Jose Pizarro in the Machine shop. Once the OMT was manufactured we proceeded to verify whether the energy transmits efficiently through the analog OMT, so a measurement using a Vector Network Analyzer (VNA) was required. In Table 3.1 the VNA characteristics are presented.

Table 3.1: Instrument used in this test-setup:

Equipment	Brand	Model	Characteristics
Vector Network Analyzer	Agilent	E8364C	10MHz - 50GHz

The first step consists of setting up the VNA using the wizard calibration specifying the band, the number of points and the S-parameters to be performed during measurements. In this stage the Agilent 85056D 2.4 mm standard calibration kit is used to calibrate the Agilent network analyzers up to 50 GHz for measurements of components with 2.4 mm connectors. The 85056D calibration kit includes the following items: opens, shorts and broadband terminators. The open and shorts are identical in the kit 85056D, however they are labeled with their respective names. The broadband loads are metrology-grade, 50 Ω terminations. Following the wizard calibration instructions is enough to VNA calibrate out at desired frequencies, extra documentation is not necessary for VNA calibration.

The measurement consists of a transmitting a sweep in 12-18 GHz using an Agilent 50-GHz VNA, as shown in figure 3.11. S11 and S21 are determined by measuring the magnitude and phase of the incident, reflected and transmitted voltage signals when the output is terminated in a perfect Z_O (a load that equals the characteristic impedance of the test system), in this every port was matched at 50 ohms. The VNA reads and saves the S-parameters. The results are presented in the next section.

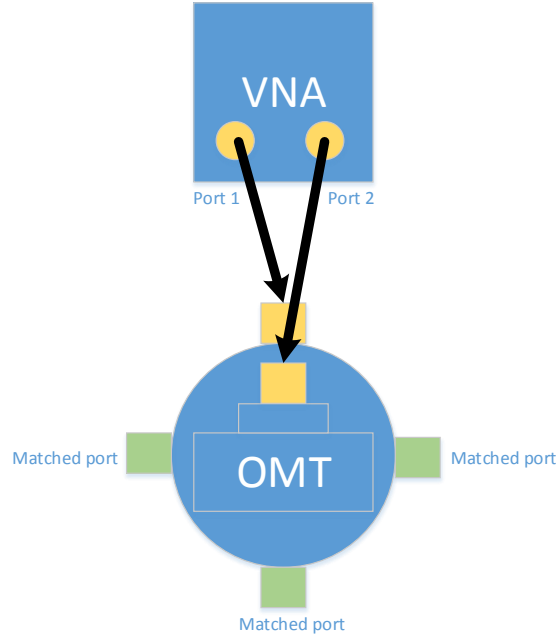


Figure 3.11. Sketch of the VNA setup to measure the S-parameters from 12 to 18 GHz. The VNA ports 1 and 2 are connected to the OMT as the scheme present. The remaining ports must be matched using 50 ohms loads to measure S_{11} and S_{21} .

3.3. Measurements results

The OMT with rectangular to circular waveguide transition and WR-62 to SMA waveguide transitions was measured using a VNA with 1 MHz discrete frequency sweep in the Ku-band, following the measurement procedure described above. The results of the transitions and reflections for both polarizations are shown in Figure 3.12.

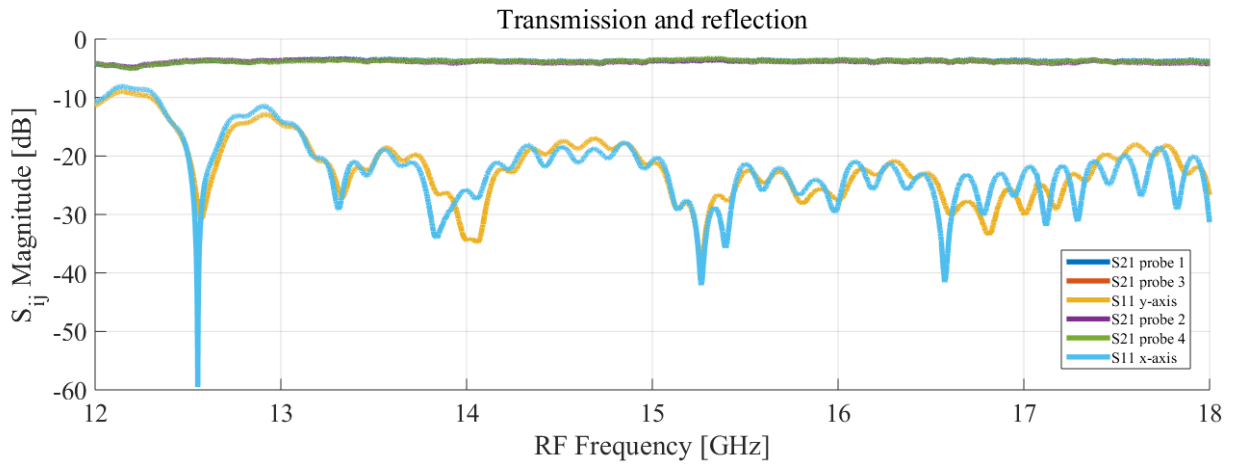


Figure 3.12. Circular waveguide to 4 coaxial probes OMT Transmission and reflection measurement using VNA.

The OMT has its reflection average below -20dB from 13.17 GHz to 18 GHz, which covers

80.5% of the Ku band. The OMT presents two sections in the band above -20dB, one from 12 GHz at -10.18dB and 12.5 GHz at -20 dB, followed by a resonant peak in 12.55 GHz which is not very wide. The second section above -20dB is from 12.64 GHz to 13.17 GHz followed by a resonant peak in 13.9 GHz in x-pol and 13.84 GHz for y-pol. The reflection average fits the simulation results, however, a ripple along the band is present due to standing waves that contribute only to gain ripple, not cross-polar leakage, therefore this behavior is acceptable because the system met the project requirements.

On the other hand, the average of the transmission results of the transitions for both polarizations along the Ku-band are in a range about -3 to -4 dB while the simulation result for transmission is at -3dB. The loss in the range of -1dB is due to the cables and adapters that were not calibrated during the VNA set up.

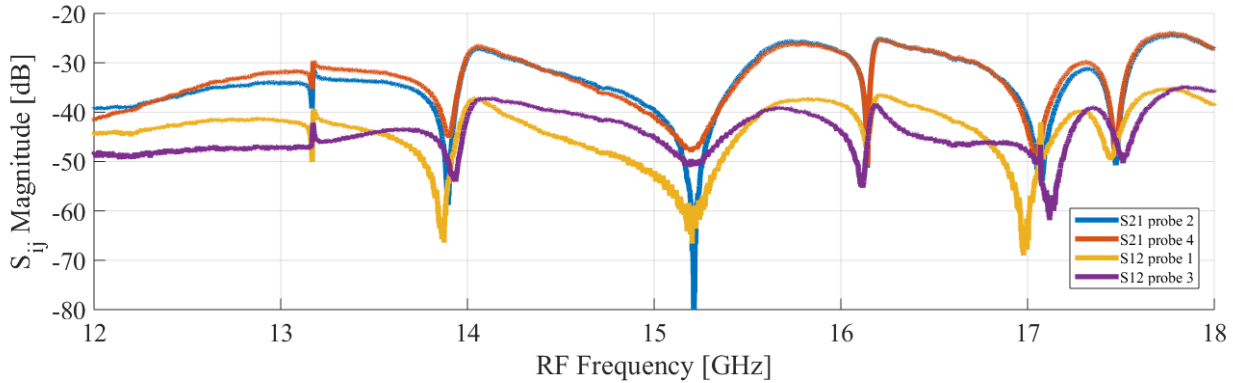


Figure 3.13. Circular waveguide to 4 coaxial probes OMT and cross-polarization measurement using VNA.

In Figure 3.13 the cross polarization of the OMT is presented. The cross polarization is around -40dB on average, but degrades around 14 and 17 GHz due to three resonant peaks that were present in the transmission and reflections are also present in the cross polarization.

3.4. DSB Heterodyne Front End receiver

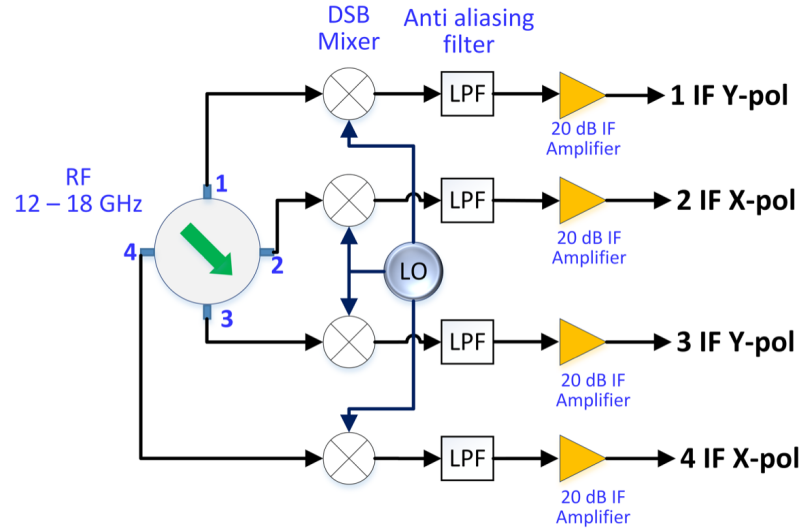
This section presents the design analog front end components. In the following subsections, the front end components will be described and their performance and characterization will be presented.

One of the main attractions of digitally calibrated analog receivers is that we can use simple analog components than can be produced, miniaturized and integrated easily, but reaching similar or even better performance than complex fine-tuned designs. Particularly we want to demonstrate that a very simple OMT made of four coaxial probes inserted in a circular waveguide can reach similar or better performance than the more complex and bulky Dual-Ridge [7] or Turnstile [9] OMTs commonly used in Radio Astronomy receivers. This could allow the construction of high-performance dual polarization receiver arrays, which are normally single polarization due to the difficulty of miniaturizing and integrating a large number of OMTs.

Some components of the digital OMT were built in the laboratory, that includes the circular

waveguide and the transitions that are used to make a connection to the SMA cables, its performance obtained during the simulation stage using HFSS and its characterization using VNA once they were manufactured are presented.

Figure 3.14 shows the block diagram of the front-end receiver implemented for the digital OMT. The front-end has been assembled using commercial parts working at a frequency range of 12 – 18 GHz (Ku-band). After the OMT the signal is led through four identical signal paths where the RF signal is down-converted to baseband using a mixer (part number: ZX05-24MH+) with the local oscillator (LO) tuned to select the specific bands along side the RF band. After the down-conversion the IF bandwidth is filtered (part number: VLF-800+) to remove harmonics and amplified (part number: ZX60-43+).



Digital Orthomode Transducer Test-Setup.

Figure 3.14. Block diagram of the Digital ortho-mode transducer front-end setup.

The Ku-band was chosen to show that the OMT design and polarization synthesis works at higher frequencies while still being able to construct the full setup using commercial parts. Figure 3.15 shows a picture of the front-end test-setup of the digital OMT.

The parameters of the Front-End devices are presented in the following tables:

Table 3.2: Mixer ZX05-24-MH+:

Freq RF [GHz]	Freq LO [GHz]	Freq IF [GHz]	Max Pow IN [dBm]	Conversion Loss (typ.) [dB]
7.5 - 20	7.5 - 20	DC - 7.5	17	7

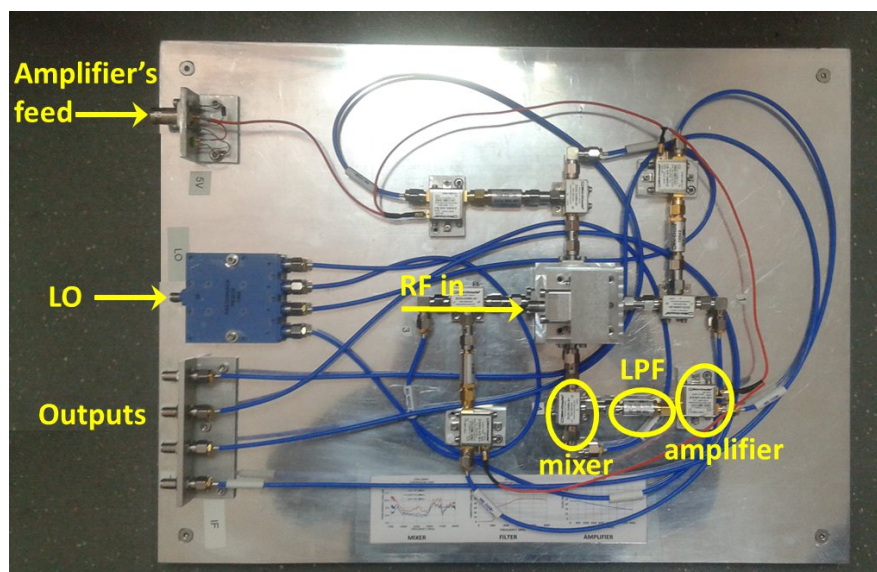


Figure 3.15. DOMT Front-End.

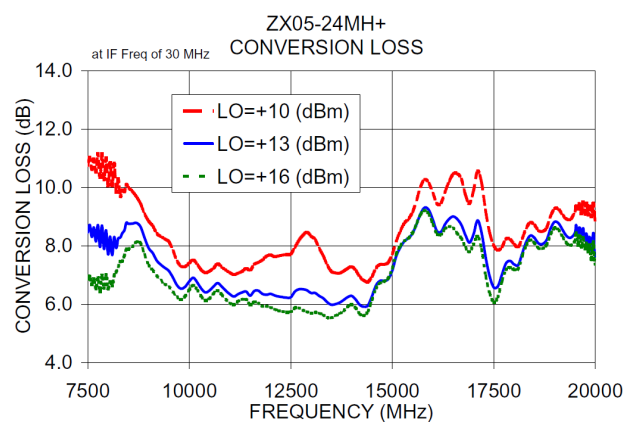


Figure 3.16. Coaxial Frequency mixer, wide band from 7500 to 20000 MHz.

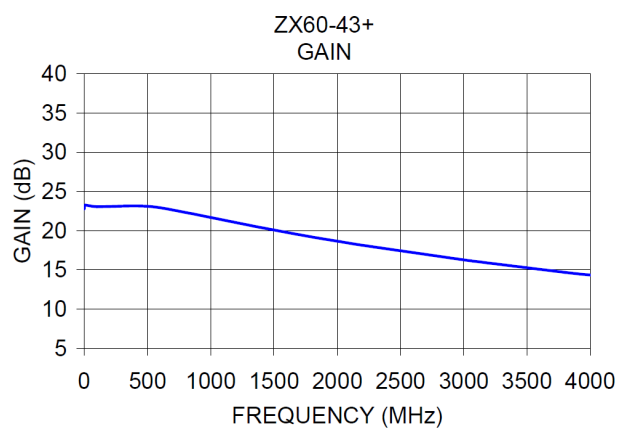


Figure 3.17. Wide band amplifier

Table 3.3: Amplifier ZX-60-43+:

Freq IN [MHz]	Gain [dB]	Max Pow OUT (1dB Comp.) [dBm]	Vin [V]
0.5 - 4000	23.1	17.3	5

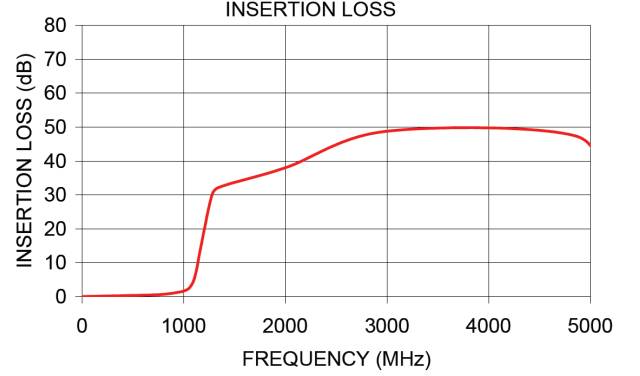


Figure 3.18. Wide band Low pass filter

Table 3.4: Low Pass Filter VHF-5050+:

Passband (Loss < 1dB) [MHz]	f_{co} (Loss < 3dB) [MHz]	Stopband (attenuation > 20dB) [MHz]	VSWR typ. :1	
			Stopband	Passband
DC - 800	1075	1250 - 5100	20	1.2

3.5. Digital Back-End

In order to process the four IF outputs to synthesize the desired polarization vectors, we need to implement 4 high resolution wideband spectrometers.

MATLAB-Simulink is used to program the FPGA chip at low level using a graphical language that describes the interconnections of logical gates or functional modules. Most of the modules used in this top-level schematic are already developed by our group or available in CASPER libraries. Figure 2 shows the firmware to be implemented in the FPGA to perform the tasks depicted within the yellow dash-line region in Figure 1 and described above. In the following sections, the Back-End will be presented, focusing on its characteristics and its performance.

In this work, we present a novel class of OMT which use digital calibration to synthesize the desired polarization vectors to achieve very low cross-polarization. Inspired by the work of Morgan et al.[5] we decided to focus our efforts on implementing the proof of concept developed by NRAO using off-line processing of narrow bandwidths, but using on a real-time Virtex-6 FPGA (XC6VSX475T-1FFG1759C) [27] processing platform, wide instantaneous bandwidth, and non-stop integration capabilities.

To implement the DOMT we are using a ROACH-II [16] (Fig. 3.19) platform equipped with two 5 Gs/s (max) analog-to-digital converter (ADC). Each ADC uses an e2v EV8AQ160 chip [42] with 4 cores at 8-bit resolution. Each ADC board allows to sample up to two signals in

parallel, the ROACH-II platform can be configured for 4 inputs.

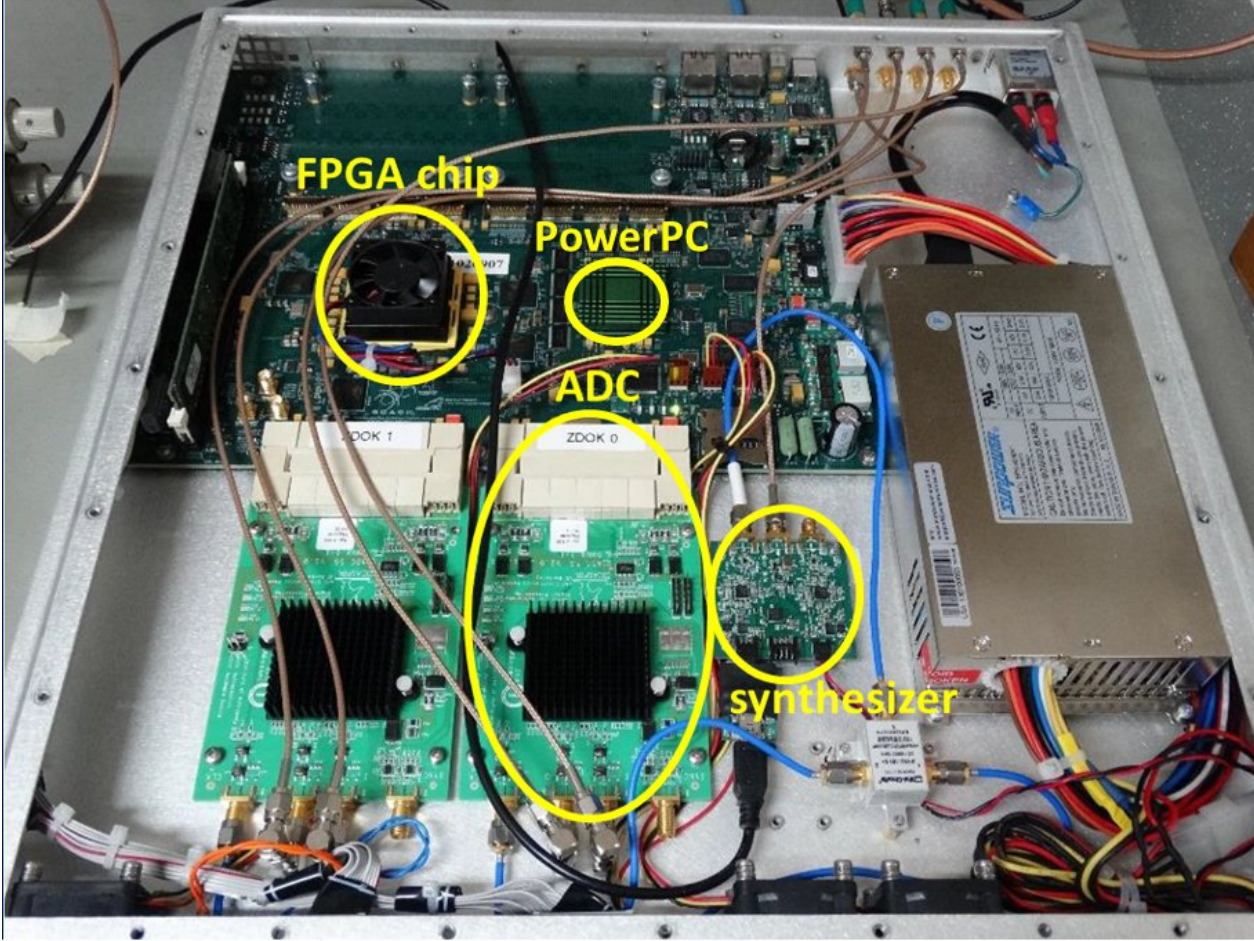


Figure 3.19. ROACH-II. Two ADCs 5 GSps are connected to ZDOK connectors. The synthesizer module (valon 5007 [43]) provides the clock reference to the ADC boards [44].

The analog part of the DOMT consists of a circular waveguide to four probes coaxial transition. Each output is connected to an independent receiver chain constituting its Front-End. Figure 3.1 shows a block diagram of the OMT with 4 outputs.

The FPGA configuration is specified using a hardware description language (HDL) with the help of Matlab-Simulink as a visual user interface. FPGAs contain an array of programmable logic resources and a layer of reconfigurable interconnections that allow these resources to be connected, permitting the implementation of custom hardware. Logic blocks can be configured to perform complex logic functions, or used as look-up tables. In most FPGAs logic blocks also include memory elements, which may be simple flip-flops or complete Random Access Memories (RAMs). In Xilinx nomenclature, they are called “Block RAMs” (BRAMs). In addition to the above, the Virtex-6 FPGA have several thousand arithmetic units (ALUs) available on a single chip most of them are DSP48 slices. The DSP48 is a digital signal processing logic element, with both an exceptional capacity of performing all kinds of arithmetic operations and efficient calculation working in parallel [28].

3.5.1. ROACH-II

In Figure 3.19 the hardware used to perform the signal processing known as ROACH-II (ROACH stands for Reconfigurable Open Architecture Computing Hardware) is presented. The centerpiece of the ROACH-II board is a Xilinx Virtex-6 SX475T FPGA. This FPGA has 476160 logic cells, 74400 slices² and 2016 of DSP units on a single chip.

In Figure 3.20 the Roach-II Revision 2 block diagram is presented. A separate PowerPC 440EPx runs Linux and it is used to control the board, which means reconfiguring the FPGA and allowing interfacing between the FPGA software registers/BRAMs/FIFOs and external devices using Ethernet. Two ADCs are connected to the board through ZDOK connectors [45] allowing interface cards to be attached to the FPGA. Both ADCs have 8-bit resolution and sampling rates up to 5GSPS. An inexpensive synthesizer board, known as Valon 5007³ [43] provides clock reference to the ADC boards.

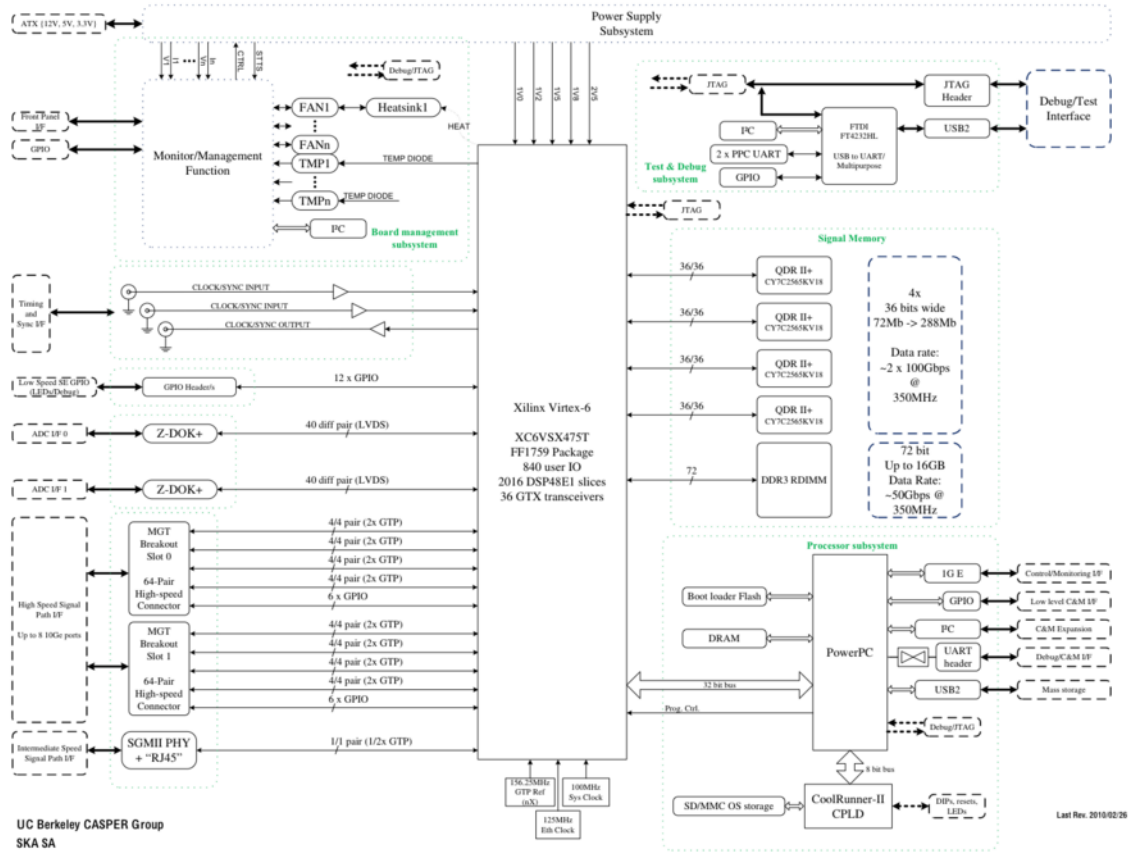


Figure 3.20. ROACH-II revision 2 block diagram⁴.

²Each Virtex-6 FPGA slice contains four LUTs and eight flip-flops, only some slices can use their LUTs as distributed RAM or SRLs [27].

³Valon Technology <http://www.valontechnology.com/5007/5007.htm>

⁴Figure extracted from https://casper.berkeley.edu/wiki/ROACH-2_Revision_2.

3.5.2. External Clock reference synthesizer

Figure 3.20 shows the external clock reference synthesizer device which is placed into the ROACH-II box, this is the Valon 5007 Dual Synthesizer [43] and provides high quality clock signal to the ADCs and allows to reference the sampling process. The frequency can be set between 137.5 and 4000 MHz. This synthesizer has a non-volatile FLASH memory that allows the user to set frequencies by tuning the internal VCO, i.e. keeps the choices made after turning off the module.

3.5.3. The ADC Board ADC1x5000-8

In Figure 3.20 two ADC boards developed by ASIAA (Academia Sinica Institute for Astronomy and Astrophysics) are connected to the ROACH-II, they are known as ADC1x5000-8. The centerpiece of the board is the ADC chip e2v EV8AQ160 [46], with 8-bit resolution and 4 interleaved cores, it can operate in three different modes. However, the ADC1x5000-8 with 8-bit resolution operate in two modes:

1. one-channel mode up to 5 GSPS.
2. two-channel mode up to 2.5 GSPS.

The ADC boards have two independent SMA connectors intended as inputs of IF signals. When we program the FPGA to operate these ADCs in two-channel mode, two connectors fed by two IF signals can be sampled up to 2.5 GSPS sampling rate. While if we program the FPGA to operate these ADCs in one-channel mode, one SMA input supplied by an IF signal can be sampled up to 5 GSPS.

In Figure 3.19 is shown the ROACH-II with 2 ADCs connected to the ZDOK connectors. The ADC boards have three SMA cables connected. The ROACH-II's FPGA was programmed to operate in the two-channel mode to process the polarization components from the analog Front-End. From left to right, the blue cable carries the external clock reference for each ADC. Then the middle and right SMA cables carry the IF signals coming from the analog front end to feed the ADCs. Each ADC gets a new sample on every positive and negative edge, using the external clock reference as the master clock.

In Figure 3.21 the internal ADC chip block diagram is presented. Each core represents an ADC with 8-bit resolution and a 1.25GSPS sampling rate, this allows 256 levels in amplitude of the sampled signal and in one channel mode when all cores are interleaved in order to sample only one input signal up to 5GSPS. This property makes necessary the calibration of the ADC cores prior to use due to issues during the interleave mode in gain, offset and phase [25].

The ADC has an SPI bus (Serial Peripheral Interface), through which it is possible to write in the internal registers, which are used to set gain corrections, offset, and phase. The gain has a control range of $\pm 18\%$, the offset of $\pm 50\text{mV}$ and the phase of $\pm 14\text{ps}$.

ADC four cores use the same external clock signal, which may be of a maximum frequency of 2.5 GHz. The clock is divided by 8 before entering the FPGA in two-channel mode. While when the ADC is in one-channel mode 16 parallel samples (8-bit each) are generated.

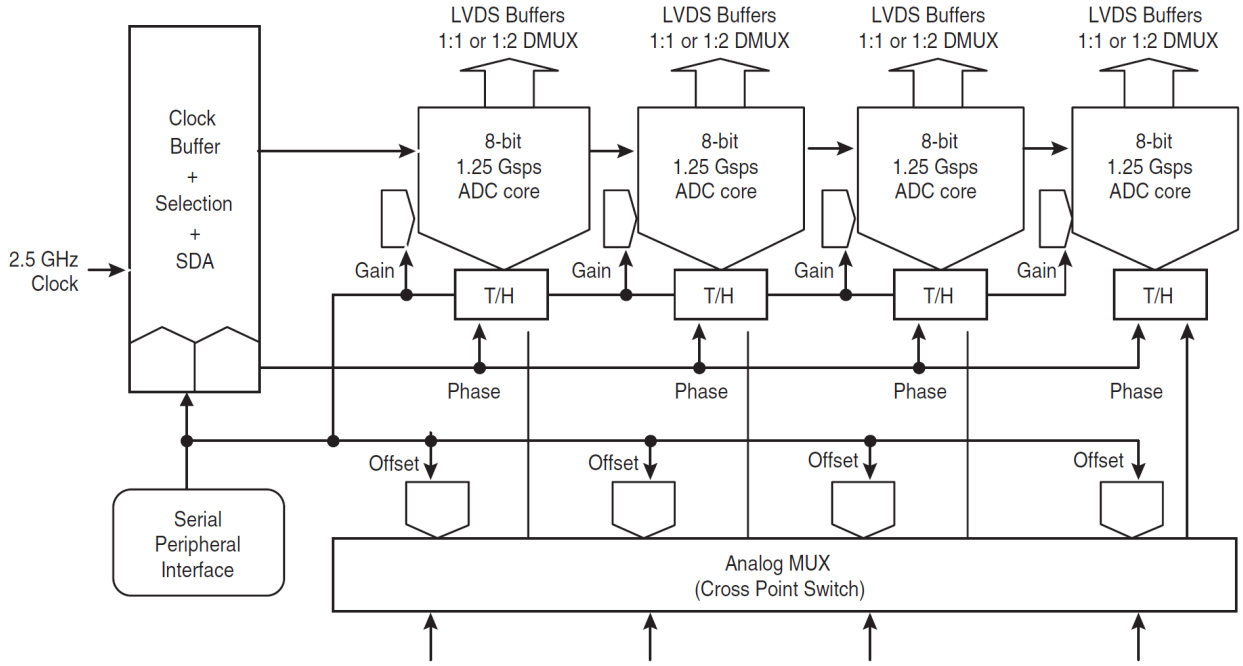


Figure 3.21. EV8AQ160 chip ADC 5 GSps block diagram [46].

ADC phase difference compensation

As already mentioned above, the FPGA can be programmed to operate with two ADC boards working in two channel-mode to digitized signals. However, the digitized signals have phase differences caused by the two ADC boards are not able to be synchronized automatically. Sync out the two ADC boards perfectly is tricky because every time you reprogram the FPGA, a mismatch latency value between the ADCs appear randomly. Fortunately, this value can be measured on-the-fly in terms of the master clock period.

A handy way to synchronize two ADC boards is by incorporating FIFOs in the first stage of gateway on the FPGA as shown in the following Figure 3.23. The adopted solution consists in using a delay FIFO (First Input First Output) block after the ADC blocks. The delay FIFO block allows delaying the flow of data in a specific amount, multiple of the FPGA clock period, by changing the value of a register via a python script. The disadvantage of this implementation is that the user must change the delay every time the FPGA is reconfigured. The advantages are that it is fast and easy to automate via a python script.

Figure 3.22 shows the results of phase differences, with the implemented solution. This time all phase differences are fairly near to zero, which is what was expected, hence solving the ADC synchronization problem.

An alternative to resolve the issue can be implementing a hdl module which operate theses both ADC boards in interleave mode, i.e. gathering samples in an interleaved manner will improve phase errors detected, allowing automation of the calibration phase and secondly increasing the IF bandwidth. The ideal case would be to reach 1.25GHz by IF, which is the maximum sampling rate for the ADC5G in two-channel mode⁵.

⁵In two-channel mode, the in-phase 1.25 GHz clock is sent to ADC A or C and the inverted 1.25 GHz clock is sent to ADC B or D, while the analog input is sent to both ADCs, resulting in an interleaved mode with an equivalent sampling frequency of 2.5 GSps. EV8AQ160 QUAD ADC Datasheet, page 2,

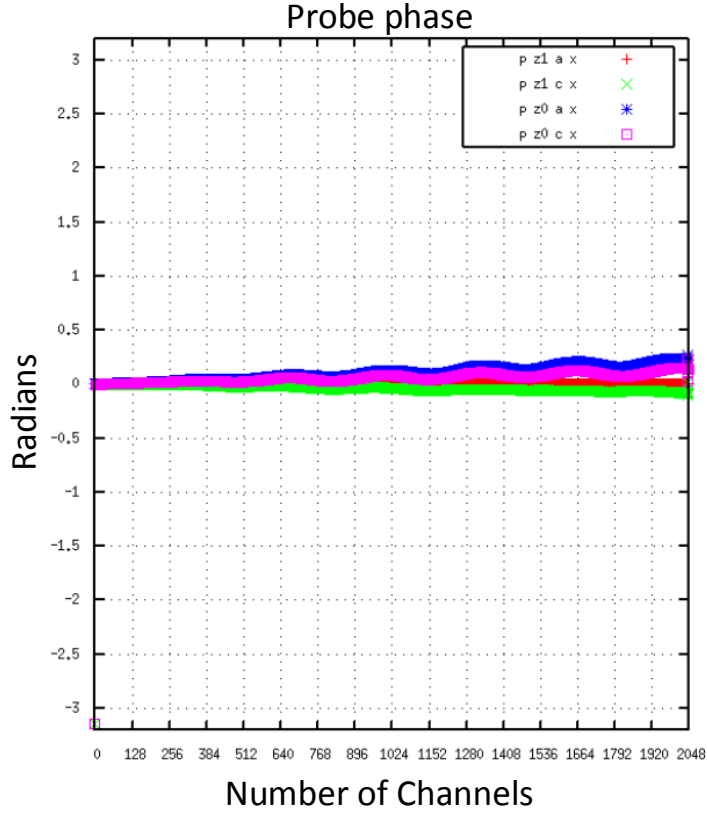


Figure 3.22. Snapshot obtained with a python script during phase difference compensation. This result was obtained after ADC calibration and FIFO delay compensation.

3.6. FPGA Gateway design

The DOMT was developed by two subsystems, hereafter named: 'calibration' and 'polarization synthesis.' A ROACH-II (see Figure 3.19) was used to implement both subsystems. The ROACH-II is equipped with the new Xilinx Virtex-6 series of FPGAs and two wideband ADC boards. Each ADC allows the sampling of two signals in parallel, so in total the DOMT has 4 signals as input. The calibration stage captures the frequency spectra and calculates the gain matrices whereas the synthesis stage synthesizes the polarization vector using the calibration data. All the models have been designed using CASPER library IP blocks. The DOMT back end was designed to meet the following requirements for a successful integration with the analog front end:

1. The solution was implemented in a ROACH-II Revision-2 platform, using two ADC boards *ADC1x5000-8* from ASIAA (Academia Sinica Institute for Astronomy and Astrophysics) connected to the ROACH-II.
2. Process 4 IFs bandwidth in real-time using the analog front end proposed in the whole Ku-band.
3. Implement the Calibration and Spectrometer mode in one gateway design.

4. Spectrometers:

- a) Dynamic Range = around 45dB on average.
- b) Bw = 600MHz, i.e. a sampling rate of 1.2GSPS for each ADC.
- c) Number of channels = 2048.
- d) Spectral resolution = 293kHz.
- e) 512 channels indexed into 1 Bram for X-Pol and Y-Pol.
- f) 64bit per channel.
- g) Provide on-the-fly programmable registers to set the spectrometers gain and accumulation length.

3.6.1. Calibration:

In Figure 3.23 is shown the calibration model. The calibration model has the task of calculating the correct parameters for the OMT presented in Figure 3.4. The architecture is similar to the spectrometers, but instead of computing the power of the spectrum, the real and imaginary components are saved in the Block RAM. (BRAM). Later all the data of the spectrum is processed by Python scripts. The general structure of the calibration model is shown in Figure 3.23. This subsystem uses 2 ADC boards (4 inputs), each one will output 16 data lines of 8 bits each. The sampling rate of the ADC boards are set to 1200 MSPS, dual-channel mode and the internal FPGA clock are set to $1/8ADC_{clock} = 150$ MHz. This results in a bandwidth of 600 MHz. Experiments with increased clock speeds led to problems in meeting the timing constraints in the FPGA. Each collection of 8 data lines is then fed into a polyphaser filter bank (PFB) and a Fast Fourier Transform (FFT). Together these blocks achieve real-time non-stop Fourier transformation when input data is continuously fed into the system. The size of the PFB and the FFT are 4096 points and have an output coefficient bit width of 18 bits. Only the positive frequencies of the FFT outputs are used since the negative frequencies are mirror images. This results in a spectrum per FFT, each consisting of 512 samples. The FFT block procedures four data lines since it is delivering four data samples at each clock cycle.

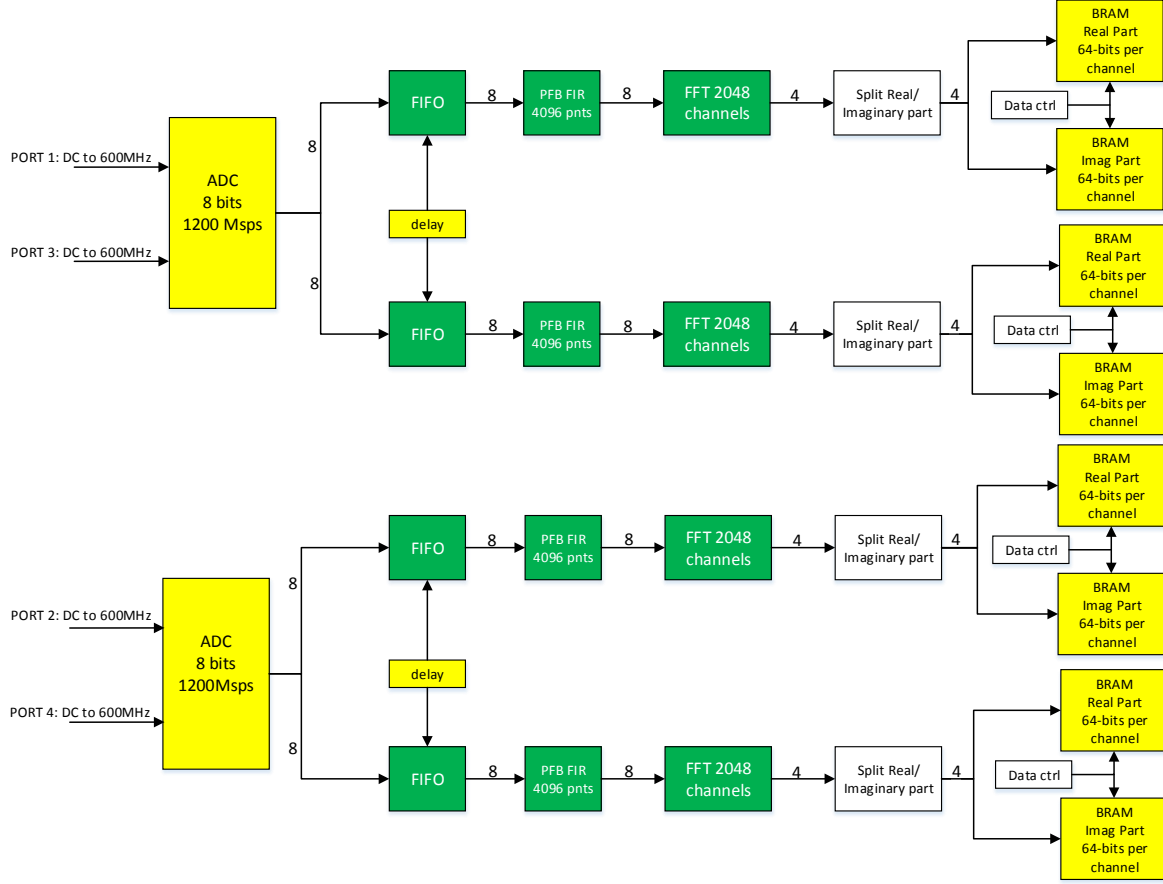


Figure 3.23. Digital OMT calibration schematic.

3.6.2. Polarization synthesis

After the calibration procedure has been completed and all the coefficients are known the results are loaded in the model which synthesizes the polarization vectors (see Figure 3.1). The ADC board outputs are again fed into a 4096 points FTT. Each line, that outputs 2048 FFT channel frequencies, is split into its real and imaginary parts and then multiplied with the calibration coefficients. Afterwards the results are summed to constitute the final polarization in either the x or y direction according to the equation 3.1.

$$\begin{bmatrix} s_x[n] \\ s_y[n] \end{bmatrix} = \begin{bmatrix} H_{11}[n] & H_{12}[n] & H_{13}[n] & H_{14}[n] \\ H_{21}[n] & H_{22}[n] & H_{23}[n] & H_{24}[n] \end{bmatrix} \begin{bmatrix} V_{11}[n] \\ V_{21}[n] \\ V_{31}[n] \\ V_{41}[n] \end{bmatrix} \quad (3.1)$$

The latest version of our Polarization Synthesis model for the DOMT, with its Front-End and with the ROACH-II connected as a Digital Back-End is illustrated in Figure 3.1.

3.7. Digital Orthomode Transducer Gateway

MATLAB-Simulink[®] is used to design the Gateway⁶. The modules used in this top-level schematic were developed using the Xilinx and CASPER libraries. Then this gateway was compiled using the CASPER Toolflow. Figure 3.24 shown a block diagram of the firmware implemented in the FPGA. As an alternative to the ADC synchronization issue the calibration and synthesis model were connected in the top hierarchy of the system as it is shown in Figure 3.24.

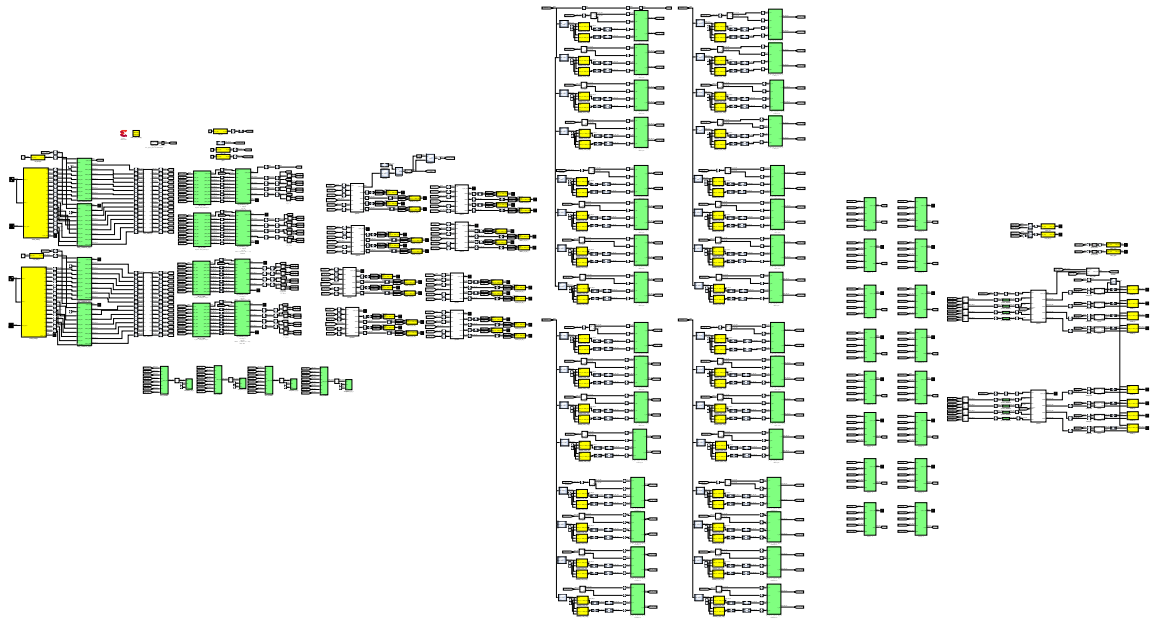


Figure 3.24. Top level Simulink block diagram of the Digital Orthomode Transducer (available in Appendix B).

⁶Gateway is the representation of the data processing algorithm that runs on the FPGA. Programming an FPGA implies building hardware through selecting a particular interconnection of the hardware resources (e.g. logic gates, Digital Signal Processor (DSP) slices or memories) [22].

3.7.1. Calibration Gateway

In Figure 3.24 the DOMT gateway was presented. Now we are going to present the sub-process that constitutes the calibration model in DOMT.

In Figure 3.25 the snapshot shows blocks used during the Calibration stage. The snapshot block is a configurable block for capturing blocks of data. First the data is concatenated and is then stored in RAM memories. These blocks were included in order to calibrate the ADC before the start up of the DOMT.

In Figure 3.26 which represents the left side of Figure 3.24 the ADC calibration is presented. From left to right: ADC, FIFO. This includes the FIFO memories in order to correct the ADC synchronization issue. In Figure 3.27 the PFB is presented. The PFB spectrometer is composed of a 4-tap Fir filter and a 4096-point FFT. The PFB is capable of non-stop processing with 8 parallel inputs and finally 4 outputs per clock, each complex channel output is split in two values second complement signed 17.16 by the block real/imaginary Split.

In Figure 3.28 we present the subsystem formed mainly of BRAMs that store up to 512 FFT channels. The 8 white blocks are used to quantize the FFT outputs. Then the outputs are stored in BRAM modules until a counter reaches 512 account when a reset signal is raised restarting the write from 0 to 511 in the BRAM. In the top-left corner you see some additional logic which is the 'data ctrl' that has two registers which are write in order to enable and disable writing in BRAMs via Ethernet using a python script.

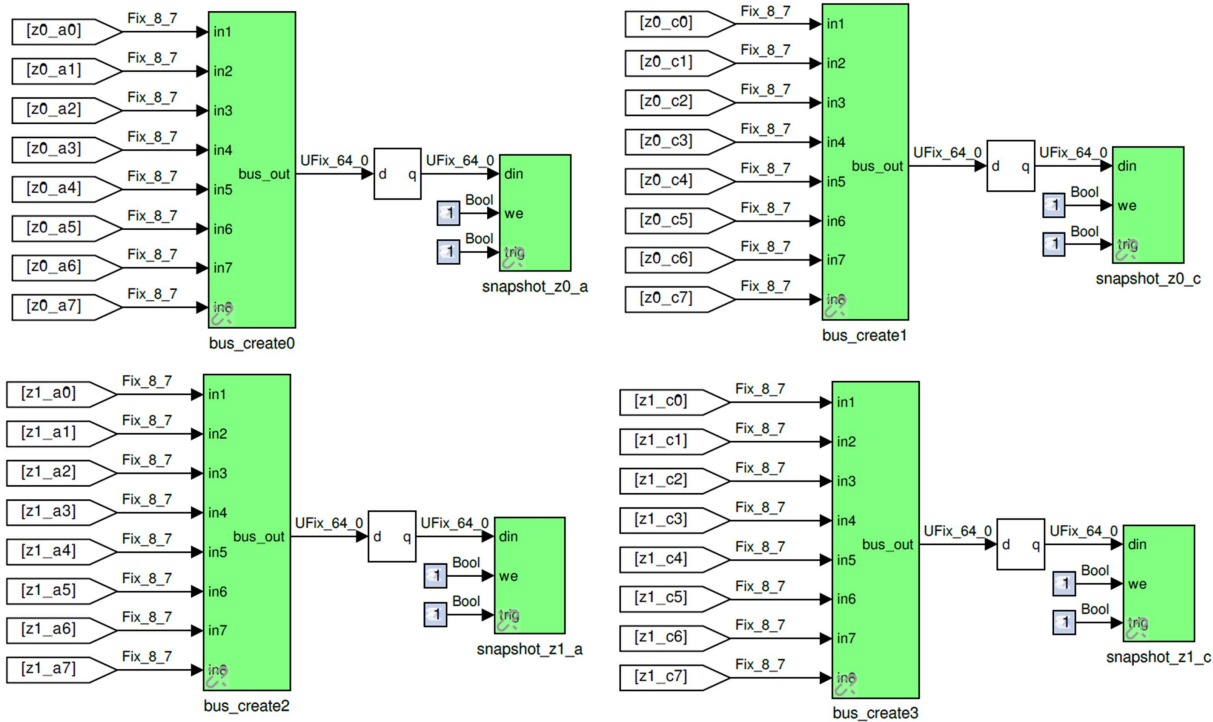


Figure 3.25. Snapshot circuit to record blocks of data obtained by the ADCs. First the data is concatenated and then is stored in RAM memories, implemented in a BRAM. The Bram has a memory depth of 16384 and 32 bit per data. These blocks were included in order to calibrate the ADC before the start up of the DOMT.

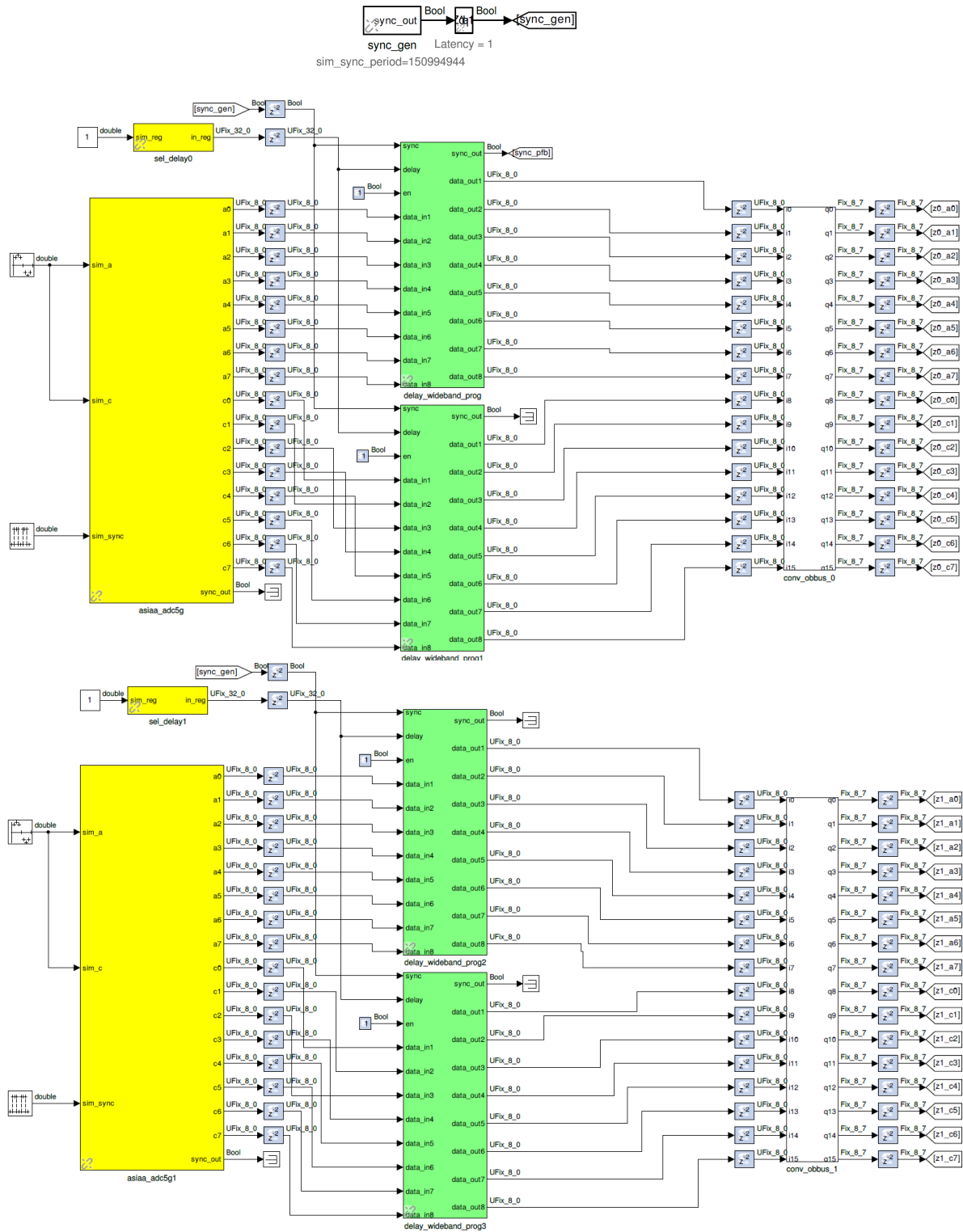


Figure 3.26. Left side of the calibration gateway, left to right: ADC, FIFO.

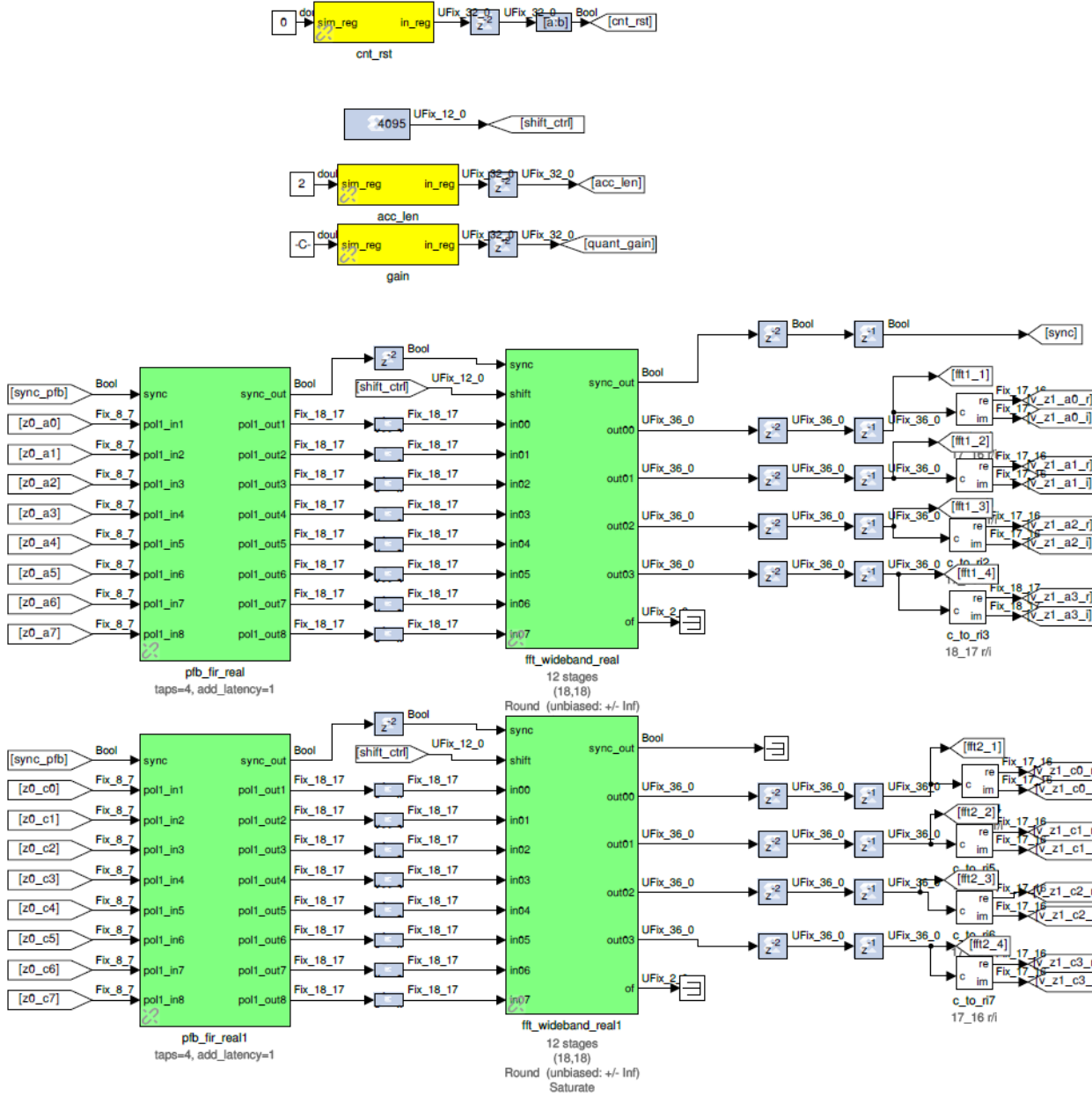


Figure 3.27. The real PFB spectrometer is composed of a 4-tap Fir filter and a 4096-point FFT. This real Polyphase Filter Bank uses windows of 512 data to improve the shape of channels within a spectrum by applying the hamming window. Only positive frequencies are output (negative frequencies are the mirror images of their positive counterparts), so there are 8 parallel input and 4 output ports per PFB.

3.7.2. Synthesis Gateware

In the following pictures we present the synthesis model implemented in Simulink, following the Block Diagram presented in the Figure 3.24. In Figure 3.29 the middle part of the synthesis model, part 2, is presented. In these blocks are the calibration coefficients stored and multiplied with the FFT input. Note that for each H matrix entry you have 2 BRAM modules, one for the real and one for the imaginary part.

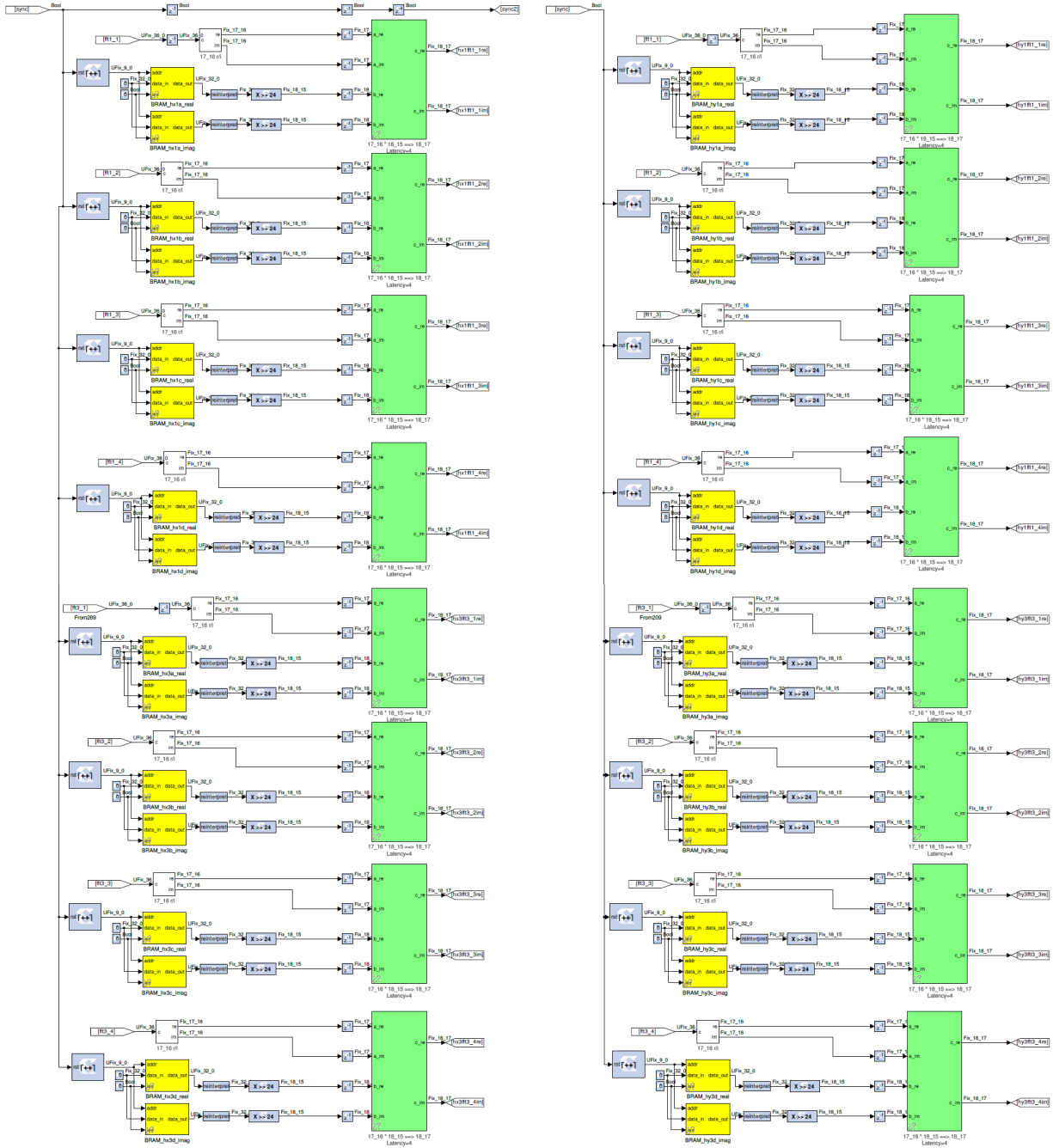


Figure 3.29. The middle side of the polarization synthesis model. The H matrix has been hardcoded to be able to load the calibration coefficients via python. This circuit multiplies every FFT's channel by a calibration coefficient to compensate the amplitude and phase imbalances that the orthogonal ports present, regarding co-polar signal of the OMT.

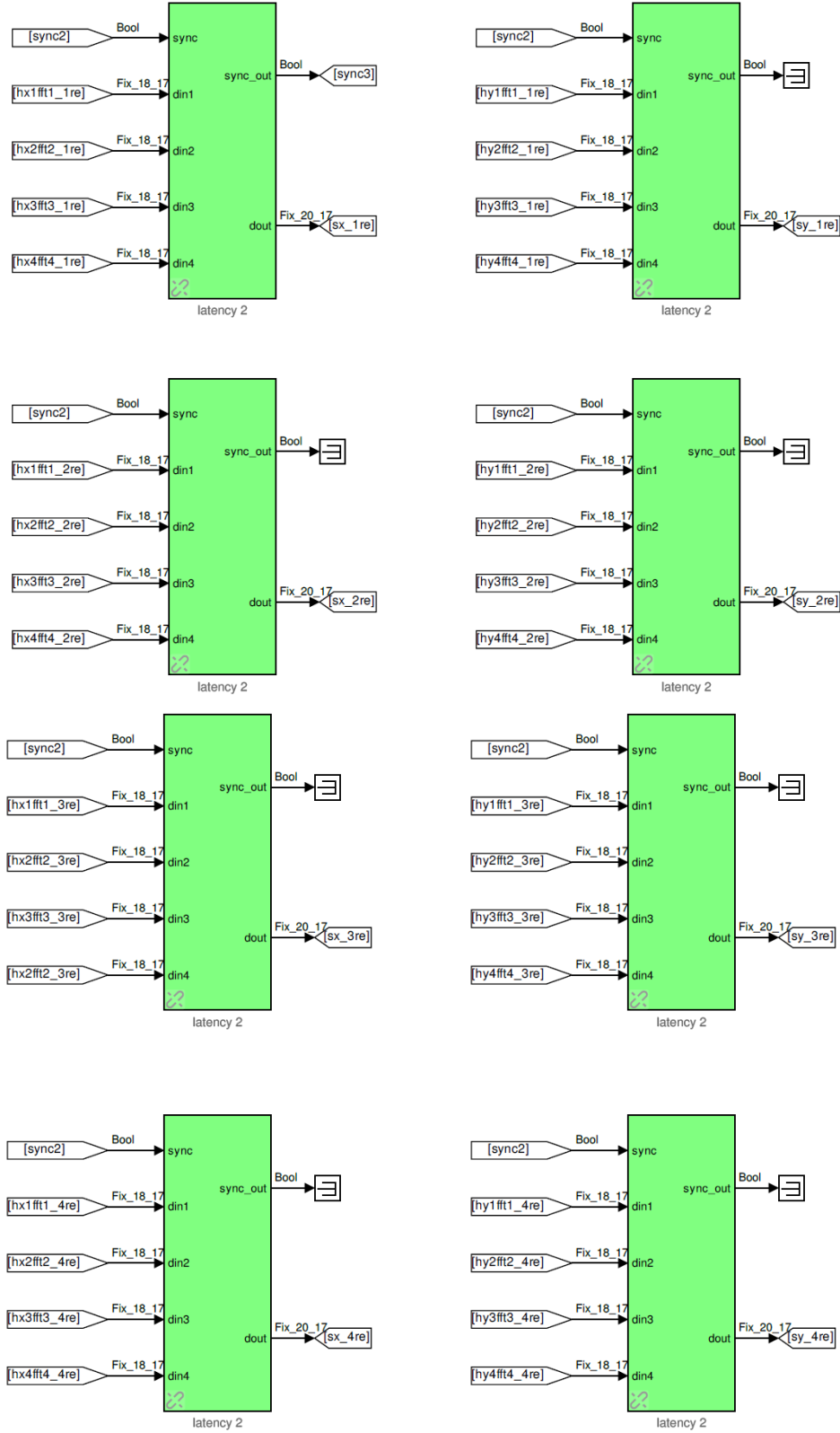


Figure 3.30. The middle side of the polarization synthesis model, part 2. The addition step of the multiplication algorithm of matrices V (each channel of the FFT) by H (calibrated coefficients) was hardcoded to obtain the S' matrix elements. The S' matrix is the polarization vector in the x and y direction.

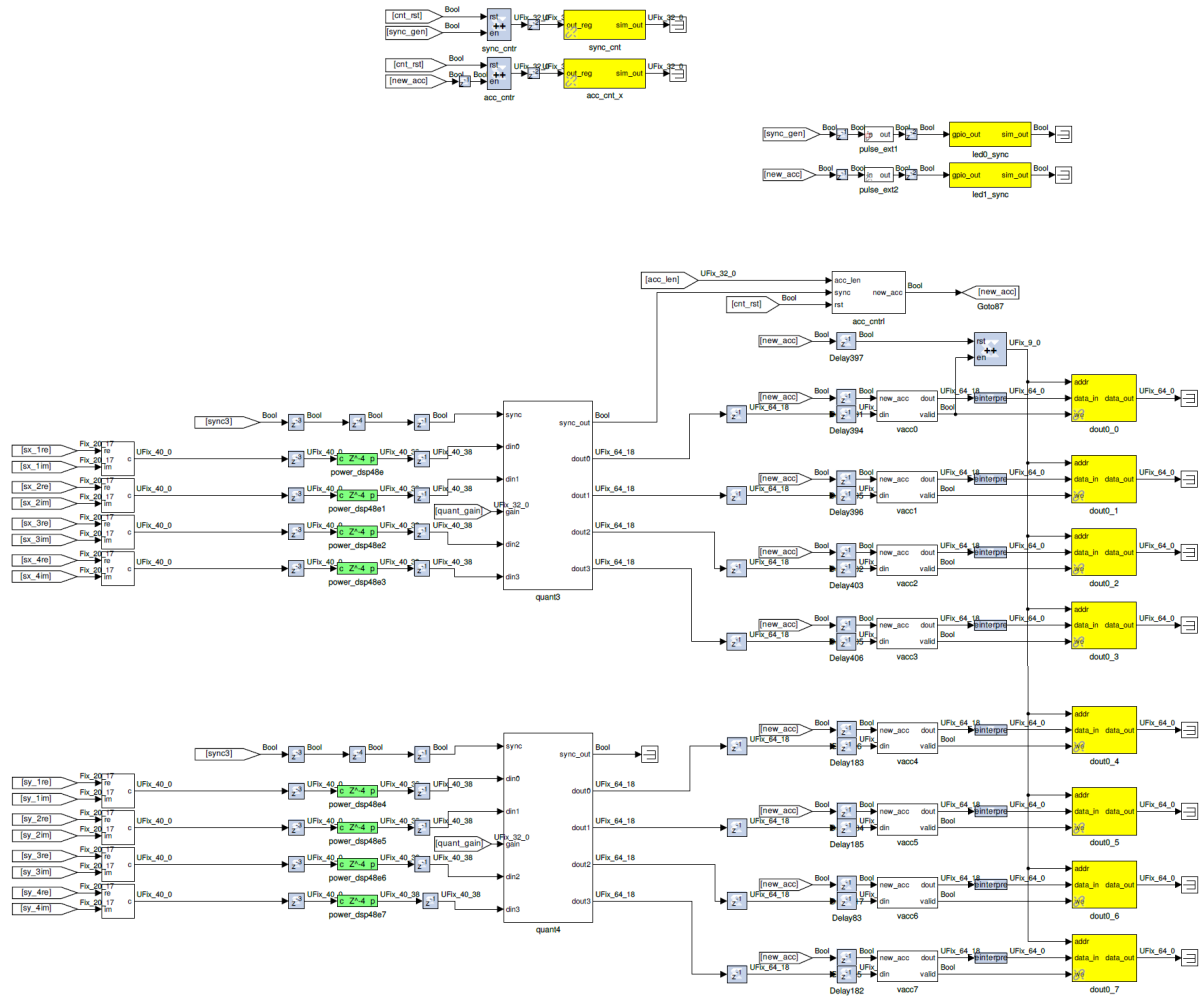


Figure 3.31. The right side of the polarization synthesis model consists in the vector accumulators. The real and imaginary components of the S' matrix are plugged into power blocks, to convert from complex values to real power values by squaring. They are also scaled by a gain factor before being quantized to unsigned 64-bit. The requantized signals then enter the vector accumulators. Accumulation length is controlled by the “acc_ctr1” block. The accumulated signal is then fed into software registers, which allows the writing and reading of blocks of data via python.

Chapter 4

Results and Measurements

This chapter presents outcomes obtained with the DOMT prototype. The calibration coefficients obtained for three incidence angles are presented $\alpha = 0^\circ, 90^\circ, 45^\circ$. The amplitude and phase imbalances of the cross-polarization measurements of the OMT analog stem from the non-linearity of the mixing process which by digital calibration is compensated achieving high isolation. Finally, the cross-polarization isolation achieved by polarization synthesis means of an un-calibrated DOMT and calibrated DOMT are presented.

4.1. Test-Setup

In Table 4.1 the equipment models and characteristics used in test-setup are presented. In Figure 4.1 the DOMT schematic is presented. It is correspondent to the block diagram presented in Figure 3.1.

Table 4.1: Instruments used in this experiment:

Equipment	Brand	Model	Characteristics
Signal Generator	Anritsu	MG3604C	2-40 GHz
Signal Generator	Agilent	E8257D	250KHz-20 GHz
DC POWER SUPPLY	MCP	M10-DP-305E	0-30Vx2 0-5Ax2

Figure 4.2 shows the measuring test setup bench used in the experiment. Two signal synthesizers were used as LO and RF sources. No particular care was taken to match cable length or to choose matched-pairs of mixers, amplifiers or any other component. The RF synthesizer provides the clock reference at 10 MHz to the LO synthesizer and to the four ADCs in ROACH-2 keeping the coherence during the experiment.

In Figure 4.2 top side a computer connected to the laboratory LAN is shown. It's used to control the instrument and download the spectra. A Python script using telnet protocol can read and write registers and memories in FPGA and set power and frequencies and read

values from Signal Generator Agilent E8257D (RF Source), as well as the Signal Generator Anritzu E8257D used as LO can be set to measurement.

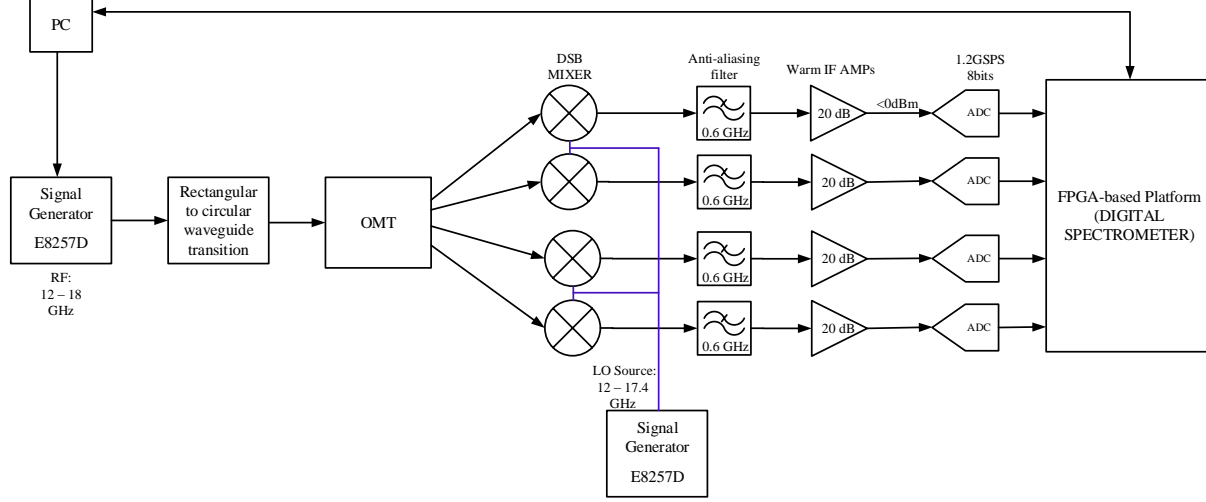


Figure 4.1. Sketch of the calibration setup to obtain calibration coefficients. The IF amplifiers are used in order to get the -4 dBm at the input of the ADC, this is the point where the ADC has the best performance.

4.2. Digital OMT validation

The analog OMT prototype (described in section 3.1.1) was degraded, as shown in Appendix C, to include all common manufacturing issues pinned by mechanical accuracy. To demonstrate manufacturing tolerance immunity is one of the chief benefits of a calibrated approach, a test case, which consists of an OMT degraded with a transmitted polarization for the orthogonal probes on the order of -35 dB in the whole Ku-Band (Fig. C.6), was chosen for this experiment.

Simultaneous measurements of copolarized and cross-polarized signal components for two orthogonal linear polarizations are presented in the following sections, to measure the cross-polarization isolation of the system.

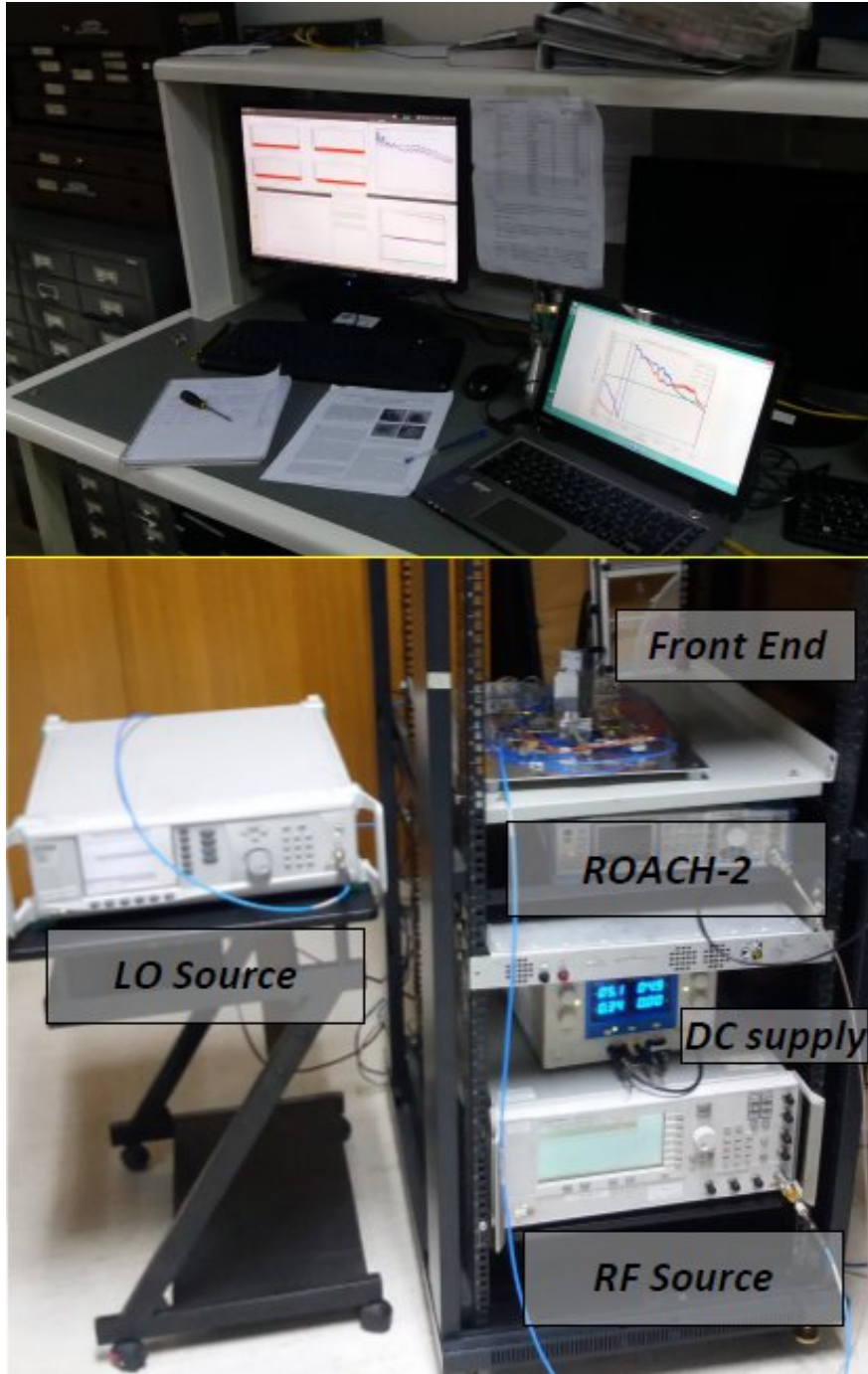


Figure 4.2. Measuring test setup implemented for the DOMT characterization. Top-down the PC connected to LAN can be seen. At the center the front end plate and ROACH-2 are over the rack. In left side of the picture the Signal Generator Anritsu MG3604C, it is the LO source. Under the ROACH-II is shown the DC supply that feeds the four amplifiers connected in parallel to +5V. On the rack shelf below the Signal Generator Agilent E8257D is the RF source.

4.3. Polarization Synthesis using the ideal gain matrix

To validate the correct working of the digital OMT we synthesize the polarization vectors with an ideal Gain matrix. This is done by loading the ideal H matrix (eq. 4.1) to the FPGA. Figure 4.3 shows the un-calibrated X-pol and Y-pol spectra for a 12.15GHz test tone, the LO signal was set to 12GHz. Spurious signals are generated in the ADC and can be seen at -45dBc limiting the spurious free dynamic range to about 45dB. The cross-polarization isolation in this example exceeds 40dB. As the G and H matrices are real, this result would explain that the final calibration constants should be close to the ideal calibration constants with phases coupled to 0° and 180° that compensate the gain imbalances that the orthogonal ports present, regarding co-polar signal of the OMT.

$$[H] = \begin{bmatrix} \frac{1}{2} & 0 & \frac{-1}{2} & 0 \\ 0 & \frac{1}{2} & 0 & \frac{-1}{2} \end{bmatrix} \quad (4.1)$$

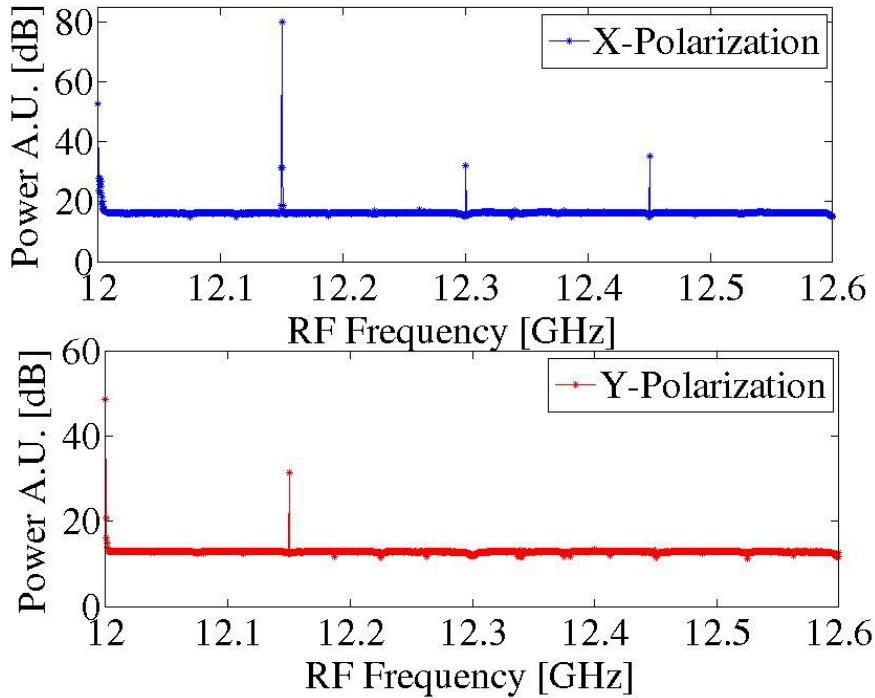


Figure 4.3. Co-pol and Cross-pol spectra of the uncalibrated Digital OMT. LO was set to 12GHz and the RF was 12-12.6[GHz]. Spurious signals appear along side the band.

In Figure 4.4 the measured cross-polarization isolation for X-Pol (in blue) and Y-pol (in green) using the ideal gain matrix is presented. This experiment presents a wide sweep along the Ku band of 12 to 18 GHz divided into 10 sub-bands of 600 MHz. The cross-polarization isolation ratio exhibits short sections of the band that are over 40dB. The spikes correspond to LO spurs and DC.

The next step consists of calibrating the OMT to get calibrated cross-polarization isolation. The calibration process is presented in the following section.

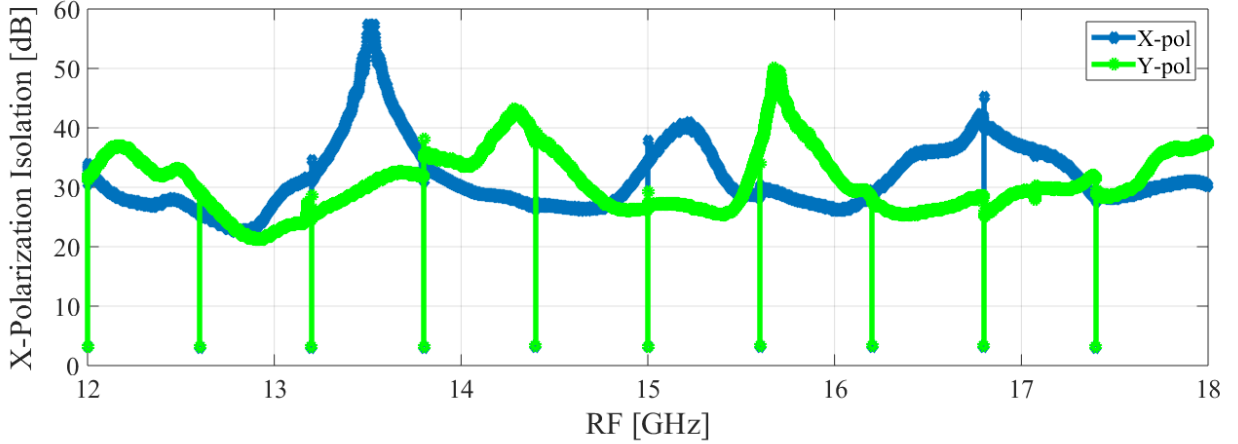


Figure 4.4. Measured Cross-Polarization Isolation for X-Pol and Y-pol using the ideal gain matrix.

4.4. Calibration

The sources of the calibration data - it was obtained through calibration with an SSB receiver. The block diagram of the test setup is in Figure 3.1.

Although the measurements of Matt Morgan et al. [5] were done on a 2SB receiver, there isn't any reason why it shouldn't work for an SSB receiver also. The operational principles are the same, and no assumption was made about the downconversion aspect of the receiver. In Matt Morgan's formulation there is a notational typo that would confuse the reader of this work. The pseudo-inverse matrix, H , defined in Eq. 4.2 should be:

$$H = (G^\dagger G)^{-1} G^\dagger \quad (4.2)$$

In other words, it should use the CONJUGATE transpose¹ of G , not the simple transpose as written in the paper.

In order to obtain a precise reconstruction of the polarization vector, S , we must first calibrate the DOMT spectrometer by computing the complex constants of the gain matrix, G , which characterize the Analog Front-End.

A proper implementation of an off-line numerical calibration to determine elements of the gain matrix G leads to the following question: how could one find the elements of the matrix G , which would provide a unique solution of Eq. 2.31, $S' = HV$, that compensates the gain imbalances that the orthogonal ports present, regarding co-polar signals of the OMT?

In response to that question, a second spectrometer was designed to measure the amplitude and phase of both I and Q channels. The calibration spectrometer, instead of accumulating the downconverted power spectrum, it records the complex spectral data. Figure 4.5 shows the block diagram of the calibration spectrometer used to measure the amplitude and phase for each IF output. This technique was proposed in Finger et al. [6], the equation (4.3) presents the FFT channel of the calibration spectrometer in terms of $n = 1, 2, 3, 4$.

$$V_n = v_n e^{j\phi_n} \quad (4.3)$$

¹unary operator \dagger indicates Conjugate Transpose of Complex Matrix.

As shown in Figure 3.1 four IF bandwidths coming from the front-end after a single sideband down-conversion are then digitized by four 8-bit ADCs with a sampling rate of 1.2GSPS. The data is then passed to four independent PFBs (Polyphase Filter Banks). The PFBs consist of an FIR filter and the 2048 channel Fast Fourier Transform (FFT) block. After the computation of the FFT, the channels are split and stored in real and imaginary parts and then they are recorded in 64-bit BRAMs during 512 clocks. Finally, the instantaneous Fourier spectra is retrieved by a desktop computer using a Python script.

Figure 4.5 shows the block diagram of the calibration spectrometer proposed to measure the amplitude and phase at each IF output.

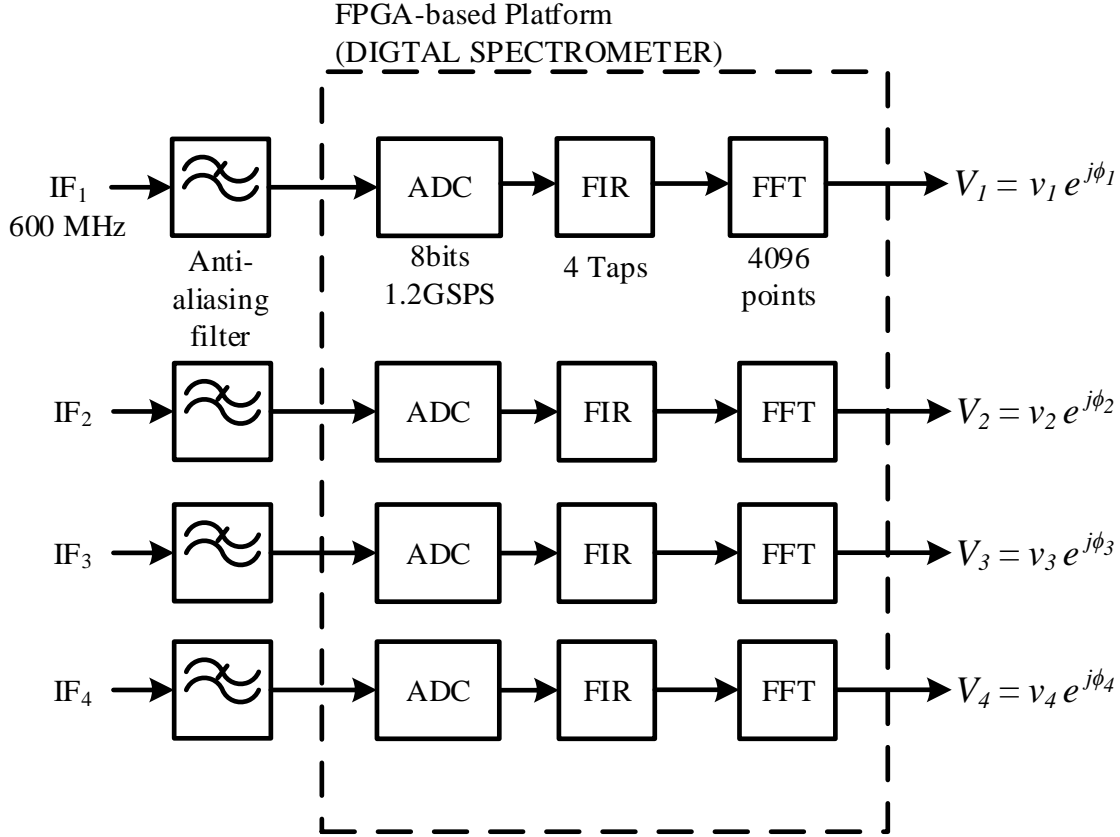


Figure 4.5. Schematic of the DOMT calibrating spectrometer. Four identical branches were implemented to compute a set of calibration constants to compensate the system imbalances of the analog Front-End. The 4 FIR filters and 4 FFTs were implemented in a FPGA Virtex-6.

To obtain G matrix by Calibration measurement we set the OMT in three incident angles, defined as α . Initially, we take two measurements, first with the input test signal at $\alpha = 0^\circ$, the second measurement with the input test signal at $\alpha = 90^\circ$. Finally, we must resolve the relative reference between the two previous measurements which are x and y columns in G. So, a third calibration measurement is taken with the input test signal at $\alpha = 45^\circ$. To further this discussion the reader can go to section 2.2.

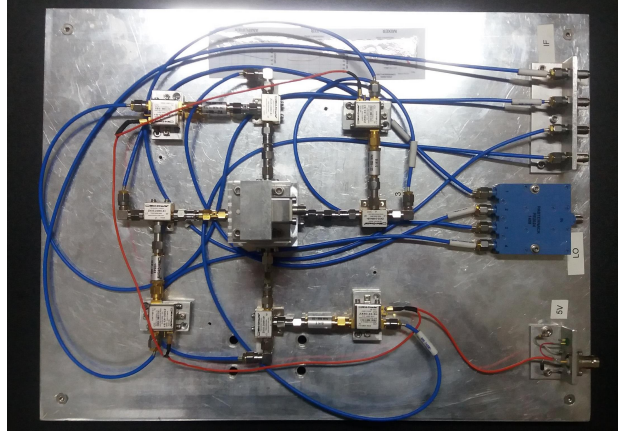


Figure 4.6. Photograph of the Digital Orthomode Transducer Test-Setup. The initial calibration measurement was taken with the input transition set at $\alpha = 0^\circ$.

In Figure 4.6 the initial arbitrary position called $\alpha = 0^\circ$ due to the incident angle taken as the first measurement. Regarding the photograph symmetry this was done by exciting the probes 1 and 3 in co-polarization.

In Figure 4.7 the second position called $\alpha = 90^\circ$ due to the input transition being rotated 90° clockwise. Regarding the photograph symmetry this was done by exciting the probes 2 and 4 in co-polarization.

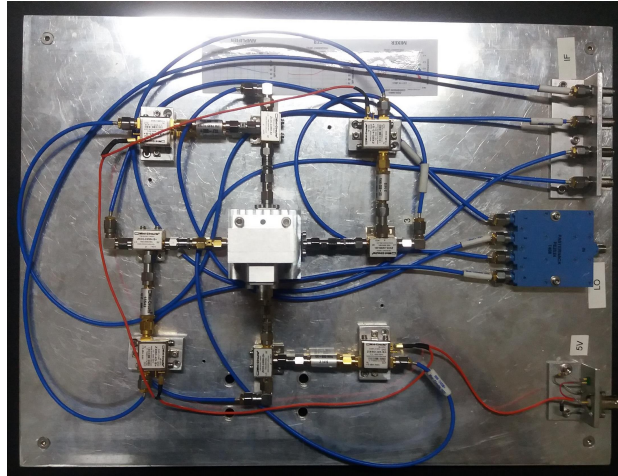


Figure 4.7. Photograph of the digital orthomode transducer test setup. The second calibration measurement was taken with the input transition rotated 90° clockwise. $\alpha = 90^\circ$.

In Figure 4.8 the third position called $\alpha = 45^\circ$ due to the input transition being rotated 45° anticlockwise. Regarding the photograph symmetry this was done by exciting the four probes with the same power but two of them have a phase difference of about 180° in relation to the other two. The gain matrices resulting from the three measurement calibration procedure described in Section 2.3 are shown in Figures [4.9-4.13].

From the plots we can infer the following things. The approximate magnitude of the gain terms fit are almost one, where some deviation is expected due to different amplifier gains in the analog hardware after the probes, and some signs of standing waves in the first band section.

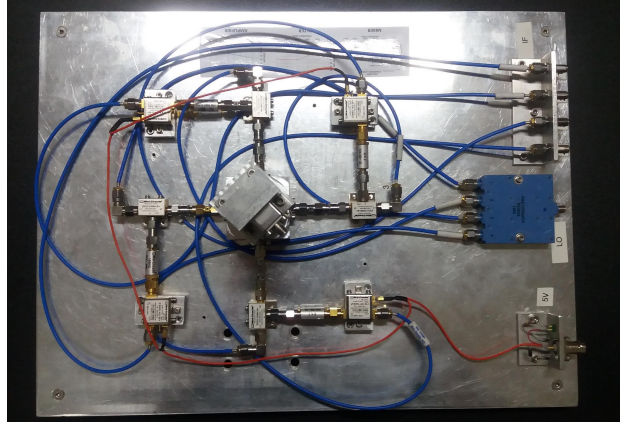


Figure 4.8. Photograph of the digital orthomode transducer test setup. The third calibration measurement was taken with the input transition rotated 45° anticlockwise. $\alpha = 45^\circ$.

Second, the channels that present amplitude imbalances should be corrected once the calibrated complex coefficients are loaded into the DOMT. The angle for orthogonal probes during measurements are noisy due to them having indeterminate phase relative to the reference probe. The hypothesis presented by Matt Morgan and R. Fisher et al. is founded on the fact that the orthogonal probes did not provide useful information about the given component x , or y , of the input signal.

Also, in practice it is a simple matter for the calibration algorithm to choose the one probe in each column which has the largest gain magnitude, a_x or a_y , and thus the strongest correlation to the input signal to use as the reference. The software needs only to do its best to determine the phase angles of the rest of the terms in that column. The ones that are approximately orthogonal could potentially be very noisy, but this should not matter because the entire term will receive a very small weight in the final solution.

In Matt Morgan’s formulation, “ s_0 ” is simply the voltage amplitude of the calibration test tone, measured at the input to the receiver. Its only real purpose is to establish an absolute amplitude scale for calibration of the receiver. In most cases, that isn’t really needed (since astronomers tend to calibrate the entire instrument to external sources on the sky anyway). For all of this work, it just let $s_0 = 1$ in arbitrary units. As long as the test tone is constant in amplitude as it sweeps across frequency and change polarization, then it should have no effect on the performance of the calibration. On the other hand, if its amplitude does vary across the band, then that variation will appear as gain ripple/slope in its calibrated output.

4.4.1. Elements of the gain matrix G :

Since the implementation of an off-line numerical calibration to determine elements of the gain matrix G was done, described in equation 2.27. Figure [4.9-4.13] shows the gain matrices resulting from the three measurement calibration procedures described in equation 2.27. The data of the gain matrix coefficients look quite reasonable for a four-probe OMT. Also, since calibration phases obtained for the strongly coupled components are close to 0 and 180, the G and H matrices are nearly real, which would explain why the results are close, but not quite perfect.

The reader should notice, in Figures 4.11-4.13, that the orthogonal phases are constrained to their principal value, in the interval $([-\pi, \pi])$, it is called wrapped phase.

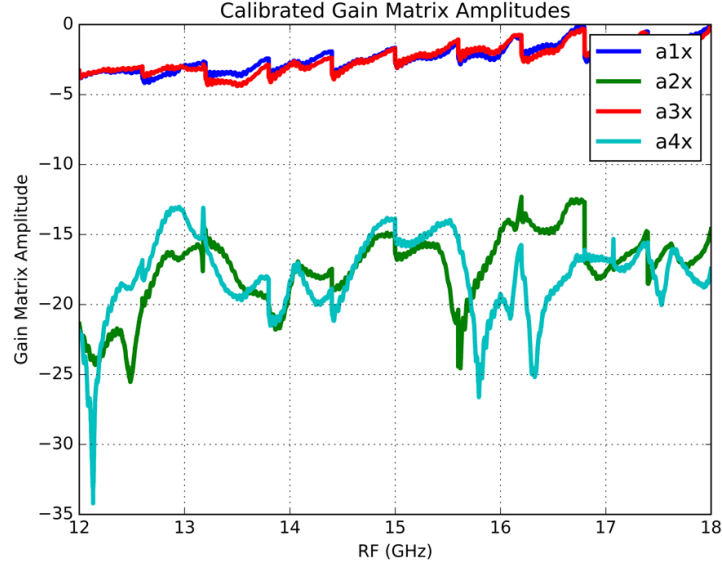


Figure 4.9. Measured gain matrix amplitudes, a_x , for the X probes of the digital orthomode transducer. A sweep along the Ku band of 12 to 18 GHz divided into 10 sub-bands of 600 MHz.

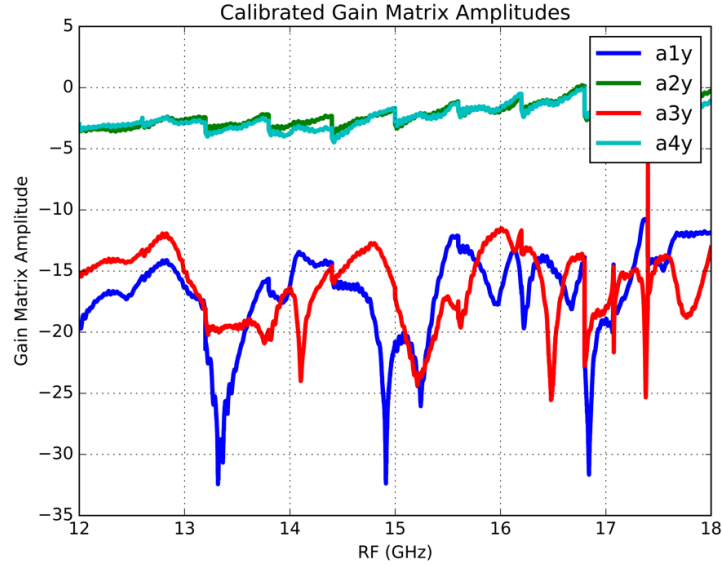


Figure 4.10. Measured gain matrix amplitudes, a_y , for the Y probes of the digital orthomode transducer. A sweep along the Ku band of 12 to 18 GHz divided into 10 sub-bands of 600 MHz.

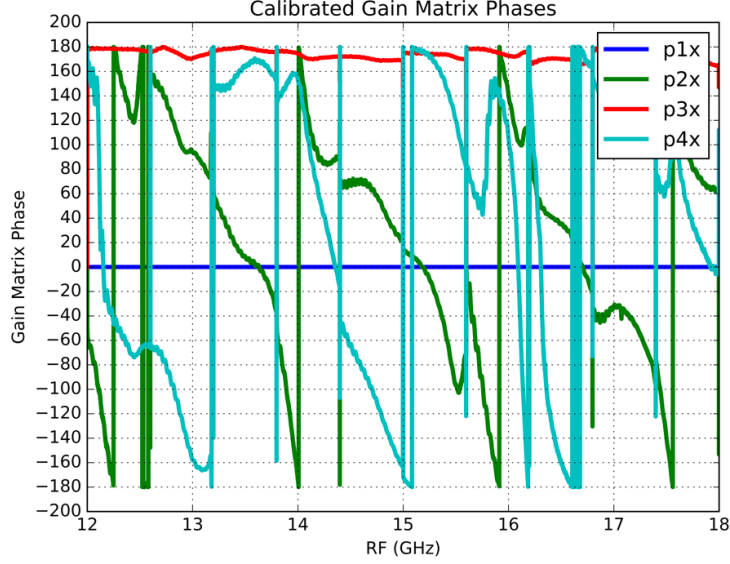


Figure 4.11. Measured gain matrix phases, p_x , for the X probes of the digital orthomode transducer. The phases p_{1x} and p_{3x} for the co-polar components are close to 0 and 180. A sweep along the Ku band of 12 to 18 GHz divided into 10 sub-bands of 600 MHz.

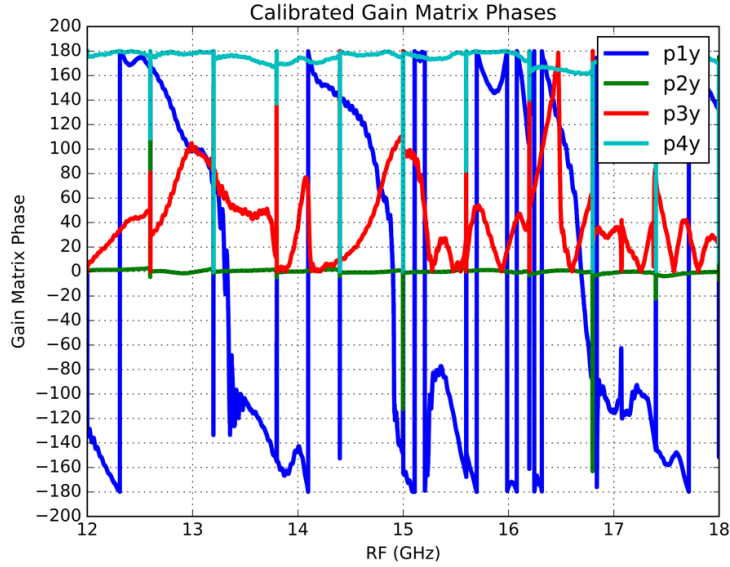


Figure 4.12. Measured gain matrix phases, p_y , for the Y probes of the digital orthomode transducer. The phases p_{2y} and p_{4y} for the co-polar components are close to 0 and 180. A sweep along the Ku band of 12 to 18 GHz divided into 10 sub-bands of 600 MHz.

4.5. Synthesis measurements

In Figure 4.13 the measured cross-polarization isolation measured for X-Pol and Y-pol using the calibrated gain matrix is presented. A wide sweep along the Ku band of 12 to 18 GHz divided into 10 sub-bands of 600 MHz. Four IF bandwidths coming from the front-end after a single sideband down-conversion are then digitized by four 8-bit ADCs with a sampling

rate of 1.2GSPS.

A set of calibration gain coefficients were loaded on the FPGA, with the aim of compensating the imbalances of amplitude and phase presents in the analog front-end.

The cross-polarization isolation ratio exhibits sections of the band that are over 40dB. The spikes correspond to LO spurs and DC.

When the test tone amplitude on the cross-polarized band is less than the spurious signal content, the cross-polarization isolation is measured as the ratio of the test tone in the pass band to the stronger spurious signals in the cross-polarized band, so the measurement is limited by the ADC spurious-free dynamic range to about 45 dB.

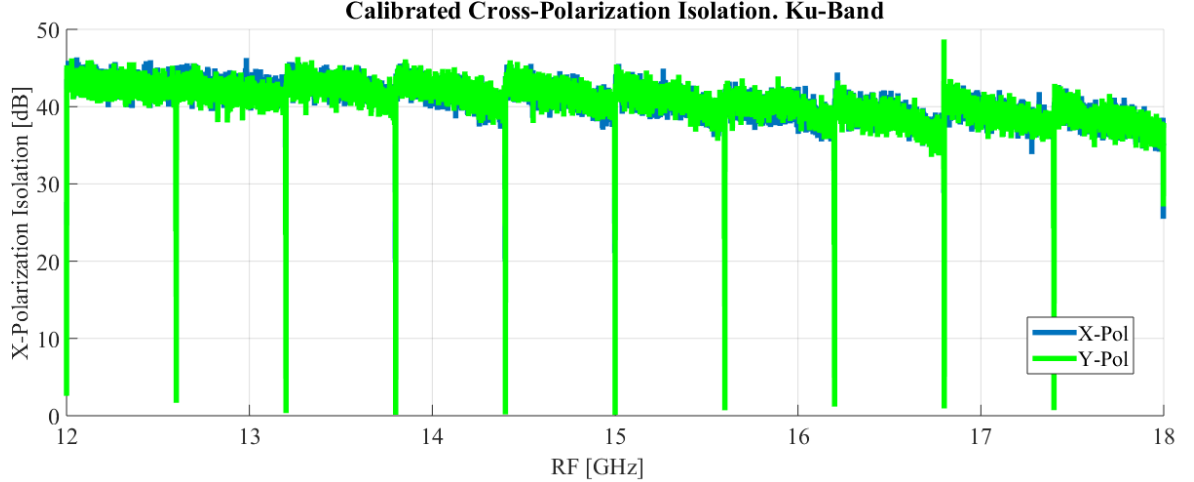


Figure 4.13. Full Ku-Band measure of the cross-polarization isolation for the four-probe DOMT. The result measured immediately after loading the calibration constants to the FPGA. A sweep along the Ku band of 12 to 18 GHz divided into ten sub-bands of 600 MHz. The first measurement, blue plot, is the cross-polarization isolation for X-pol and then the second measurement, green plot, is the cross-polarization isolation for Y-pol.

4.5.1. Discussion and Conclusions

Equation 2.31 states what the pseudo-inverse should result in, presuming the receiver behaves according to Eq. 2.27. If we substitute Eq. 2.28 and Eq. 2.30 in Eq. 2.31, the result is Eq. 4.4:

$$S' = HV = (G^*G)^{-1}V = (G^*G)^{-1}G^*GS = S \quad (4.4)$$

So if Eq. 2.28 is an exact and true model of how the receiver behaves, then Eq. 2.31 dictates how the input sky signals, referred to as S , are recovered and mathematically describes the receiver voltage outputs, referred to as V . Prime notation, referred to as S' , is used because, in practice, V is obtained not from an ideal model, but from imperfect measurements. Since the problem is over-constrained with too many measurements for too few variables, the pseudo-inverse does not result in an exact solution, but rather a closer fit.

On the other hand, if it is possible to measure its gain terms, G , then you can determine H from Eq. 2.30. The receiver has to be linear for Eq. 2.28 to be a valid model, and it has to be stable so that the coefficients derived from calibration remain accurate.

Based on the stated before:

Calibration results gain amplitudes at about -3 dB, and phase about 0° or 180°. (The other phase terms vary widely, but the amplitude for those terms are small). So the gain matrix G is approximately Eq. 4.5:

$$G = \frac{1}{\sqrt{2}} \begin{bmatrix} 1 & 0 \\ 0 & 1 \\ -1 & 0 \\ 0 & -1 \end{bmatrix} \approx \begin{bmatrix} 0.7071 & 0 \\ 0 & 0.7071 \\ -0.7071 & 0 \\ 0 & -0.7071 \end{bmatrix} \quad (4.5)$$

This is essentially identical to Eq. 4.6, but for a pre-factor of $\frac{1}{\sqrt{2}}$, which just affects the absolute amplitude scale and has no impact on the isolation.

$$G = \frac{1}{\sqrt{2}} \begin{bmatrix} 1 & 0 \\ 0 & 1 \\ -1 & 0 \\ 0 & -1 \end{bmatrix} \quad (4.6)$$

These terms are frequency-dependent. In order to simplify the math the G terms are constant. In Eq. 4.7 shown below values were changed randomly to add a little gain variation and leakage terms:

$$G_{act} = \begin{bmatrix} 0.71 & 0.1 \\ -0.05 & 0.75 \\ -0.69 & 0.07 \\ 0.02 & -0.74 \end{bmatrix} \quad (4.7)$$

Eq. 4.7 is the actual gain matrix of the receiver. But our calibration measurement is imperfect, so when calibrated, similar values are obtained, but not identical:

$$G_{meas} = \begin{bmatrix} 0.7 & 0.09 \\ -0.06 & 0.75 \\ -0.68 & 0.08 \\ 0.01 & -0.75 \end{bmatrix} \quad (4.8)$$

The H matrix is then derived from the *measured* gain matrix:

$$H = (G_{meas}^* G_{meas})^{-1} G_{meas}^* = \begin{bmatrix} 0.7371 & -0.0326 & -0.7093 & -0.0198 \\ 0.1074 & 0.6569 & 0.0429 & -0.6589 \end{bmatrix} \text{ (this one by matlab)} \quad (4.9)$$

Once the calibration is done, the receiver will be tested with a perfect x-pol signal as shown in Eq. 4.10:

$$S = \begin{bmatrix} 1 \\ 0 \end{bmatrix} \quad (4.10)$$

The actual outputs of the receiver are determined by the actual gain matrix,

$$V = G_{act} S = \begin{bmatrix} 0.71 & 0.1 \\ -0.05 & 0.75 \\ -0.69 & 0.07 \\ 0.02 & -0.74 \end{bmatrix} \begin{bmatrix} 1 \\ 0 \end{bmatrix} = \begin{bmatrix} 0.71 \\ -0.05 \\ -0.69 \\ 0.02 \end{bmatrix} \quad (4.11)$$

However, when voltages are multiplied by the imperfectly calibrated H matrix, a very close approximation of the input is obtained, $S' \approx S$, as shown in Eq. 4.12.

$$S' = HV = \begin{bmatrix} 0.7371 & -0.0326 & -0.7093 & -0.0198 \\ 0.1074 & 0.6569 & 0.0429 & -0.6589 \end{bmatrix} \begin{bmatrix} 0.71 \\ -0.05 \\ -0.69 \\ 0.02 \end{bmatrix} \approx \begin{bmatrix} 1.0139 \\ 0.0006 \end{bmatrix} \text{ (by matlab)} \quad (4.12)$$

The central piece of this algorithm, the Moore-Penrose pseudo-inverse, was implemented using the matlab pinv function². The reader may verify the above results to understand this formulation in more depth.

²Further information for that function is available on the following link: <https://www.mathworks.com/help/matlab/ref/pinv.html>

Chapter 5

Conclusion

This thesis demonstrates that the Calibratable Digital OMT created by the Millimeter Wave Laboratory for real-time processing of RF signals and continuous integration of spectra is suitable for radio astronomy because the Polarization Isolation obtained proves to be stable in the whole Ku-band on the order of 45dB.

This OMT prototype used was designed to reconstruct incoming linear polarization without the aid of analog baluns or hybrids. Showing that the architecture of the WR-62 rectangular waveguide to circular waveguide taper, finished in a four-port OMT serves as a starting point to separate polarizations which are generated by injecting signals through the probe antenna.

For the purpose of studying the manufacturing tolerances involved and any potential angular misalignments of the probes the cross-polarization of the device was intentionally degraded by 10dBm, introducing typical issues which degrade astronomical OMTs performance under simulation and electromagnetic characterization of S parameters.

Calibrating the degraded OMT demonstrated that the polarization synthesis algorithm was capable of compensating for amplitude and phase imbalances typical of analog radio astronomy front-ends. Despite the obtained calibration measurement's being imperfect, the calibration procedure guaranteed that the final axes are orthogonal, even when the calibration sources themselves are not.

It was shown that the pioneering previously-tested method of calibration and synthesis, Matt Morgan et al., could be implemented on a real-time digital spectrometer, using an FPGA, reaching a polarization isolation ratio of 45 dB on average for the entire RF bandwidth in the Ku-band, representing an improvement factor of 100 over its analog counterpart.

The work carried out demonstrates that the use of fast ADCs and FPGA based platforms to perform signal processing, currently being implemented by analog means, can substantially increase the performance of OMTs, particularly highly miniaturized OMTs which are more prone to being affected by manufacturing tolerances.

Bibliography

- [1] Barraeto, I., *DEVELOPEMENT OF MICROWAVE DEVICES FOR MILLIMETER AND SUB-MILLIMETER RECEIVERS*, master of science, thesis, in electrical engineering, Universidad de Chile, Santiago, Chile (May 2017).
- [2] Proakis, J. G. and Manolakis, D. G., [*Digital signal processing: principles, algorithms, and applications*], Pearson Prentice Hall (2007).
- [3] Burke, B. F. and Graham-Smith, F., [*An introduction to radio astronomy*], Cambridge University Press (2009).
- [4] Barraeto, I., Reyes, N., Mena, P., and Bronfman, L., “A broadband orthomode transducer for the new alma band 2+ 3 (67–116 ghz),” in [*Millimeter Waves (GSMM) & ESA Workshop on Millimetre-Wave Technology and Applications, 2016 Global Symposium on*], 1–4, IEEE (2016).
- [5] Morgan, M. A., Fisher, J. R., and Boyd, T. A., “Compact orthomode transducers using digital polarization synthesis,” *Microwave Theory and Techniques, IEEE Transactions on* **58**(12), 3666–3676 (2010).
- [6] Finger, R., Mena, P., Reyes, N., Rodriguez, R., and Bronfman, L., “A calibrated digital sideband separating spectrometer for radio astronomy applications,” *Publications of the Astronomical Society of the Pacific* **125**(925), 263 (2013).
- [7] Dunning, A., “Double ridged orthogonal mode transducer for the 16–26 ghz microwave band,” in [*Proceedings of the Workshop on the Applications of Radio Science*], (2002).
- [8] Bøifot, A., Lier, E., and Schaug-Pettersen, T., “Simple and broadband orthomode transducer,” in [*IEE Proceedings H (Microwaves, Antennas and Propagation)*], **137**(6), 396–400, IET (1990).
- [9] Navarrini, A. and Plambeck, R. L., “A turnstile junction waveguide orthomode transducer,” *IEEE Transactions on Microwave Theory and Techniques* **54**(1), 272–277 (2006).
- [10] Chattopadhyay, G., Miller, D., LeDuc, H. G., and Zmuidzinas, J., “A dual-polarized quasi-optical sis mixer at 550 ghz,” *IEEE Transactions on Microwave Theory and Techniques* **48**(10), 1680–1686 (2000).
- [11] Morgan, M. A. and Fisher, J. R., “Next generation radio astronomy receiver systems,”

arXiv preprint arXiv:0908.3849 (2009).

- [12] Gonzalez, A. and Uzawa, Y., “Investigation on alma band-4 frequency-dependent cross-polarization,” *IEEE Transactions on Terahertz Science and Technology* **4**(2), 184–192 (2014).
- [13] Morgan, M. A. and Fisher, J. R., “Experiments with calibrated digital sideband-separating downconversion,” *Publications of the Astronomical Society of the Pacific* **122**(889), 326 (2010).
- [14] Grimes, P., King, O., Yassin, G., and Jones, M., “Compact broadband planar orthomode transducer,” *Electronics Letters* **43**(21), 1146–1148 (2007).
- [15] Mauskopf, P., Zhang, J., Ade, P., Withington, S., and Grime, P., “Clover polarimetric detector-a novel design of an ortho-mode transducer at 150 and 225 ghz,” in [*Infrared, Millimeter and Terahertz Waves, 2008. IRMMW-THz 2008. 33rd International Conference on*], 1–2, IEEE (2008).
- [16] “Roach2.” https://casper.berkeley.edu/wiki/ROACH-2_Revision_2. Accessed: 2015-09-30.
- [17] “Casper.” <https://casper.berkeley.edu/>. Accessed: 2015-09-30.
- [18] Pozar, D. M., “Microwave engineering 3e,” *Transmission Lines and Waveguides*, 143–149 (2005).
- [19] of Electrical, I. and Engineers, E., [*IEEE Standard Definitions of Terms for Antennas*], IEEE (1983).
- [20] Balanis, C. A., [*Antenna theory: analysis and design*], John Wiley & Sons (2016).
- [21] Penrose, R., “A generalized inverse for matrices,” in [*Mathematical proceedings of the Cambridge philosophical society*], **51**(3), 406–413, Cambridge University Press (1955).
- [22] Finger, R., *Design and Construction of a Digital Sideband Separating Spectrometer for the 1.2-meter Southern Radio Telescope*, ph.d. thesis, Universidad de Chile, Facultad de Ciencias Físicas y Matemáticas, Santiago, Chile (March 2013).
- [23] Wilson, T. L., Rohlf, K., and Hüttemeister, S., [*Tools of radio astronomy*], vol. 86, Springer (2009).
- [24] Alvear, A., Finger, R., Fuentes, R., Sapunar, R., Geelen, T., Curotto, F., Rodríguez, R., Monasterio, D., Reyes, N., Mena, P., et al., “Fpga-based digital signal processing for the next generation radio astronomy instruments: ultra-pure sideband separation and polarization detection,” in [*SPIE Astronomical Telescopes+ Instrumentation*], 99141E–99141E, International Society for Optics and Photonics (2016).
- [25] Sapunar Opazo, R. I., “Diseño e implementación de un espectrómetro de alta resolución basado en fpga para análisis de señales radioastronómico,” (2015).

- [26] Gowda, S., “A 3gigahertz bandwidth fpga spectrometer,” *Unpublished Technical Report*, http://casper.berkeley.edu/wiki/3GHz_Spectrometers (2010).
- [27] “Virtex-6 family overview (datasheet).” http://www.xilinx.com/support/documentation/data_sheets/ds150.pdf. Accessed: 2016-05-30.
- [28] “Dsp48 slice.” <http://www.xilinx.com/technology/dsp/xtremedsp.htm>. Accessed: 2016-05-30.
- [29] Farooq, U., Parvez, H., Mehrez, H., and Marrakchi, Z., “Exploration of heterogeneous fpga architectures,” *International Journal of Reconfigurable Computing* **2011**, 2 (2011).
- [30] Tilden, S. et al., “Ieee standard for terminology and test methods for analog-to-digital converters,” *IEEE Std 1241-2010 (Revision of IEEE Std 1241-2000)*, 1–139.
- [31] Brisk, P., Verma, A. K., Ienne, P., and Parandeh-Afshar, H., “Enhancing fpga performance for arithmetic circuits,” in *[Proceedings of the 44th annual Design Automation Conference]*, 334–337, ACM (2007).
- [32] Farooq, U., Marrakchi, Z., and Mehrez, H., “Fpga architectures: An overview,” *Tree-based Heterogeneous FPGA Architectures*, 7–48 (2012).
- [33] Inc., X., *[Virtex-6 FPGA Configurable Logic Block]*, Xilinx Inc. (2012).
- [34] Inc., X., *[Mixed-Mode Clock Manager (MMCM) Module (v1.00a) - Data Sheet 737]*, Xilinx Inc. (2009).
- [35] Stavinson, E., *[100 Power Tips for FPGA Designers]*, Evgeni Stavinson (2011).
- [36] “Virtex-5 family overview (datasheet).” http://www.xilinx.com/support/documentation/data_sheets/ds100.pdf. Accessed: 2016-05-30.
- [37] “Development system reference guide.” <http://www.xilinx.com/itp/xilinx10/books/docs/dev/dev.pdf>. Accessed: 2016-09-30.
- [38] Inc., X., *[Command Line Tools User Guide]*, Xilinx Inc. (2009).
- [39] Bhasker, J. and Chadha, R., *[Static timing analysis for nanometer designs: A practical approach]*, Springer Science & Business Media (2009).
- [40] Alvear, A., *Extensión del Ancho de Banda de Espectrometros Radioastronómicos Basados en FPGA*, engineering thesis, PUCV, EIE, Valparaíso, Chile (March 2014).
- [41] Ansoft, L., “An introduction to hfss fundamental principles, concepts, and use,” *Ansoft, Pittsburgh*, 88 (2009).
- [42] “Ev8aq160 quad adc.” <https://casper.berkeley.edu/wiki/images/1/19/Ev8aq160.pdf>. Accessed: 2016-05-16.
- [43] “5007 dual 137.5-4400mhz frequency synthesizer module.” <http://valontechnology>.

com/5007/5007_r4_ds.pdf. Accessed: 2016-05-30.

- [44] Sapunar, R., *Diseño e implementación de un espectrómetro de alta resolución basado en FPGA para el análisis de señales radioastronómicas*, engineering thesis, Universidad de Chile, Santiago, Chile (March 2015).
- [45] “tyco - z-dok high-performance docking connector.” http://www.te.com/documentation/electrical-models/files/epr/EPR-22GC007_Zdok_RA-P_RA-R.pdf. Accessed: 2018-03-25.
- [46] “Ev8aq160 quad core adc.” <https://casper.berkeley.edu/wiki/images/1/19/Ev8aq160.pdf>. Accessed: 2015-09-30.

Appendices

Appendix A

FPGA-based digital signal processing
for the next generation radio
astronomy instruments: ultra-pure
sideband separation and polarization
detection

FPGA-based digital signal processing for the next generation radio astronomy instruments: ultra-pure sideband separation and polarization detection

Andrés Alvear^a, Ricardo Finger^a, Roberto Fuentes^a, Raúl Sapunar^a, Tom Geelen^b, Franco Curotto^c, Rafael Rodríguez^a, David Monasterio^a, Nicolás Reyes^c, Patricio Mena^c, and Leonardo Bronfman^a

^aUniversidad de Chile, Department of Astronomy, Santiago, Chile

^bTechnical University of Eindhoven, Eindhoven, Netherlands

^cUniversidad de Chile, Department of Electrical Engineering, Santiago, Chile

ABSTRACT

Field Programmable Gate Arrays (FPGAs) capacity and Analog to Digital Converters (ADCs) speed have largely increased in the last decade. Nowadays we can find one million or more logic blocks (slices) as well as several thousand arithmetic units (ALUs/DSP) available on a single FPGA chip. We can also commercially procure ADC chips reaching 10 GSPS, with 8 bits resolution or more. This unprecedented power of computing hardware has allowed the digitalization of signal processes traditionally performed by analog components. In radio astronomy, the clearest example has been the development of digital sideband separating receivers which, by replacing the IF hybrid and calibrating the system imbalances, have exhibited a sideband rejection above 40dB; this is 20 to 30dB higher than traditional analog sideband separating (2SB) receivers. In Rodríguez et al.,¹ and Finger et al.,² we have demonstrated very high digital sideband separation at 3mm and 1mm wavelengths, using laboratory setups. We here show the first implementation of such technique with a 3mm receiver integrated into a telescope, where the calibration was performed by quasi-optical injection of the test tone in front of the Cassegrain antenna. We also reported progress in digital polarization synthesis, particularly in the implementation of a calibrated Digital Ortho-Mode Transducer (DOMT) based on the Morgan et al. proof of concept.³ They showed off-line synthesis of polarization with isolation higher than 40dB. We plan to implement a digital polarimeter in a real-time FPGA-based (ROACH-2) platform, to show ultra-pure polarization isolation in a non-stop integrating spectrometer.

Keywords: FPGA, Digital sideband separation, Digital orthomode transducer, ROACH, OMT, 2SB receiver

1. INTRODUCTION

New challenges of astronomy require the use of a new hardware. An area that has been identified to limit receivers' performance is the amplitude and phase imbalance of parallel receiver channels required for sideband separation and polarization detection. Incorporating digitalization and arithmetic processing in crucial parts of the receiver chain has been proposed as a possible solution for current analog technology limitations.⁴ Traditionally high bandwidth signal processing is performed by analog components (splitters, hybrids, filters, etc), but recent advances in digital hardware have allowed the digitalization of some of the signal processing fund in radio astronomy receivers. In 2010, we identified the fast growing trend of digitization of radio astronomy instruments Alex Murk et al.⁶ and M. Morgan and J. Fisher⁷ and joined the Collaboration for Astronomy Signal Processing and Electronics Research⁸ (CASPER), led by UC Berkeley. We acquired state of the art digital re-configurable hardware based on high-performance FPGAs and fast ADCs and began researching in novel ways of using digital technology to improve radio astronomy receiver performance. We have developed two prototype digital receivers suitable for radio astronomy operations. The first is a Calibrated Digital Sideband Separating receiver which performs the IF recombination in digital arithmetic, replacing the IF hybrid by a fixed point processor. After

Further author information:

Ricardo Finger: E-mail: rfinger@u.uchile.cl

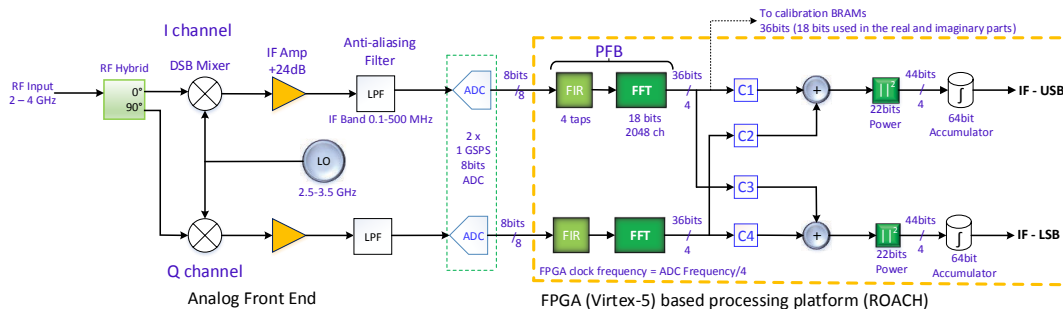


Figure 1: Digital Sideband Separating Receiver Block Diagram.⁵

calibration, it can compensate for amplitude and phase imbalances in the analog portion of the receiver to produce high sidebands rejections. The second consists of a Digital OMT that allows the correction of analog OMTs' cross-polarization leakage allowing optimal observation of weakly polarized astronomical sources.

In this paper, we show a summary of the results of previous and current work on digital sideband separation and the latest developments on digital polarization detection. The first Calibrated Digital Sideband Separating Receiver was implemented using a 4 GHz test front-end. This receiver was designed to study the possibility of implementing the large dual-channel FFT spectrometer and digital IF hybrid required for this application in a single FPGA chip as shown in Figure 1. The work showed that high-end FPGAs were capable of handling the large data rates required by this particular application and that the calibration process can indeed compensate front-end imbalances in real time operation. This 2SB receiver showed a sideband rejection of 50 dB, a factor of 100 to 1000 higher than current analog technology. The work was published in Finger et al.⁹ in 2013 and produced good interest in the astronomical instrumentation community with a number of incoming collaboration proposals. Finger's work was continued by Ph.D. student Rafael Rodriguez, in 2013, while he worked on the upgrade of the Southern Millimeter Wave Telescope (SMWT – 1.2m mm-wave Radio Telescope¹⁰). Rodriguez decided to implement the technique in an astronomical-grade mm-wave receiver. In Rodriguez et al.¹ we showed the integration of the digital hybrid and FFT spectrometer in a laboratory test receiver at 3mm wavelength (~100 GHz) showing a similar performance to the reported in 2013 using the 4 GHz test front-end, and far beyond the state of the art of 100 GHz receivers.

Following Rodriguez's work, the SMWT was equipped with a Digital Sideband Separating receiver (2SB receiver), where the calibration was performed by quasi-optical injection of the test tone at the secondary mirror of the Cassegrain antenna. The results in the SMWT exhibit an Image rejection above 30dB in the whole IF band, in both Lower Side Band (LSB) and Upper side Band (USB). The results and discussions of this work are presented in this paper. In 2014 we collaborated with SRON (Netherlands Institute for Space Research) in order to demonstrate that this technique could be used to improve ALMA band 9 sideband rejection, and in general that the method can be applied to sub-millimeter SIS receivers.

In 2015, we reported the implementation of an ALMA Band-9 digital 2SB receiver using two down-conversion stages. We found an average sideband rejection of 45.9 dB while small portions of the band dropped below 40 dB. The performance was 27 dB (a factor of 500) higher than the average performance of the proof-of-concept Band 9 purely-analog 2SB prototype receiver developed by SRON.²

In 2015 we began working in Digital Polarization Detection. A proof of concept of this technique has been reported by M.Morgan and R.Fisher³ showing a dramatic reduction of cross-polarization compared with current analog Orthomode Transducer (OMTs). In Morgan and Fisher's Digital Orthomode Transducer (DOMT) the incoming signal is coupled to a set of probes into a circular waveguide. The several data streams are then digitized and arithmetically combined to synthesize the incoming polarization state. Before the signal recombination, a set of complex constants allowed calibrating gain and phase imbalances introduced by the OMT's waveguide portions, to reconstruct the original polarization state with unprecedented purity. In Morgan and Fisher's work the signal processing is done off-line (in software), after buffering the digitalized signal.

We present the current state of the implementation of a DOMT on a real-time FPGA-based processor capable of non-stop integration.

2. DIGITAL SIDE-BAND SEPARATION SPECTROMETERS:

This section presents an overview of our results obtained with the digital sideband separating spectrometer developed by the Millimeter Wave Laboratory (MWL). In order to address the different stages of the research, we begin summarizing the results of the proof of concept developed in 2013, followed by the achievements during 2014 with a millimeter-wave receiver; both were laboratory setups. We finish with the results of the 3mm receiver performance installed and calibrated in the SMWT and the ALMA Band-9 digital sideband separating prototype.

2.1 Hardware Description

Figure 1 presents the block diagram of the digital sideband separating spectrometer. The receiver has an analog front-end from 2GHz to 4GHz, presented in Figure 6. The front-end was built with commercial components to mimic the functionality of the typical analog heterodyne receivers. After the 90° RF hybrid we down-convert the input signal using a 2.5-3.5 GHz local oscillator (LO). After amplification and anti-aliasing filtering the outputs are digitalized to 8 bits by a fast ADC, ADC083000 of National Semiconductor,¹¹ at 1GSPS allowing the processing of 500MHz IF bandwidth per sideband. The key component of this set-up is the digital IF-hybrid and its non-stop integration spectrometers that compensate the phase and amplitude imbalances and perform the sideband-separation at the same time. The digital 2SB receiver was implemented in an FPGA-based board developed by the CASPER community.⁸ The ROACH¹² is a platform based in a Xilinx Virtex 5 FPGA (Virtex-5 XC5VSX95T-1FF1136¹³).

The FPGA configuration is specified using a hardware description language (HDL) with the help of Matlab-Simulink as a visual user interface. FPGAs contain an array of programmable logic resources and a layer of re-configurable interconnections that allow these resources to be connected, permitting the implementation of custom hardware. Logic blocks can be configured to perform complex logic functions, or used as look-up tables. In most FPGAs logic blocks also include memory elements, which may be simple flip-flops or complete Random Access Memories (RAMs). In Xilinx nomenclature, they are called “Block RAMs” (BRAMs). In addition to the above, the Virtex-5 FPGA have several thousand arithmetic units (ALUs) available on a single chip most of them are DSP48 slices. The DSP48 is a digital signal processing logic element, with both an exceptional capacity of performing all kinds of arithmetic operations and efficient calculation working in parallel.¹⁴

2.2 Method

The method consists of first in the implementation of a digital hybrid and real-time spectrometer FPGA-based platform and a fast ADCs capable of non-stop integration. Second, it is necessary to measure and characterize the receiver front-end to measure relative amplitude and phase of the receiver I-Q channels. Finally, the calibration data is loaded into the model of IF hybrid implemented inside the FPGA.

2.2.1 Implementation

As shown in Fig. 1 the two front-end outputs are digitalized by the ADCs at 1 GSPS, with 8 bits resolution. The data is then passed to two independent polyphase filter banks (PFB). The PFBs consist of an FIR filter and a 2048 channels Fast Fourier Transform (FFT) block. Fig. 1 The digital hybrid is composed of the complex calibration vectors C_1 , C_2 , C_3 and C_4 and the adder tree. The samples, after the computation of the FFT, are multiplied by the calibration constants, summed and squared (allowing the power to be calculated). After this, a 64-bit accumulator adds the spectra in several BRAMs with a configurable integration time. Finally, the integrated spectrum is retrieved by a desktop computer using a Python script. In order to calibrate the digital sideband-separating spectrometer we computed the complex constant that characterize the analog front-end.

A second spectrometer was designed to measure the amplitude and phase of both I and Q channels. The calibration spectrometer, instead of accumulating the sideband-separated power spectrum, records the complex spectral information.⁹ Fig. 2 shows the block diagram of the calibration spectrometer used to measure the amplitude and phase at both IF outputs. As described in Finger et al.,⁹ the equation (1) presents the amplitude ratio of the two channels that is computed as the quotient of the amplitudes V_1 and V_2 for each spectral channel.

$$X = \frac{V_1}{V_2} \quad (1)$$

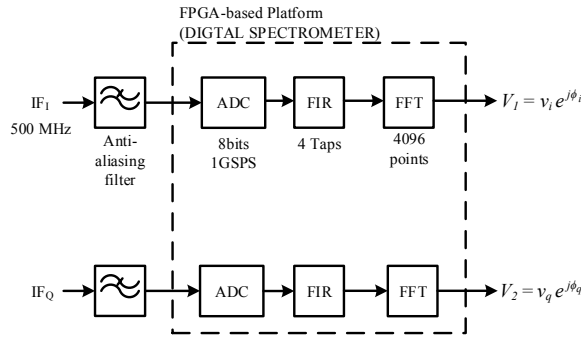


Figure 2: Digital Sideband Separating Spectrometer calibration schematic. Two identical branches were implemented in order to compute the calibration constants to compensate the system imbalances of the analog front-end. The 2 FIR filters and 2 FFTs were implemented in the FPGA.

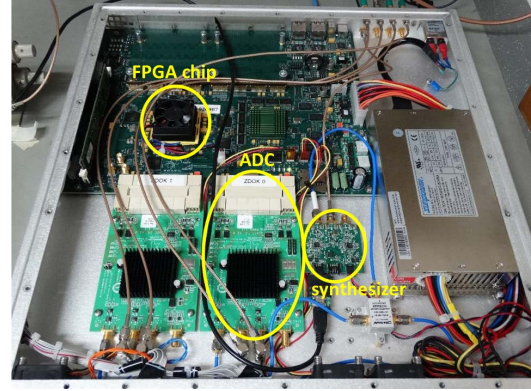


Figure 3: ROACH-II. Two ADCs 5 GSps are connected to ZDOK connectors. The synthesizer module (valon 5007¹⁵) provides the clock reference to the ADC boards.¹⁶

The angles ϕ_{USB} and ϕ_{LSB} are defined for each FFT channel according to the equations (2) and (3):

$$\phi_{LSB} = (\phi_i - \phi_q) \quad (2)$$

$$\phi_{USB} = (\phi_i - \phi_q) \quad (3)$$

C1 and C4 are set to 1+0j while C2 and C3 are determined using the equations (4) and (5):

$$\frac{1}{C_2} = \frac{1}{X} e^{-j(\phi_{LSB} - \pi)} \quad (4)$$

$$C_3 = \frac{1}{X} e^{-j(\phi_{USB} - \pi)} \quad (5)$$

2.2.2 Synthesis

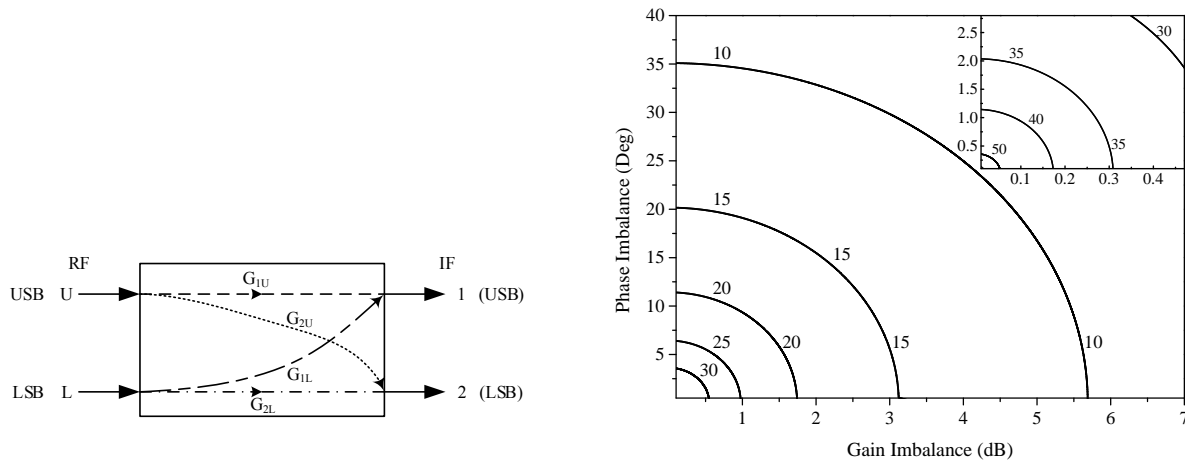
According to the Fig. 4a to determine the theoretical image rejection of sideband-separating receiver, we can consider the generalized input-output behavior of a 2SB receiver showing the signal flow from the RF input to the IF outputs (Kerr et al.¹⁷). Such receiver is depicted in the Fig. 4a. G_{1U}, G_{2U}, G_{1L} and G_{2L} are the power gains between both inputs and outputs. The only assumption is that the RF upper and lower sideband ports input to the system separately, the IF outputs are used to define the SRR.

The sideband rejection is defined R_1 and R_2 in the output ports IF₁ and IF₂, in the Fig. 4a, from equations (6) and (7):

$$R_1 = \frac{G_{1U}}{G_{1L}} \quad (6)$$

$$R_2 = \frac{G_{2L}}{G_{2U}} \quad (7)$$

For a good understanding of the Sideband Rejection Ratio concept a simple theoretical model is given by Jacob Kooi et al.¹⁸ Where G and ϕ are the total amplitude and phase imbalances, respectively. Fig. 4b illustrates how the rejection ratio is affected by the imbalances.



(a) Generalized input-output behavior of the sideband-separating receiver proposed in the ALMA Memo 357.¹⁷

(b) Sideband rejection ratio for different phase and gain imbalances as calculated from equation (8). The inset shows the rejection ratio for imbalances below 0.5 dB and 3 degrees.¹

Figure 4: Theoretical Image Rejection of a Sideband-Separating Receiver.

$$RR = -10 \times \log \left(\frac{1 - 2\sqrt{G} \cos \phi}{1 + 2\sqrt{G} \cos \phi} \right) \quad (8)$$

Fig. 4b shows that with small values of the variables G and ϕ it is possible to obtain high Sideband rejection ratios. Typical wideband analog 2SB receivers achieve sideband rejections between 10 to 20 dB, indicating that the imbalances in phase and gain are around 12-35 degrees and 1.7 to 5.7 dB, respectively. To overcome this problem we introduce digital processing to measure and compensate the imbalances presented in the analog front-end obtaining higher sideband rejection ratios.

2.3 Laboratory Proof of concept results

Fig. 5 shows the results of the 4 GHz experiment. A sideband rejection in the order of 50 dB is achieved, this is a factor of 100 to 1000 higher than current analog technology.⁹

2.4 Laboratory experiments at 3mm wavelength

The receiver used for this implementation was a prototype for the SMWT currently located at Cerro Calán, Santiago, Chile. This prototype was tested in the laboratory with an RF of 80-100 GHz. Fig. 7 shows the block diagram of the experiment. As shown in Fig. 9 the signal is injected to the receiver using horns, to include the optics of the receiver in the calibration process. The signal passes through an amplifier, and an isolator before it reaches the RF hybrid where the signal power is split in half and shifted in 90 degrees. After the RF hybrid, the signal passes to the mixers where it is downconverted to baseband with a bandwidth of 3 GHz. The digital spectrometer works at 0.5 GHz then a filter is required after the mixer in order to avoid aliasing effects. The chain of amplifiers is necessary in order to achieve the 0 dBm required at in the input of the ADCs.

Figure 8, shows the SRR for the 3mm receiver in five different LO frequencies, with an IF bandwidth of 500 MHz in each sideband. On this prototype, the SRR is higher than 45 dB for most of the band, while drops to about 40 dB at the end of the band. The main effect causing the reduction in SRR is the decrease in conversion gain due to a lack of LO power.

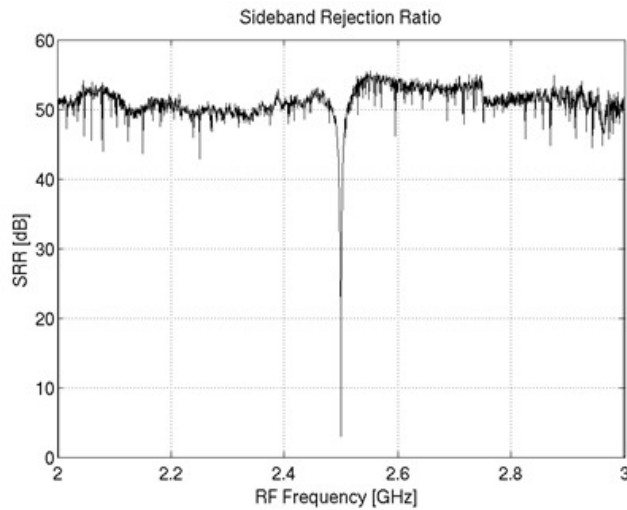


Figure 5: Measured Sideband Rejection Ratio after calibration. The plot shows the SRR for a 2 to 3 GHz RF. The drop at 2.5GHz (IF=0) is due to the DC decoupling of the ADCs.⁵

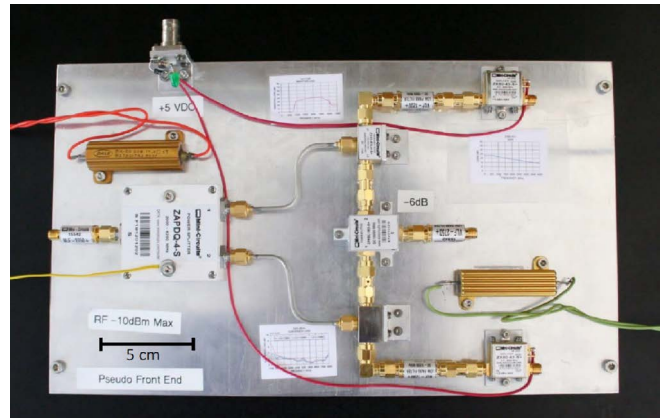


Figure 6: 4 GHz Analog Front-End used as a mock-up receiver.⁹

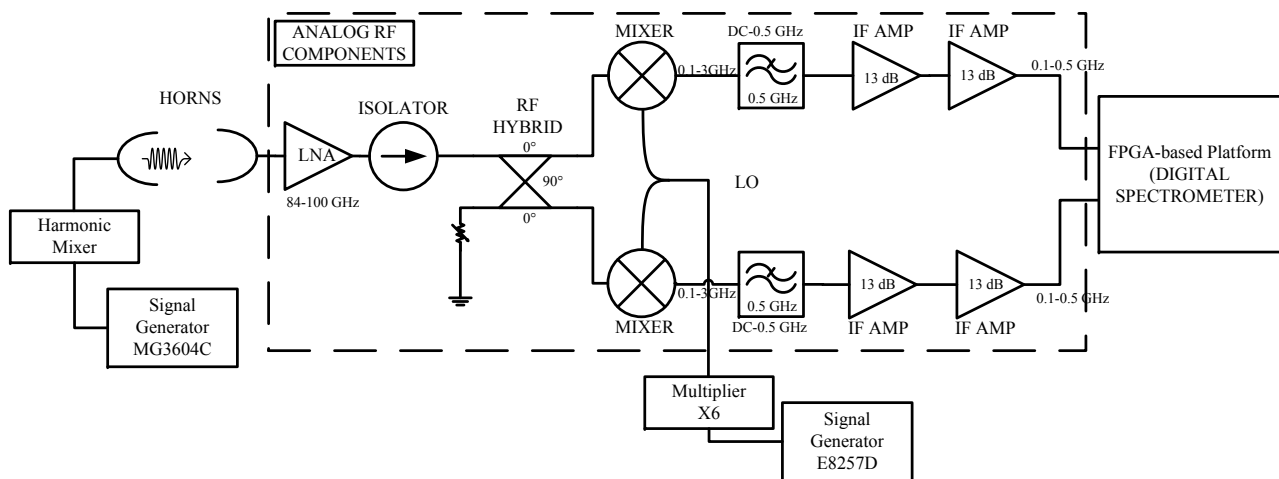


Figure 7: Scheme of the 3mm receiver laboratory experiment. The IF amplifiers are used in order to get the 0dBm at the input of the ADC, this is the point where the ADC has the best performance.¹⁹

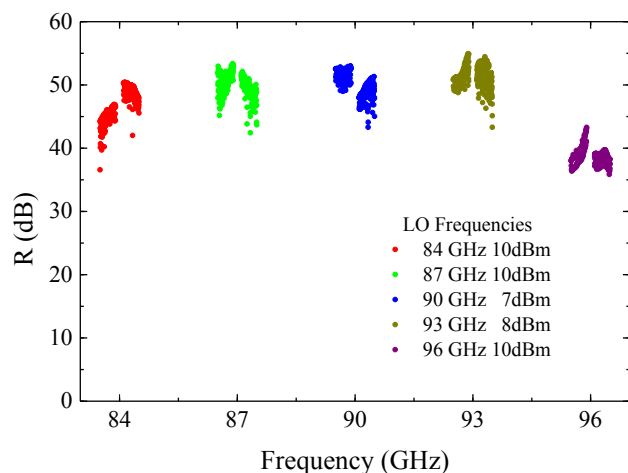


Figure 8: Digital Sideband Rejection using a 3mm receiver.¹

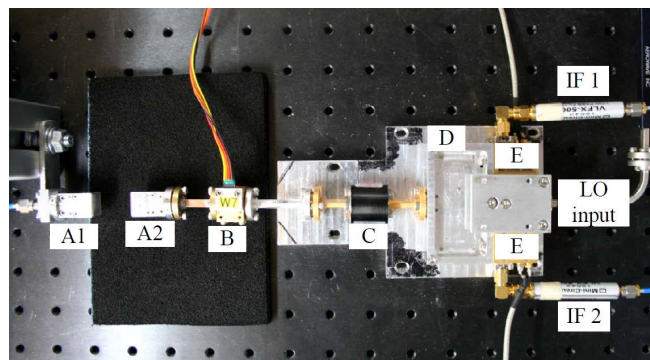


Figure 9: 115 GHz astronomical-grade Front-End. The components are A1/2: Horns, B:HEMT Amplifier, C: Isolator, D: RF hybrid, E: Mixers.⁹

2.5 On telescope calibration test

This section reports the integration of a digital sideband separating spectrometer with the 1.2m Southern Millimeter Wave Telescope (SMWT Fig. 12) in order to demonstrate the technique and to test the calibration capabilities on a radio telescope, including the antenna and optical components. In the next subsections, we present briefly the SMWT configuration and results.

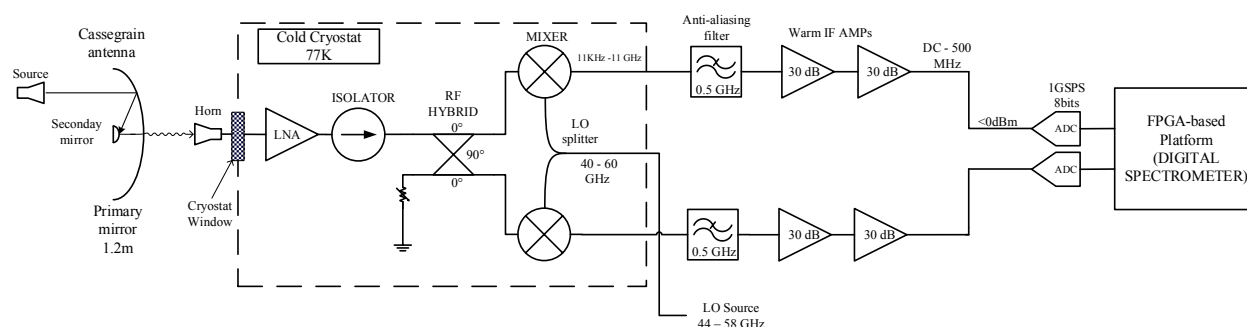


Figure 10: 1.2m Southern Millimeter Wave Telescope (SMWT) block diagram.

2.5.1 Calibration in mm-waves

Fig. 10 shows the block diagram of the SMWT, the RF band for this test was 114.521 to 115.521 GHz. The calibration was performed by quasi-optical injection of the test tone using a probe antenna pointing to the primary mirror of the Cassegrain antenna. The test tone is then reflected towards the secondary mirror to be coupled to the receiver horn antenna, i.e. following the same path of the astronomical signal. The test tone swept the USB and LSB computing the calibration constants as explained in the previous sections.

2.5.2 Results

Results of this experiment are presented in the Fig. 11. The calibrated receiver in the telescope exhibit an Image rejection above 32dB in the whole band, with an average close to 40dB. The degradation with respect to the laboratory setup at the same wavelength is explained by the relatively large ripple in the telescope receiver pass band. Since the SRR measurement is done with a fixed test tone power, minimal in conversion gain translates into minimal in dynamic range, which limits the ability to measure very high SRR.

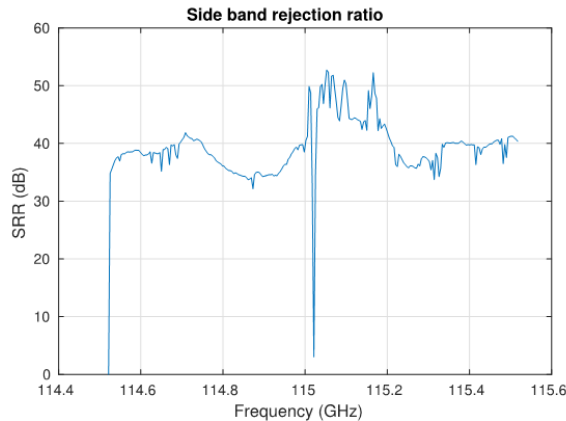


Figure 11: Measured Sideband Rejection Ratio performance after calibration of all spectral channels. The plot shows the SRR in the millimeter band from 114.521 to 115.521 GHz and the LO = 115.021 GHz.



Figure 12: 1.2 meter Souther Millimeter Wave Telescope (SMWT) ¹⁰

2.6 Laboratory ALMA Band-9

This section reports the integration of a digital sideband separating spectrometer with an ALMA Band-9 2SB prototype receiver in order to demonstrate, calibrated digital sideband separation at sub-millimeter wavelengths. In the next subsections, we present the analog ALMA Band 9 test setup, followed by the digital back-end configuration, and the experiment results.

2.6.1 Test-setup and measurement description

Figure 13 shows the ALMA band 9 receiver block diagram. A first down-conversion to a 4–12 GHz IF band driven by an in-phase local oscillator (LO1) was performed using a pair of superconducting (SIS) mixers. Then a second down-conversion to a 0–1 GHz baseband is driven by an in-phase second local oscillator (LO2). LO1 was swept from 614 to 710 GHz with 8 GHz sub-bands, while LO2 was swept with steps of 1GHz from 4 to 12 GHz for each LO1 setting, to provide the full analysis of the ALMA Band 9 bandwidth. Cold and warm LNAs are used in order to amplify the signal and then equalizers compensate the amplifiers gain slope. Anti-aliasing filters and the last amplification stage are applied to reach optimal signal condition for the ADCs in the digital Back-end. The test source and the local oscillators were locked to 10 MHz references to prevent frequency drift of the test tone during calibration. Finally, the digital hybrid and the spectrometers implemented in the digital Back-end perform the recombination of the I and Q channels obtaining the USB and LSB separated.

2.6.2 FPGA gateware optimization - Floorplanning

The method shown in the previous section works reasonably well sweeping small RF bands with IF bandwidth of 500 MHz. However, for this experiment, a very wide sweep along the ALMA band 9 (614 to 710 GHz divided into 12 sub-bands from 4 to 12 GHz) was required. So we decided to expand the baseband bandwidth to 1GHz to optimize the ALMA band 9 measurement. To achieve 1 GHz of baseband bandwidth we had to manually constrain the placement of resources on the FPGA. It helps to lower the delay time between logic resources,²⁰ allowing faster FPGA clock rates. This is an optimization technique of FPGA hardware and this process is called floorplanning. The software used to perform the floorplanning was Xilinx ISE, PlanAhead. In order to obtain optimal results, i.e. speed up the FPGA clock rate, we placed BRAMs and DSP48s of the design into specific areas or “Pblocks”. Once the Floorplanning was done, several constraints were created with the aim of improve the efficiency of the Placement-And-Routing (PAR) algorithm. The PAR algorithm is efficient enough placing auxiliary logic, obtaining optimal results during the compilation process. On the other hand, applying hand placement usually falls into suboptimal results.²⁰ Figure 14 shows the logic resources placement in the FPGA chip area, before and after floorplanning. The colors represent the different subsystems depicted in Figure 1. The FIR was located on the left side of the chip near of the I/O banks, then the 4096 point FFT was divided

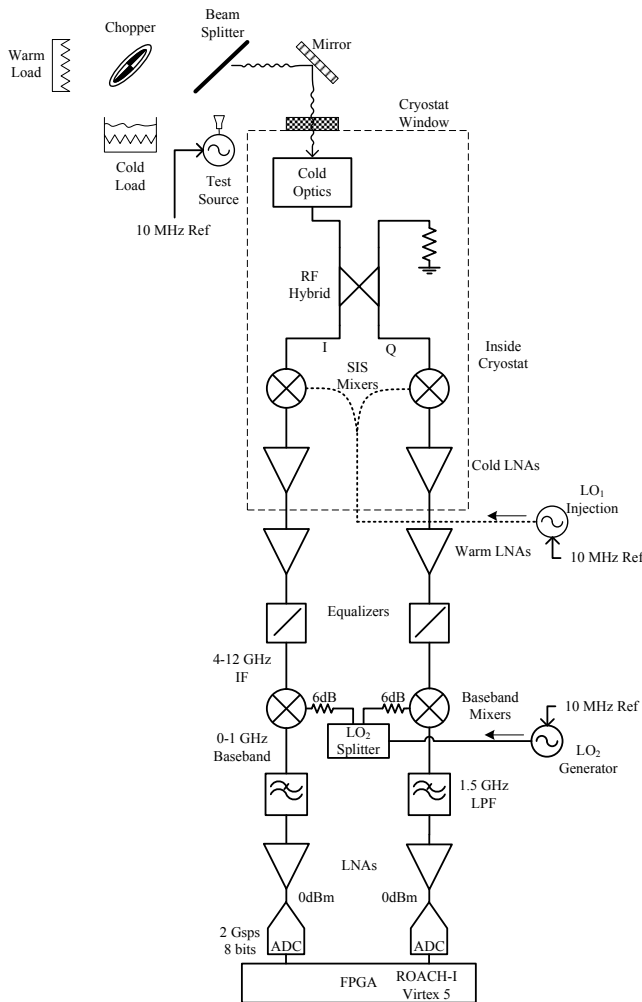


Figure 13: Test setup block diagram.²

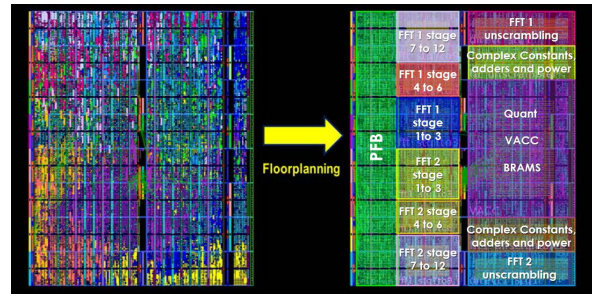


Figure 14: Logic resources allocation in the FPGA (Virtex 5) chip surface before and after floorplanning. Each color represents a processing subsystem depicted in Figure 1.²⁰

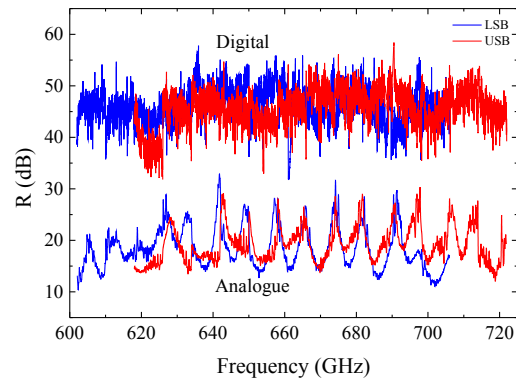


Figure 15: Calibrated digital sideband rejection ratio vs. Analogue sideband rejection performance (Khudchenko et al. 2011) is shown for comparison.²

into 4 stages for a better placement. Complex constants, the power stage, and the vector accumulator were placed beside the Output I/O banks, following the scheme in Figure 1. After applying Floorplanning in the current design we reduced data path delay within subsystems in the chip from 8ns to 4ns. The optimized design doubles the clock frequency achievable by the automatic compilation tools, reaching an instantaneous bandwidth of 1GHz per sideband.²⁰

2.6.3 First results at sub-millimeter wavelengths

The measurement with second down-conversion was performed applying the new methods and techniques mentioned before and it is presented in Figure 15. The SRR for the entire ALMA Band-9 RF band using the technique presented above. This digital 2SB receiver shows an average sideband rejection of 45.9 dB while small portions of the band drop below 40 dB. The performance is 27 dB (a factor of 500) better than the average performance of the proof-of-concept Band 9 purely-analog 2SB prototype receiver developed by SRON.²

3. POLARIZATION DETECTION

An Ortho-Mode Transducer (OMT) is a device that separates an incoming signal into two orthogonal polarizations. Typical analog OMTs are often bulky and geometrically awkward, which make it difficult to integrate them with the rest of the elements of the radio telescope receiver.³ On the other hand, asymmetries in the OMT

waveguide and non-linear behavior of analog components produce errors in the polarization measurement, which are manifested as reflections and cross-polarization leakage. Recent advances in digital systems are seen as a promising option for correcting the system imperfections, by adding complex constants that compensate gain and phase imbalances, effectively increasing the OMT accuracy.

3.1 Hardware Description

In this work, we present a novel class of OMT which use digital calibration to synthesize the desired polarization vectors to achieve very low cross-polarization. Inspired by the work of Morgan et al.³ we decided to focus our efforts on implementing the proof of concept developed by NRAO using off-line processing of narrow bandwidths, but using on a real-time Virtex-6 FPGA (XC6VSX475T-1FFG1759C)²¹ processing platform, wide instantaneous bandwidth, and non-stop integration capabilities. To implement the DOMT we are using a ROACH-2²² (Fig. 3) platform equipped with two 5 Gs/s (max) analog-to-digital converter (ADC). Each ADC uses an e2v EV8AQ160 chip²³ with 4 cores at 8-bit resolution. Each ADC board allows to sample up to two signals in parallel, the ROACH-2 platform can be configured for 4 inputs. The analog part of the DOMT consists of a circular waveguide to four probes coaxial transition. Each output is connected to an independent receiver chain constituting its Front-End. Figure 16 shows a block diagram of the OMT with 4 outputs.

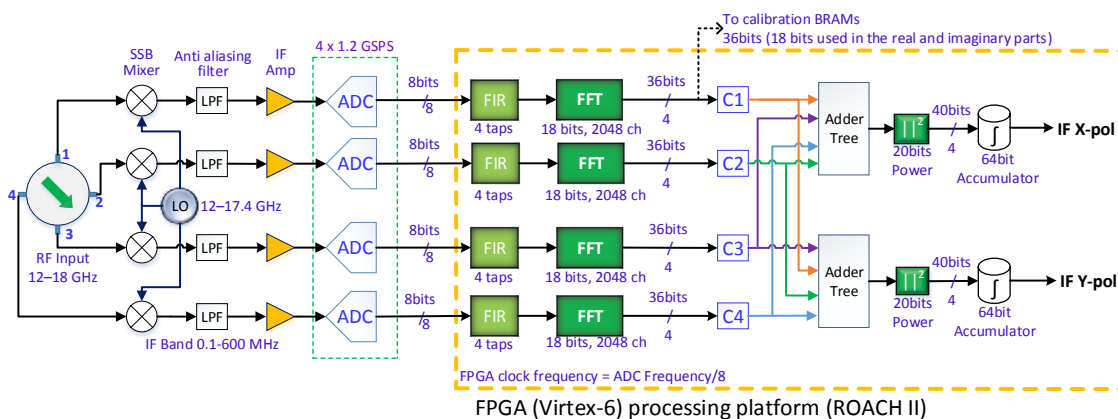


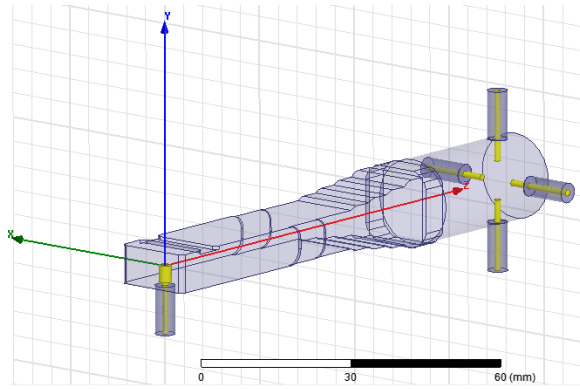
Figure 16: Digital OMT block diagram. The inside of the yellow block represents the polarization synthesis model of the FPGA. To the left of the yellow block is the OMT analog front-end.

The analog OMT has been designed using HFSS software for the Ku-band, so the Front-End bandwidth is between 12-18 GHz. We have chosen this band to easily obtain commercial devices for the front end and center our efforts in the development of the FPGA gate-ware for the digital signal processing.

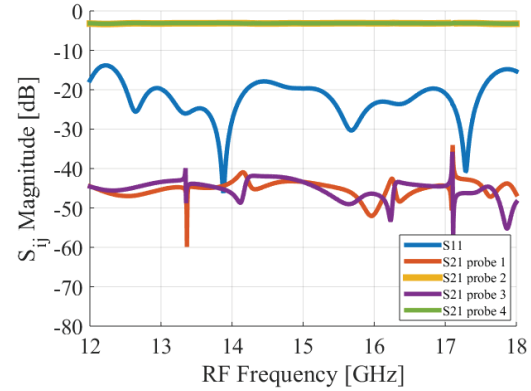
3.2 Design

The analog OMT design specifications are the following: Operation in Ku-band, Simple SMA Coaxial probes, Easy to build and miniaturized, Reflections ($S_{11} \leq -20dB$, Cross-polarization $< -30dB$). The proposed design is a circular waveguide to 4 coaxial SMA probes OMT. As shown in Figure 17a, this design is very symmetrical and is easy to be built mechanically. The circular waveguide is a standard Ku-band circular waveguide with a diameter of 12.7mm. The probes are Pasternak PE4128 SMA connectors. The position and length of the central pins are optimized to meet the specifications. Figures 17a and 17b show the electromagnetic design and simulation for the Digital OMT front-end. The OMT was simulated with 1 MHz discrete frequency sweep. There is a good performance in almost all the band while only two narrow resonant peaks are present.

Prototypes were manufactured using a CNC Milling Machine. The prototypes after construction are shown in Fig. 18.



(a) HFSS 3D model. OMT + Circular to rectangular waveguide transition + WR-62 to SMA transition.



(b) Transmission, reflection and cross-polarization of the OMT + Circular to rectangular waveguide transition + WR-62 to SMA transition.

Figure 17: OMT front-end design and simulation.



(a) Top view of manufactured OMT.



(b) Top view of of the circular-rectangular transition.

Figure 18: Manufactured OMT

3.3 Method

Mathematically the input-output performance of the DOMT of four probes can be described by the following linear equation:

$$\begin{bmatrix} v_1 \\ v_2 \\ v_3 \\ v_4 \end{bmatrix} = \begin{bmatrix} a_{1x}e^{j\theta_{1x}} & a_{1y}e^{j\theta_{1y}} \\ a_{2x}e^{j\theta_{2x}} & a_{2y}e^{j\theta_{2y}} \\ a_{3x}e^{j\theta_{3x}} & a_{3y}e^{j\theta_{3y}} \\ a_{4x}e^{j\theta_{4x}} & a_{4y}e^{j\theta_{4y}} \end{bmatrix} \begin{bmatrix} s_0 \cos(\alpha)e^{j\beta} \\ s_0 \sin(\alpha)e^{j\beta} \end{bmatrix}, \quad (9)$$

or in matrix form:

$$V = GS. \quad (10)$$

S represents a sinusoidal input signal, where s_0 is the signal amplitude, α its incidence angle, and β its phase. $V = [v_1, v_2, v_3, v_4]$ is the output voltage vector, measured in the probes. G is the complex gain matrix that characterize the OMT, individual amplitudes a_1, \dots, a_4 and phases $\theta_1, \dots, \theta_4$ provide the full characterization.

From an astronomer perspective, one wants to compute the orthogonal signals in S , given the OMT output V , hence, equation (10) must be inverted. An efficient way to do it is to use the Moore-Penrose Pseudo-Inverse, given by^{*}:

$$H = (G^*G)^{-1}G^*, \quad (11)$$

then S can be computed as:

$$S = HV. \quad (12)$$

Matrix H represents the compensation transformation that corrects the errors from the analog front-end. In general, the OMT response is frequency dependent, so every frequency channel must be characterized independently. This is displayed in the DOMT and is called the “Calibration Phase”. The calibration consists of the performance of two tests where a pure tone is fed to the front-end in 0° and 90° polarization respectively. For each test, a frequency sweep is done at each spectral channel in the desired RF band. For each frequency channel, the complex frequency vector V is computed via Fast Fourier Transform (FFT) algorithm, and stored in memory. Then, the elements of G can be computed in an offline manner, where the exact mathematical equations can be presented.³ Finally, G is used to compute the correction matrix H by (11). Actual polarization measurements are made by applying the corrections to voltage vector as in (12).

3.4 Implementation

A ROACH2 board[†] from CASPER community is used for the digital back-end of the DOMT, which main core is the Virtex-6 SX475T FPGA chip. The FPGA gateway is separated into two subsystems: the “calibration” and “polarization synthesis”. This is done to simplify the implementation.

The calibration model is presented in Figure 19. The four front-end outputs are digitalized by the ADC at a 600MSPS, with an 8 bit resolution, which is then passed to four independent polyphase filter banks (PFB). The PFB consist in a 4 tapped FIR filter and an FFT block of 2048 channels. The complex values of the FFT are then split in real and imaginary part, which are stored in the dynamic Block RAMs (BRAM) of the FPGA for offline processing.

In the calibration phase, the spectrum of a pure tone must be recorded for each spectral channel of the FFT, for both 0° and 90° polarization. Each pair of spectra is used to compute a (specific channel) gain matrix G in a computer using the spectral information recorded by the FPGA.

To ensure the synchronization between the input signal and the FFT, a synchronization block is implemented so the FPGA’s delay does not affect the recording of the computation until the input signal has changed frequency.

3.4.1 Results

An ideal (uncalibrated) digital OMT was implemented, loading the ideal H matrix (eq. 13) into the DOMT (ROACH2). Figure 20 shows the uncalibrated X-pol and Y-pol spectra for a 12.15GHz test tone, the LO signal was set to 12GHz. Spurious signals are generated in the ADC and can be seen at -45dBc limiting the spurious free dynamic range to about 45dB. The polarization isolation in this example exceeds 40dB.

$$[H_4] = \begin{bmatrix} \frac{1}{2} & 0 & \frac{-1}{2} & 0 \\ 0 & \frac{1}{2} & 0 & \frac{-1}{2} \end{bmatrix} \quad (13)$$

The next steps in this project consist in calibrating the OMT in order to get higher polarization isolation. Calibrated Polarization synthesis results are expected for late 2016.

^{*}unary operator * indicates complex conjugate.

[†]<https://casper.berkeley.edu/wiki/ROACH2>

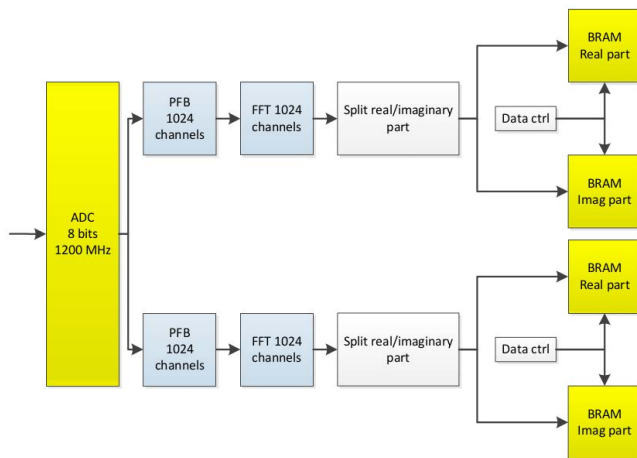


Figure 19: Digital OMT calibration schematic.

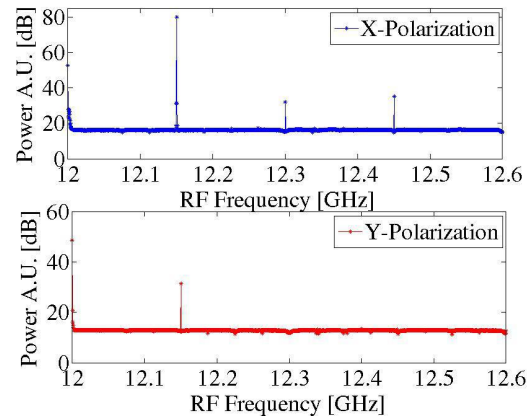


Figure 20: Polarization isolation of an uncalibrated digital OMT (ideal constants) between co-polarization and cross-polarization spectra. LO was set to 12GHz and the RF was 12-12.6[GHz]. Spurious signals appear along side the band.

4. CONCLUSION

It has been demonstrated that radio astronomy receivers' performance can be considerably improved by expanding the role of digital electronics in current designs. The first technique showed in this work, the calibrated digital sideband separation, has the potential of implementing 2SB receivers at frequencies where no such instruments exist, as well as improving the image rejection of current millimeter and sub-millimeter 2SB receivers to a level where sideband contamination is so low that would become negligible for any known astronomical application. The second technique, calibrated digital polarization synthesis, has the potential to reduce receivers' cross-polarization leakage to allow optimal observation of weakly polarized astronomical sources.

We have shown that the calibration needed for optimal digital sideband rejection can be done with the receiver installed in a telescope, including all optical elements in the signal path.

ACKNOWLEDGMENTS

This work was possible thanks to the support of the Center of Excellence in Astrophysics and Associated Technologies (CATA-BASAL-PBF 06), FONDECYT 11140428 and ALMA-Conicyt 31150012. We thank José Pizarro for the mechanical design and manufacturing of waveguide components. We also thank Xilinx INC. for the donation of FPGA chips and software licenses, as well as the support of the entire CASPER collaboration.

REFERENCES

- [1] Rodríguez, R., Finger, R., Mena, F., Reyes, N., Michael, E., and Bronfman, L., "A sideband-separating receiver with a calibrated digital if-hybrid spectrometer for the millimeter band," *Publications of the Astronomical Society of the Pacific* **126**(938), 380 (2014).
- [2] Finger, R., Mena, F., Baryshev, A., Khudchenko, A., Rodriguez, R., Huaracan, E., Alvear, A., Barkhof, J., Hesper, R., and Bronfman, L., "Ultra-pure digital sideband separation at sub-millimeter wavelengths," *Astronomy & Astrophysics* **584**, A3 (2015).
- [3] Morgan, M. A., Fisher, J. R., and Boyd, T. A., "Compact orthomode transducers using digital polarization synthesis," *Microwave Theory and Techniques, IEEE Transactions on* **58**(12), 3666–3676 (2010).
- [4] Fisher, J. and Morgan, M., "Analysis of a single-conversion, analog/digital sideband-separating mixer prototype national radio astronomy observatory electronics division internal report no. 320," (2008).
- [5] Finger, R., *Design and Construction of a Digital Sideband Separating Spectrometer for the 1.2-meter Southern Radio Telescope*, ph.d. thesis, Universidad de Chile, Facultad de Ciencias Físicas y Matemáticas, Santiago, Chile (March 2013).

- [6] Murk, A., Treuttel, J., Rea, S., and Matheson, D., “Characterization of a 340ghz sub-harmonic iq mixer with digital sideband separating backend,” in *Proceedings of the 5th ESA Workshop on Millimetre Wave Technology and Applications*, 469–476 (2009).
- [7] Morgan, M. A. and Fisher, J. R., “Experiments with calibrated digital sideband-separating downconversion,” *Publications of the Astronomical Society of the Pacific* **122**(889), 326 (2010).
- [8] “Casper.” <https://casper.berkeley.edu/>. Accessed: 2015-09-30.
- [9] Finger, R., Mena, P., Reyes, N., Rodriguez, R., and Bronfman, L., “A calibrated digital sideband separating spectrometer for radio astronomy applications,” *Publications of the Astronomical Society of the Pacific* **125**(925), 263 (2013).
- [10] “Millimeter-wave laboratory.” http://www.das.uchile.cl/lab_mwl/. Accessed: 2016-05-20.
- [11] “Adc083000.” <http://www.ti.com.cn/cn/lit/ds/symlink/adc083000.pdf>. Accessed: 2016-05-26.
- [12] “Roach.” <https://casper.berkeley.edu/wiki/ROACH>. Accessed: 2016-05-30.
- [13] “Virtex-5 family overview (datasheet).” http://www.xilinx.com/support/documentation/data_sheets/ds100.pdf. Accessed: 2016-05-30.
- [14] “Dsp48 slice.” <http://www.xilinx.com/technology/dsp/xtremedsp.htm>. Accessed: 2016-05-30.
- [15] “5007 dual 137.5-4400mhz frequency synthesizer module.” http://valontechnology.com/5007/5007_r4_ds.pdf. Accessed: 2016-05-30.
- [16] Sapunar, R., *Diseño e implementación de un espectrómetro de alta resolución basado en FPGA para el análisis de señales radioastronómicas*, engineering thesis, Universidad de Chile, Santiago, Chile (March 2015).
- [17] Kerr, A., Pan, S., and Effland, J., “Alma memo 357,” *Sideband Calibration of Millimeter-Wave Receivers* (2001).
- [18] Kooi, J. W., [*Advanced receivers for submillimeter and far infrared astronomy*], Rijkuniversiteit Groningen (2008).
- [19] Rodríguez, R., *Design, Construction and Testing of a 2SB Receiver for the Southern Millimeter-Wave Telescope*, ph.d. thesis, Universidad de Chile, Facultad de Ciencias Físicas y Matemáticas, Santiago, Chile (March 2015).
- [20] Alvear, A., *Extensión del Ancho de Banda de Espectrometros Radioastronómicos Basados en FPGA*, engineering thesis, PUCV, EIE, Valparaíso, Chile (March 2014).
- [21] “Virtex-6 family overview (datasheet).” http://www.xilinx.com/support/documentation/data_sheets/ds150.pdf. Accessed: 2016-05-30.
- [22] “Roach2.” https://casper.berkeley.edu/wiki/ROACH-2_Revision_2. Accessed: 2015-09-30.
- [23] “Ev8aq160 quad adc.” <https://casper.berkeley.edu/wiki/images/1/19/Ev8aq160.pdf>. Accessed: 2016-05-16.

Appendix B

Simulink Top Level block diagram of the DOMT

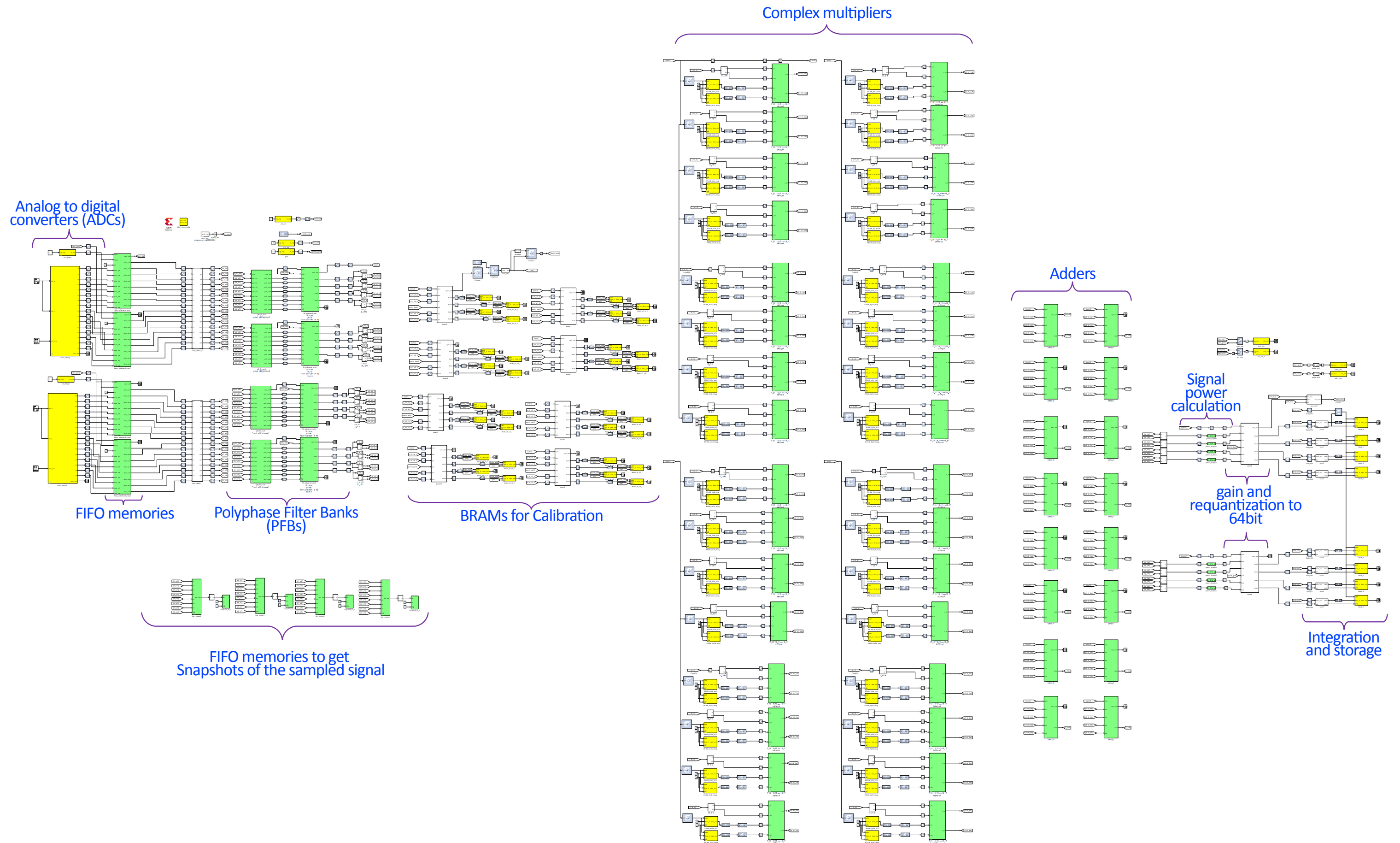


Figure B.1. Top level block diagram of the DOMT.

Appendix C

OMT degraded

The analog OMT itself presents an unbeatable cross-polarization performance via calibration, around -40dB on average along the Ku-band. Hence, we decided to include in this thesis the study of an analog OMT with a cross-polarization degraded in order to achieve a performance of around -30 dB along the Ku-band.

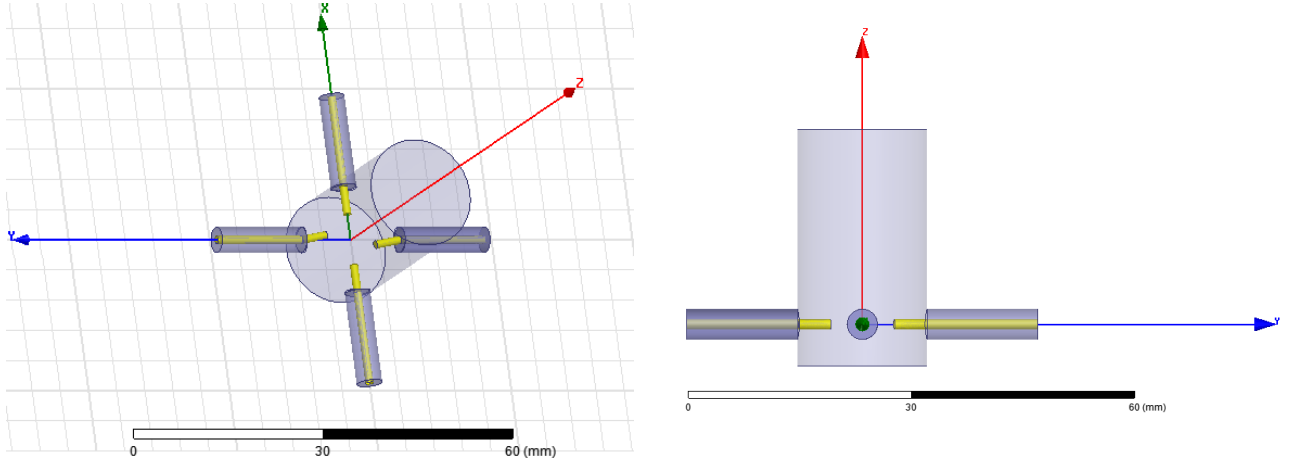


Figure C.1. HFSS 3D model of the degraded circular waveguide to 4 coaxial probes OMT (left) and lateral view of the Circular waveguide to 4 coaxial probes OMT (right).

Two snapshots of the analog orthomode transducer degraded prototype are shown in Figure C.1. As shown in the left Figure C.1, this design is very symmetrical, though the two probe antennas placed in the y-axis were bent 10° clockwise. This is easily machined and procured to introduce cross-polarization without degrading the reflection and transmission performance.

The model was simulated in HFSS using a discrete sweep of 100 MHz, the results of the transitions and reflections for both polarizations are shown in Figure C.2. The OMT has reflections below -20dB from 12.8 GHz to 17.8 GHz and fit completely the simulation result presented in Figure 3.3.

The simulation of the degraded OMT has a cross-pol of -36dB on average (Figure C.3). Two resonant peaks are present at 14.1 GHz and from 17.8 to 18 GHz. These peaks are 200 MHz

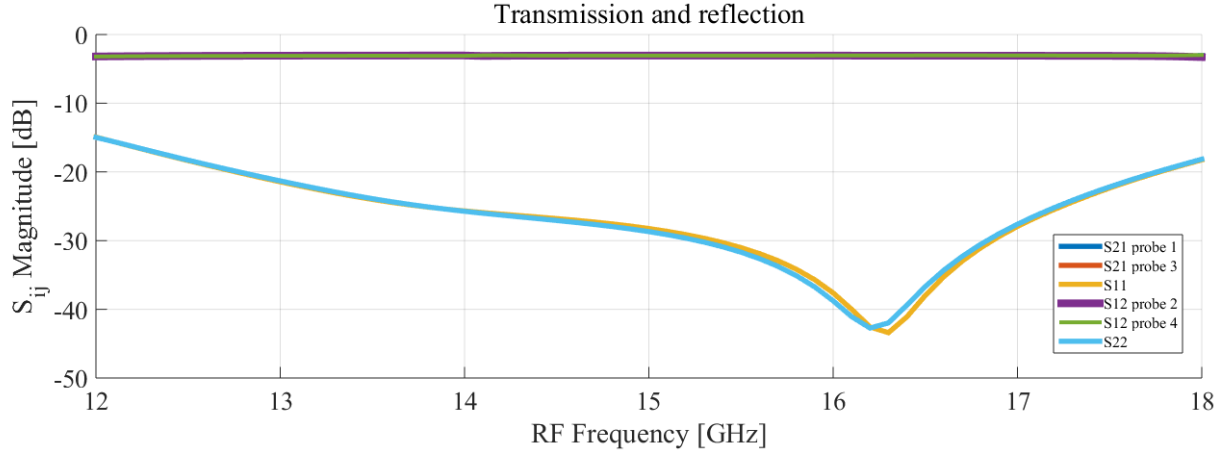


Figure C.2. Circular waveguide to 4 coaxial probes degraded OMT transmission and reflection simulation results using HFSS.

wide, however have low amplitude, so they should not generate major problems in the final performance.

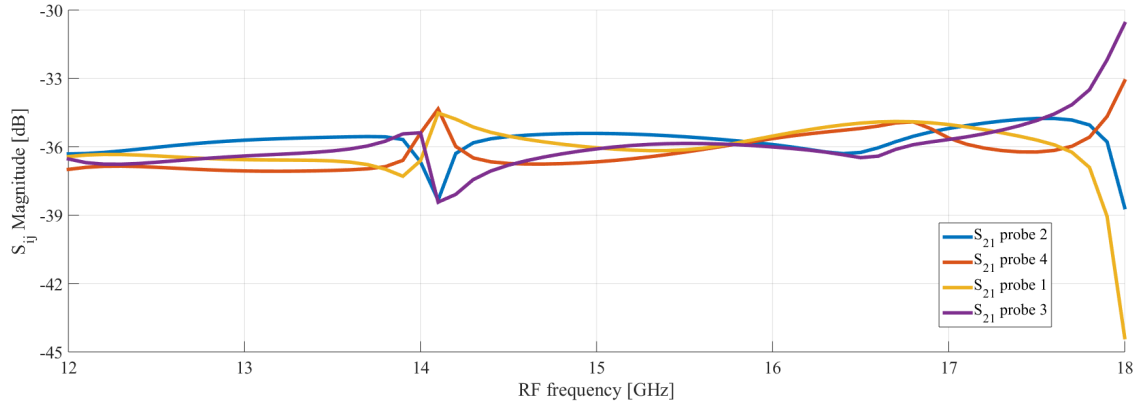


Figure C.3. Circular waveguide to 4 coaxial probes degraded OMT and cross-polarization simulation results using HFSS.

Two new probes were manufactured and installed in the OMT as shown in Figure C.4.

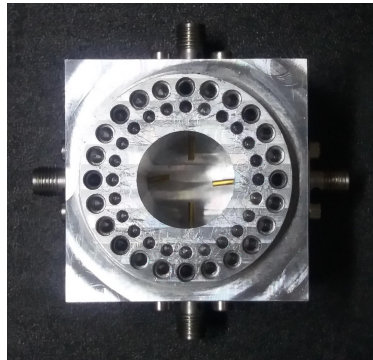


Figure C.4. Photograph of the prototype digital orthomode transducer. Four probes OMT manufactured in two aluminum blocks with two probes with two bent antennas.

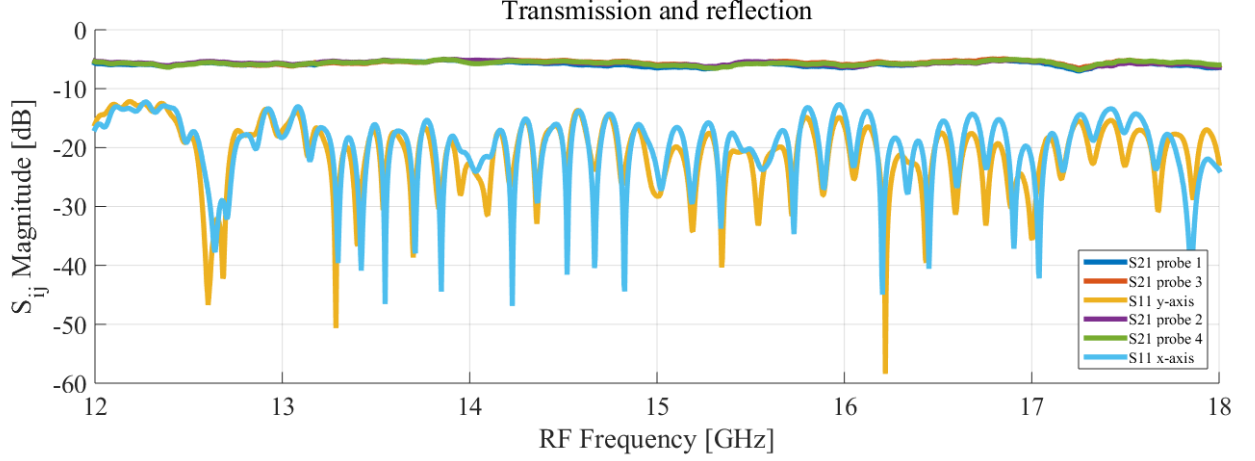


Figure C.5. Circular waveguide to 4 coaxial probes degraded OMT transmission and reflection measurement using VNA.

In Figure C.5 the reflection measurement is presented and its average is below -20dB along the Ku-band. The OMT presents some sections in the band above -20dB, one from 12 GHz at -10.18dB and 12.5 GHz at -20 dB, followed by a resonant peak in 12.55 GHz which is not very wide. The second section above -20dB is from 12.64 GHz to 13.17 GHz followed by a resonant peak in 13.9 GHz in x-pol and 13.84 GHz for y-pol. The reflection average fits the simulation results, however, a ripple along the band is present due to standing waves that contribute only to gain ripple, not cross-polar leakage, therefore this behaviour is acceptable because the system met the project requirements.

On the other hand, the average of the transmission results decreased of the transitions for both polarizations along the Ku-band are in a range about -4 to -5 dB while the simulation result for transmission is at -3dB. The loss in the range of -1dB is due to the cables and adapters that were not calibrated during the VNA set up.

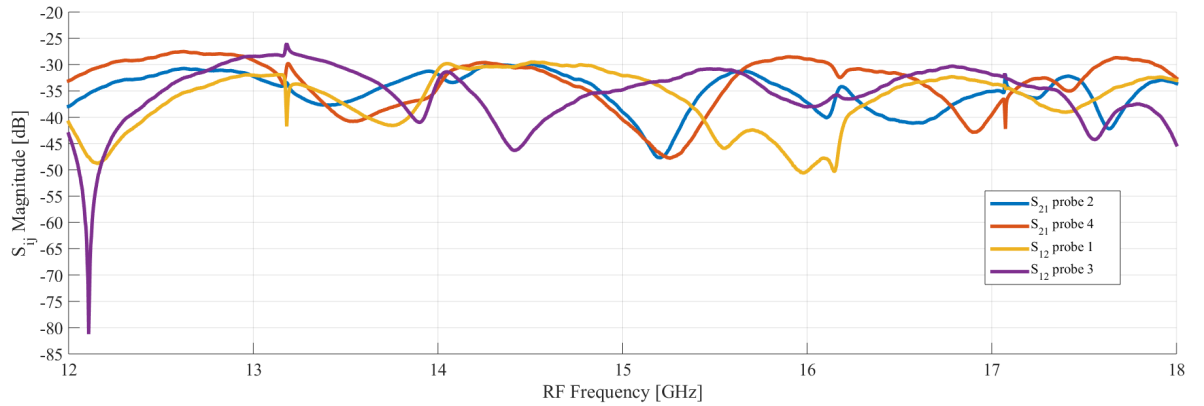


Figure C.6. Circular waveguide to 4 coaxial probes degraded OMT and cross-polarization measurement using VNA.

The measurement results of the degraded OMT has a cross-pol of -35 dB on average (Figure C.6). Several resonant peaks are present in the band, the strongest appear at 12.1 GHz. With exception of 12.1 GHz resonant peak the others are not very wide, however have low amplitude, so they should not generate major problems in the final performance.